1-1-2011

Mechanics of Heart Tube Formation in the Early Chick Embryo

Victor Varner
Washington University in St. Louis

WASHINGTON UNIVERSITY IN ST. LOUIS

School of Engineering and Applied Science

Department of Biomedical Engineering

Thesis Examination Committee:
Larry A. Taber, Chair
Philip V. Bayly
Elliot L. Elson
Guy M. Genin
Patrick Y. Jay
Ruth J. Okamoto
Jin-Yu Shao

MECHANICS OF HEART TUBE FORMATION IN THE EARLY CHICK EMBRYO

by

Victor D. Varner

A dissertation presented to the Graduate School of Arts and Sciences
of Washington University in partial fulfillment of the
requirements for the degree of

DOCTOR OF PHILOSOPHY

December 2011
Saint Louis, Missouri

ABSTRACT OF THE DISSERTATION

Mechanics of Heart Tube Formation in the Early Chick Embryo

by

Victor D. Varner

Doctor of Philosophy in Biomedical Engineering

Washington University in St. Louis, 2011

Research Advisor: Professor Larry A. Taber

The heart is the first functioning organ to form in the embryo. For decades, biologists have worked to identify many of the genetic and molecular factors involved in heart development, and over the years, these efforts have helped elucidate the vast biochemical signaling networks, which drive cardiac specification and differentiation in the embryo. Still, the biophysical mechanisms which link these molecular factors to actual, physical changes in cardiac morphology remain unclear.

The aim of this thesis is to identify some of the mechanical forces which drive heart tube assembly in the early chick embryo. A unique feature of this work is the combination of mathematical modeling with ex ovo culture experiments.

Head fold formation is the first step in this process. It sets the stage for early cardiac development by folding the (initially flat) heart fields out-of-plane, enabling them to form a tube along the ventral side of the embryo. Here, we show that head fold formation is driven by forces that originate in the ectoderm, forces that are typically associated with neurulation — the formation of the neural tube.

The primitive heart tube itself then forms as these bilateral heart fields move toward the midline and fuse to construct a straight, muscle-wrapped tube. We show that the endoderm plays a crucial mechanical role during this process. Instead of just serving as a passive, secretory substrate for the crawling mesodermal heart fields, the endoderm actively contracts to pull the heart fields toward the midline. We then investigate how this endodermal contraction is spatially distributed, and how different distributions of contraction might affect the observed morphogenetic deformations during heart tube formation.

Our methods can be readily generalized to other morphogenetic processes, enabling us to investigate how physical forces are organized at the tissue-level to create biological form.

Acknowledgments

Thank you Monica. None of this would have been possible if not for your extraordinary patience and generosity. Starting a family in the midst of graduate school's myriad demands was no small feat. (We did it!) Thank you for your unflagging support through it all. I love you.

Thank you Dr. Taber. The characteristic and winnowing rigor you bring to scientific problems has indelibly shaped my sense of how good science is done, and how I might one day hope to contribute to the field in some small way. I couldn't have hoped for a more responsive or thoughtful graduate advisor. Thank you for affording me the freedom to indulge my (many!) passing curiosities, and for your continued guidance, that ever steady keel, which kept those curiosities from veering too far off course.

I am also grateful for the many people with whom I have shared time in the Taber lab — Benjamen Filas, Alina Oltean, Yunfei Shi, Matthew Wyczalkowski, Dmitry Voronov, Gang Xu, Judy Fee, Patrick Alford, and Ashok Ramasubramanian. Thank you all for the conversations, friendship, and solidarity over the years. Your tough and insightful comments helped sharpen my scientific reasoning and undoubtedly strengthened the work presented here. Also, special thanks to Alina Oltean for her thoughtful comments on early drafts of the beginning and final chapters. (Thanks b.!)

Victor D. Varner

Washington University in Saint Louis
December 2011

This work was supported by grants R01 GM075200 and R01 HL083393 from the National Institutes of Health (L.A.T.), and grant 09PRE2060795 from the American Heart Association (V.D.V.).

For Julia and her unborn sister,

who together have deepened my wonder
at how we come into this world.

Contents

List of Figures

Chapter 1

Introduction

There is something in what it means to be human, which compels us to investigate and wonder at the world around us. Some deeply seated curiosity, some impulse to understand how and why nature is structured the way it is, which is at the heart of the scientific pursuit. In particular, our minds are captured by questions that cast back to the very beginnings of things — the origins of life, the planet, the universe itself. Questions that harken back to that inchoate childhood curiosity — how did I come to be in this world at all?

This impulse is patently clear in many of the central questions of developmental biology: how is the complex body plan of the adult organism formed from a single fertilized egg? How does such an intricate structure emerge from a relatively simple one? And what physical mechanisms accomplish this dramatic event of biological self-assembly?

1.1 Morphogenesis: the creation of biological form

One of the earliest scientific investigations that sought to address these questions was that of Aristotle in 350 BCE. He recorded detailed observations on the contents of hens' eggs at various intervals after the time of laying:

> In the case of the domestic hen, the first signs of the embryo are seen after three days and three nights...the heart is no bigger than just a small blood-spot in the white. This spot beats and moves as though it

> were alive; and from it, as it grows, two vein-like passages with blood in them lead on a twisted course (Aristotle, 1970).

Since his day, generations of biologists have been captivated by this problem, and have wondered (with Aristotle) how it is that biological form is established in the developing embryo — a process known as morphogenesis.

For many of these early investigations, chick embryos proved a convenient model organism, due to their abundant supply and ease of incubation (Balfour, 1881; Lillie, 1952; Patten, 1971). They could be readily cultured ex ovo and were accessible to physical manipulation, making them prime candidates for explanation and grafting experiments (Patten, 1971). During this early era of embryology, many of the experiments performed and much of the language used to describe them were decidedly mechanical in nature (Foster and Balfour, 1883; Lillie, 1952; Bellairs, 1953; Stalsberg and DeHaan, 1969; Patten, 1971).

After the landmark discovery of the structure of DNA by Watson and Crick in 1953 (Watson and Crick, 1953), however, and the subsequent molecular firestorm that revolutionized the field of biology, much of this physical thinking about embryonic development faded from view. In its place, an emerging understanding of the molecular mechanisms and gene regulatory networks which pattern the early embryo and drive the specification and differentiation of different cell types began to take focus. Over time, researchers deduced that biochemical signaling cascades, the primary features of which were conserved across nearly all of biology, interact in vastly complex networks to drive regional gene expression in the embryo (Lodish, 2004).

This rich molecular understanding of development, however, overshadowed many of the still unresolved physical questions about embryogenesis, and for the most part, the field went in other directions. Directions that were hostile at times to such questions entirely. In the 1990's, for example, researchers were informed in a review of a research proposal submitted to the National Institutes of Health that "the physics of how embryos change shape is neither an important nor an interesting question"(Keller, 2002).

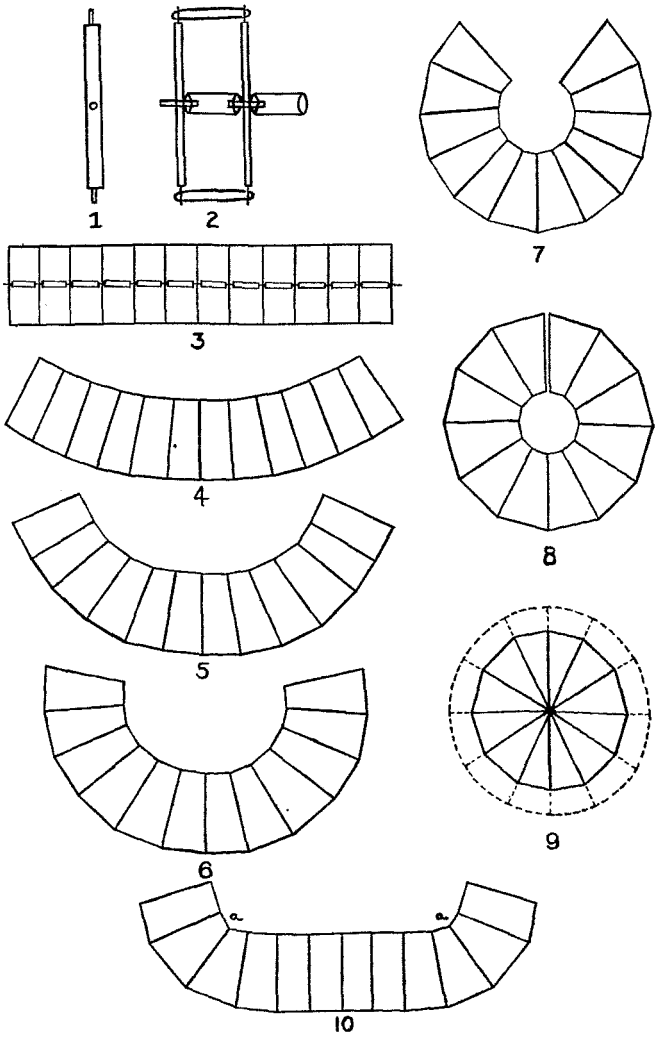

Figure 1.1: (1-3) Physical model of epithelium using brass bars and rubber bands. (4-10) Shape of model resembles invaginating epithelium if one side is under more tension (i.e., has more stretched rubber bands). [From Lewis (1947).]

1.2 Insights from physical modeling

This was certainly not always the case. For over a century, investigators have been interested in and proposed numerous theories about the physical mechanisms of morphogenesis. Still, only a few have been either formulated or tested quantitatively (Koehl, 1990; Taber, 1995). Many of these early investigators used physical simulacra of embryonic tissues to test their ideas by analogy (Weiss, 1939; Thompson, 1942; Lewis, 1947). Lewis (1947), for instance, constructed a physical model of an epithelium using brass bars and rubber bands to test their hypotheses about the mechanical forces driving invagination (Fig. 1.1). These models can provide valuable qualitative insight into the physics of a problem and can often suggest new ideas for experiments, but care must be taken to collect further quantitative experimental data in order to test the predictions of such a model.

Gathering this quantitative mechanical data in embryos, however, is a challenging task (Koehl, 1990; Davidson et al., 2009; Wozniak and Chen, 2009). Still, experimental ingenuity by pioneering investigators like Waddington, Selman and DeHaan established a clear tradition for this kind of work in embryology (Waddington, 1939; Selman, 1958; DeHaan, 1963; Stalsberg and DeHaan, 1968).

Prompted by a suggestion from Waddington, Selman (1958) measured the forces generated during neurulation by positioning "two small iron dumb-bells[1]...on the neural plate [of both newt and axolotl embryos] parallel to and against the neural folds"(Fig. 1.2). The embryos were then placed in a magnetic field of known magnitude, and the forces required to resist neural tube closure could be calculated.

A decade later, Stalsberg and DeHaan (1968) used a combination of experiments and mathematical modeling (rather presciently) to suggest a physical mechanism for foregut formation. They quantified tissue displacements by attaching iron oxide particles to the endoderm of early chick embryos. The embryos were then cultured ex ovo and photographed at various timepoints (Fig. 1.3a). A simple 2D model was then

[1]Interestingly, these dumb-bells were collected by scouring though a small pile of iron shot pellets. The majority of the these particles were spherical, but occasionally two spherical pellets were connected by a thin cylindrical shaft to create a dumb-bell shape (Selman, 1958).

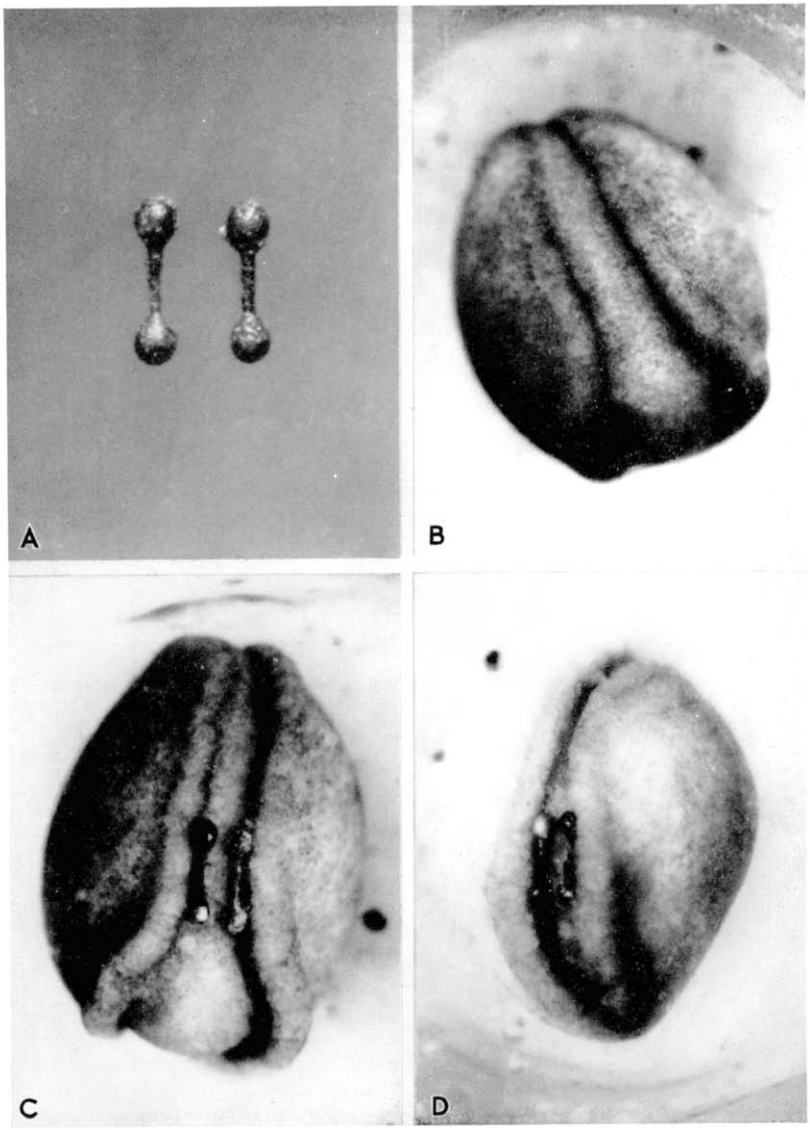

Figure 1.2: Iron dumb-bells placed along neural folds to measure forces of neurulation. When placed in a magnetic field of known magnitude, the forces required to resist neurulation could be calculated. [From Selman (1958).]

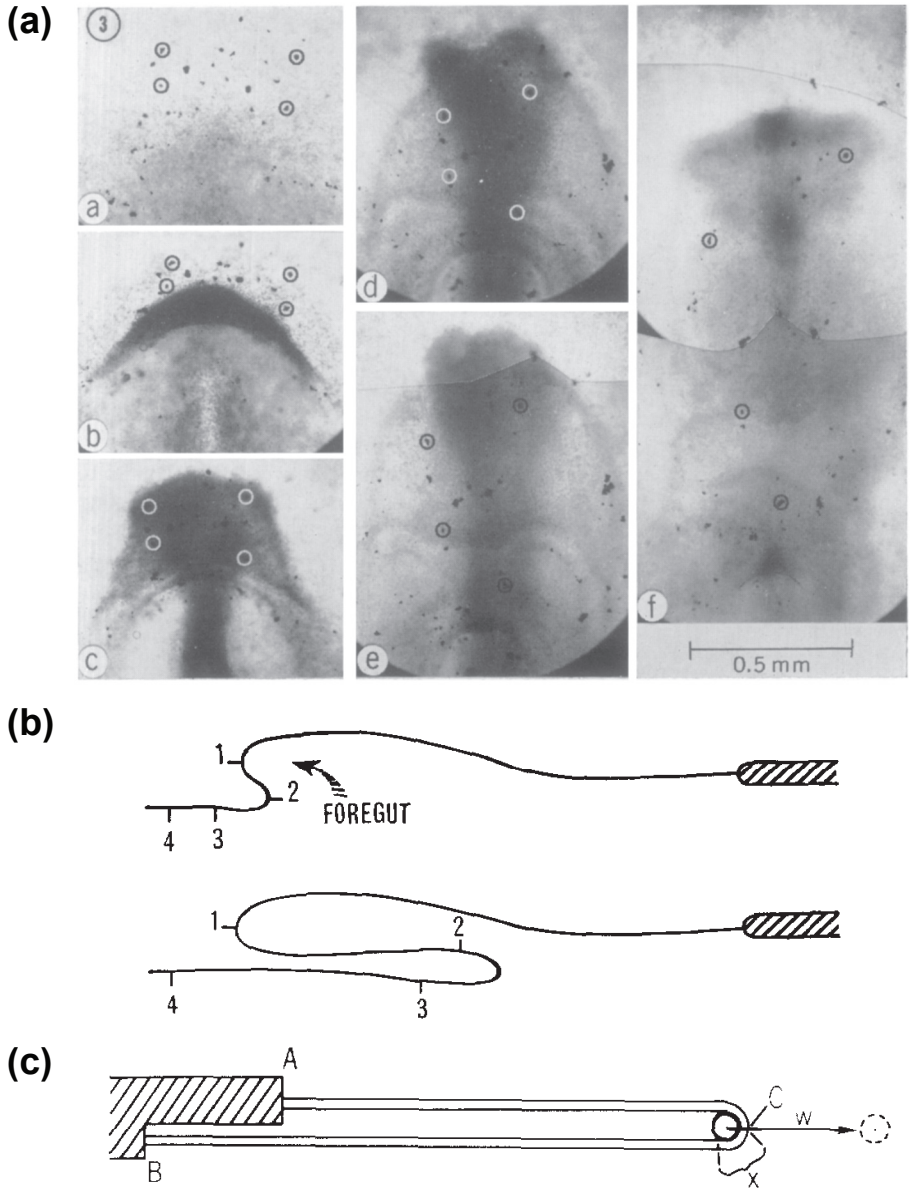

Figure 1.3: (a) Sequential images of early chick embryo marked with iron oxide particles, showing endodermal movements during foregut formation. (b) Schematics of midsagittal sections of the endoderm during foregut formation. Points 1-4 represent material points on the tissue. (c) Theoretical model for foregut formation. [From Stalsberg and DeHaan (1968).]

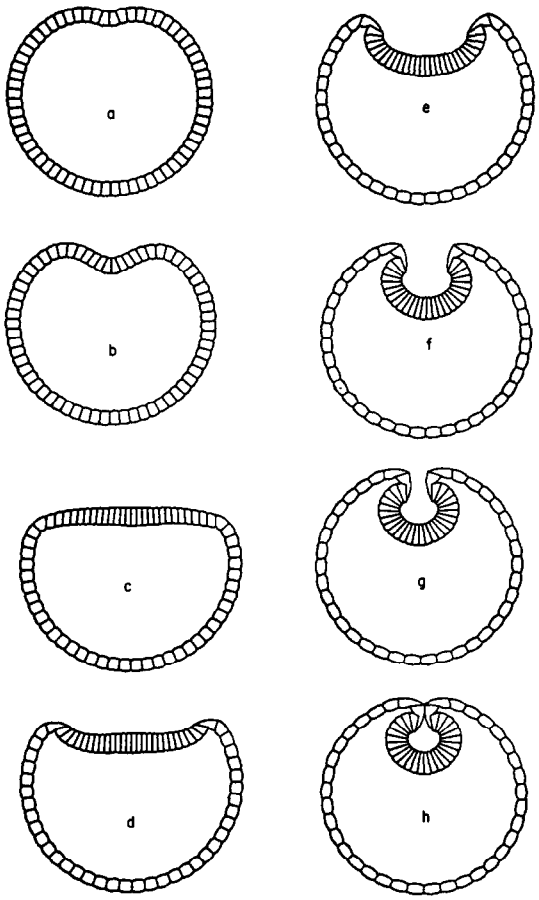

Figure 1.4: Computer simulation of amphibian neurulation. [From Odell et al. (1981).]

used to suggest mechanical forces that might be driving the observed tissue motion (Fig. 1.3b,c).

This transition from physical (i.e., actual material) models to mathematical simulations was hastened by the advent of computers (Keller, 2002) and is perhaps best epitomized by the classic work of Odell et al. (1981). They developed a 2D model for epithelial folding, where each cell is treated as a network of viscoelastic truss-like elements that simulate active and passive cytoskeletal components. The authors tested the idea that cell stretching might trigger cytoskeletal contraction, and their results demonstrated that such a mechanism could produce the shape changes observed during both Drosophila gastrulation and amphibian neurulation (Fig. 1.4).

Since then, groups of physical scientists and engineers have used a variety of mathematical frameworks to model the physics of developing tissues (reviewed in Taber, 1995; Davidson et al., 2010), including nonlinear elasticity (Taber, 2001), the Cellular Potts method (Graner and Glazier, 1992; Glazier and Graner, 1993), and vertex modeling (Weliky and Oster, 1990). This work has helped identify some of the mechanical forces that drive cortical folding (Xu et al., 2010), cardiac c-looping (Voronov et al., 2004; Ramasubramanian et al., 2006), convergent extension (Weliky et al., 1991; Davidson et al., 2010), amphibian neurulation (Chen and Brodland, 2008), Drosophila germband extension (Rauzi et al., 2008) and ventral furrow formation (Muñoz et al., 2007), cell sorting (Krieg et al., 2008), and epithelial packing (Farhadifar et al., 2007).

Recent experimental work has suggested a possible regulatory role for mechanical forces during development (Farge, 2003; Bertet et al., 2004; Desprat et al., 2008; Fernandez-Gonzalez et al., 2009; Pouille et al., 2009; Filas et al., 2011), which has garnered new attention to these modeling efforts amongst experimental biologists. Moreover, new advances in timelapse microscopy have made dynamic studies of tissue morphogenesis possible (Kiehart et al., 2000; Hutson et al., 2003; Blankenship et al., 2006; Blanchard et al., 2009; Butler et al., 2009; Martin et al., 2010). The detail with which these dramatic and beautifully orchestrated tissue deformations can now be observed has made questions about the mechanical forces which may be driving them seem almost inevitable.

This has triggered a resurgent interest in the mechanics of morphogenesis. The inherently interdisciplinary nature of these problems has brought together new groups of biologists, physical scientists, and engineers, who hope to combine experiments with physical or computational modeling to shed some light on the physics of embryonic development.

1.3 How the heart is shaped

As observed by Aristotle, the heart is first mechanically functioning organ to form in the developing embryo. The physical forces that drive its formation, however, remain poorly understood. Cardiac development in the chick (conveniently) parallels that in

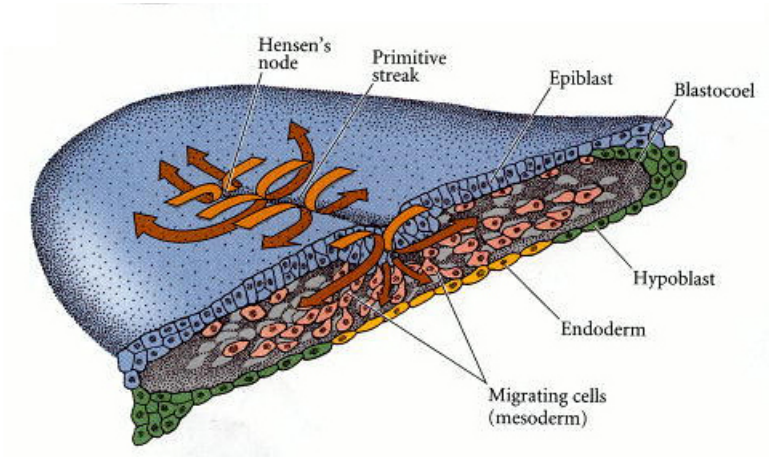

Figure 1.5: Schematic of avian gastrulation. [From Gilbert (2000).]

humans, and the chick has become a well established model organism to study early cardiogenesis (DeHaan, 1967).

Based largely on embryonic morphology, Hamburger and Hamilton (1951) have partitioned the 21-day incubation period of the chick into 46 different stages. During the first day of development, the early embryo is initially organized as a flat sheet of cells called the blastoderm (Patten, 1971). During gastrulation, the cardiac progenitor cells ingress through the primitive streak and take up residence in the lateral plate mesoderm (Fig. 1.5) (Rosenquist and DeHaan, 1966; Garcia-Martinez and Schoenwolf, 1993; Cui et al., 2009).

By Hamburger-Hamilton (HH) stage 8, the lateral mesoderm has split into splanchnic and somatic layers, which enclose the growing pericardial coelom (Fig. 1.6a) (Linask, 2003). The cardiogenic mesoderm is confined to the splanchnic mesoderm, where the epithelium begins to thicken (Fig. 1.6b-d) (Stalsberg and DeHaan, 1969; Kirby, 2007).

The heart fields then move toward the ventral midline, rotating as their lateral edges come into contact behind the head fold (Fig. 1.7) (Stalsberg and DeHaan, 1969; Linask and Lash, 1986; Kirby, 2007; Abu-Issa and Kirby, 2008; Cui et al., 2009). They fuse in both anterior and posterior directions (Moreno-Rodriguez et al., 2006) to form a relatively straight heart tube that remains open along its dorsal side. Extracelluar matrix (or cardiac jelly), secreted by the primitive myocardium, is believed to inflate

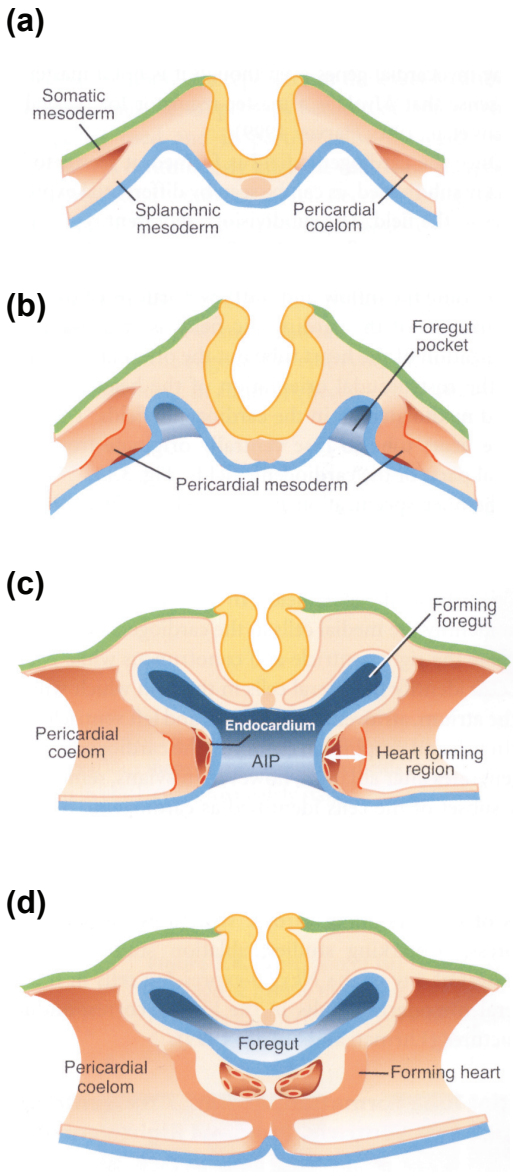

Figure 1.6: Transverse schematics of heart tube formation in the early chick embryo. [From Kirby (2007).]

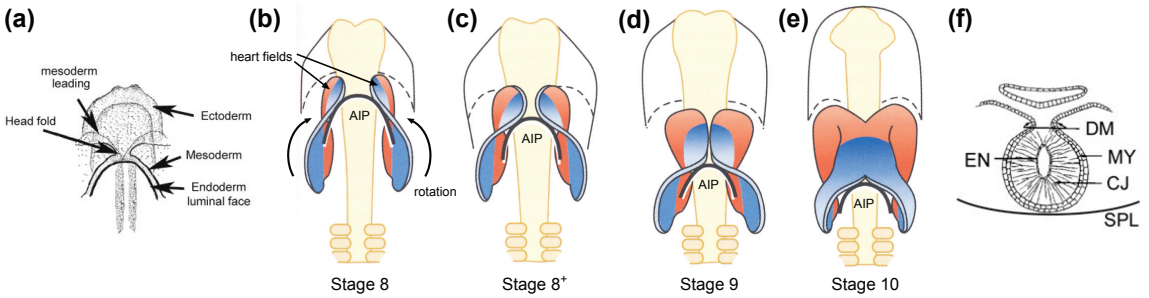

Figure 1.7: (a) Schematic of fusing heart fields. [From Moreno-Rodriguez et al. (2006).] (b-e) Formation of primitive heart tube. AIP=anterior intestinal portal (i.e., posterior opening of the foregut). [From Kirby (2007).] (f) Schematic cross-section of stage 10 chick heart ((EN = endocardium; MY = myocardium; CJ = cardiac jelly; DM = dorsal mesocardium; SPL = splanchnopleure.) [From Manasek et al. (1983).]

the elongating heart tube (de Jong et al., 1990), giving it a U-shaped transverse cross-section (Fig. 1.6d). Initially, the tube is composed of three layers: an outer layer of myocardium, a relatively thick middle layer of cardiac jelly, and an inner layer of endocardium (Fig. 1.7f).

Although many of the genetic and molecular factors integral to this process have been identified (Olson and Srivastava, 1996; Yutzey and Kirby, 2002; Buckingham et al., 2005; Abu-Issa and Kirby, 2007), the biophysical mechanisms which drive heart tube assembly remain poorly characterized (Taber, 2006).

1.4 Applications for tissue engineering

Understanding how embryonic tissues are constructed during normal development crucially underpins the field of tissue engineering, which seeks to recapitulate this process in vitro. Since the heart continuously functions as a mechanical pump while it is still being formed in the embryo, researchers have long speculated that the mechanical loads experienced by the heart during development may play a regulatory role in its morphogenesis (Bartman and Hove, 2005). This idea is supported by recent work which shows that mechanical loading can regulate regional gene expression during early Drosophila development (Farge, 2003; Desprat et al., 2008). Moreover, emerging evidence has indicated a regulatory role for matrix elasticity during stem

cell differentiation (Engler et al., 2006), and mechanical tension has been shown to determine branching sites in engineered mammary epithelial tubules (Gjorevski and Nelson, 2010a).

While it is interesting to contemplate the possible feedback between mechanics and form during cardiogenesis, this only makes the challenge facing cardiac tissue engineers all the more daunting, and underscores the importance of understanding the physical forces which form the heart.

1.5 Advances presented in dissertation

Herein, we seek to characterize some of these mechanical forces – in particular, those that drive the process of heart tube assembly.

Head fold formation sets the stage for early cardiac development by folding the (initially flat) heart fields out-of-plane, enabling them to form a tube along the ventral side of the embryo. The primitive heart tube itself then forms as these heart fields move toward the midline and fuse behind the head fold to construct a straight, muscle-wrapped tube. In this work, we characterize some of the mechanical forces that physically drive both of these processes.

A unique feature of this work is the combination of mathematical modeling with ex ovo culture experiments. Mathematical models offer particular insight in studies of morphogenesis, as growing embryonic tissues undergo complex finite deformations. This results in highly nonlinear problems that (often) elude intuition and require computational techniques. These models enable us to test whether a given set of forces could plausibly generate the tissue deformations observed during development.

We use a continuum mechanical framework to model growing soft tissues. In chapter 2, we broadly outline our theoretical methods. This treatment is only introductory, and the details of any particular model are included in later chapters.

In chapter 3, we present a method for measuring stress distributions in epithelia, similar to the hole drilling method for determining residual stresses in traditional

engineering materials. This technique can also be used to estimate the nonlinearity of the constitutive response for the material.

In chapter 4, we identify some of the tissue-level forces that drive head fold morphogenesis. Our results suggest that a group of forces, typically associated with neurulation, work in tandem to collectively shape the forming head fold. This is the first major 3D structure to arise in the early chick embryo, and, by bending the planar blastoderm out-of-plane, its formation sets the stage for both heart tube and foregut morphogenesis.

It is generally accepted that heart field motion toward the midline is primarily due to active migration of the cardiogenic mesoderm over the underlying endoderm. In chapter 5, however, we indicate a crucial mechanical role for the endoderm during this process. Instead of just serving as a passive, secretory substrate for the crawling mesoderm, the endoderm actively contracts to pull the heart fields toward the midline, where they fuse to form the heart tube.

Then, in chapter 6, we investigate how this endodermal contraction is spatially distributed, and how different distributions of contraction might affect the observed morphogenetic deformations. Moreover, we identify a gradient in the passive material properties of the tissue around the AIP, which gives us new insight into how tissue stiffness and contractility are spatially distributed as the heart tube forms.

Finally, in chapter 7, we consider future directions for this research, and comment on some the exciting new interdisciplinary work that is seeking to connect physical mechanisms of morphogenesis with the underlying genetics and cell biology.

Chapter 2

Theoretical background

We use a continuum mechanical approach to model the deformations of embryonic tissues. Here, only a very basic and introductory treatment of these ideas is presented. Interested readers should consult Taber (2004) or Holzapfel (2000) for a more comprehensive presentation of the material.

A continuum mechanical framework considers only the macroscopic behavior of a material. As such, any discrete microscopic material structures[2] are lumped into continuous field properties. The material is thus treated as a continuum of particles. This approximation makes the problem of characterizing the deformation of a material more tractable[3], but assumes that the deformations of interest occur at length scales sufficiently greater than that of the discrete microscopic material structure. Also, unlike the Cellular Potts and vertex models used by others to model embryonic tissues, this continuum approach does not (necessarily) make explicit assumptions about the directions along which mechanical loads must be carried by the material, or which constituent parts of the material must bear those loads.

In general soft biological materials undergo large strains and exhibit nonlinear, viscoelastic constitutive behavior. After unloading, that is, most tissues dissipate some of the energy stored within them during deformation[4]. As a first approximation, however, we can assume a pseudoelastic constitutive response for many soft biological tissues (Fung et al., 1979). Under this assumption, different elastic mechanical properties are used to characterize the material during loading and unloading.

[2]All matter after all is composed of atoms, which contain mostly empty space.

[3]Think atomistic simulation of an entire tissue, let alone an entire embryo.

[4]During mechanical tests of biological materials, this is evidenced by a hysteresis loop between the loading and unloading force-deflection curves.

Each problem in continuum mechanics is governed by three sets of equations:

- The kinematic (or strain-displacement) relations, which are purely geometrical and analyze the deformation of a material.
- The equations of motion (i.e., Newton's laws of motion).
- The constitutive relations, which relate the elastic deformation of a material to the internal stresses (or forces).

2.1 Analysis of deformation

Consider an undeformed (or reference) body[5] B that deforms into the body b, where the point $P(X, Y)$ on B moves to the location $p(x, y)$ on b, and the point Q maps to q. (Fig. 2.1).

The position vectors[6]

$$\begin{aligned} \mathbf{R} &= X_i \mathbf{e_i} \\ \mathbf{r} &= x_i \mathbf{e_i} \end{aligned} \tag{2.1}$$

define points in the undeformed and deformed configurations, respectively, and there is a one-to-one mapping between all points on B and b, such that

$$\begin{aligned} \mathbf{r} &= \mathbf{r}(\mathbf{R}) \\ \mathbf{R} &= \mathbf{R}(\mathbf{r}) \end{aligned} . \tag{2.2}$$

The differential line element $d\mathbf{R} = dX_i \mathbf{e_i}$ on B deforms and rotates into $d\mathbf{r} = dx_i \mathbf{e_i}$ on b. This transformation is defined by the second-order tensor $\mathbf{F}$, which is defined by

$$d\mathbf{r} = \mathbf{F} \cdot d\mathbf{R} \tag{2.3}$$

[5] When possible, uppercase letters are used for quantities defined in the reference configuration, and lowercase letters for quantities defined in the deformed configuration

[6] Unless otherwise noted, we employ the Einstein summation convention for repeated indices (e.g., $a_i b_i = \sum_{i=1}^{3} a_i b_i = a_1 b_1 + a_2 b_2 + a_3 b_3$).

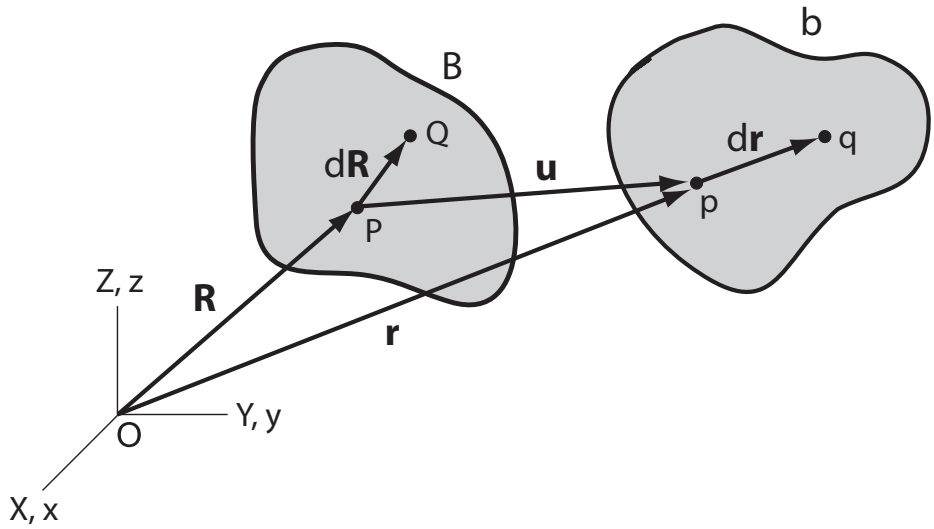

Figure 2.1: Deformation of undeformed body B into deformed body b. [Modified from Taber (2004).]

and termed the deformation gradient tensor. Using our definitions of the differential line elements $d\mathbf{R}$ and $d\mathbf{r}$, we can show that

$$dx_i = F_{ij} dX_j, \tag{2.4}$$

and from our one-to-one mapping in Eq. (2.2) that

$$\mathbf{F} = F_{ij}\mathbf{e_i}\mathbf{e_j} \quad \text{where} \quad F_{ij} = \frac{\partial x_i}{\partial X_j}. \tag{2.5}$$

If we use the gradient operator in the undeformed configuration

$$\boldsymbol{\nabla} = \mathbf{e_i}\frac{\partial}{\partial X_i}, \tag{2.6}$$

and, substituting with Eq. (2.1), consider

$$\begin{aligned} \boldsymbol{\nabla}\mathbf{r} = \left(\mathbf{e_i}\frac{\partial}{\partial X_i}\right)(x_j\mathbf{e_j}) &= \frac{\partial x_j}{\partial X_i}\mathbf{e_i}\mathbf{e_j} \\ &= \frac{\partial x_i}{\partial X_j}\mathbf{e_j}\mathbf{e_i} \\ &= \mathbf{F}^T, \end{aligned} \tag{2.7}$$

we can take, in coordinate-free form,

$$\mathbf{F} = (\boldsymbol{\nabla}\mathbf{r})^T . \tag{2.8}$$

Note that, in general, $\mathbf{F}$ is not a symmetric tensor. In addition, since it both deforms and rotates $d\mathbf{R}$ into $d\mathbf{r}$, it still contains rigid body motion, and thus is not purely a measure of deformation.

To remove rigid body rotation, we consider the squared lengths dS^2 and ds^2 of the line elements $d\mathbf{R}$ and $d\mathbf{r}$, respectively

$$\begin{aligned} dS^2 &= d\mathbf{R} \cdot d\mathbf{R} \\ ds^2 &= d\mathbf{r} \cdot d\mathbf{r} \end{aligned} . \tag{2.9}$$

Substituting Eq. (2.3) into Eq. $(2.9)_2$ yields

$$ds^2 = \left(d\mathbf{R} \cdot \mathbf{F}^T\right) \cdot (\mathbf{F} \cdot d\mathbf{R}) = d\mathbf{R} \cdot \left(\mathbf{F}^T \cdot \mathbf{F}\right) \cdot d\mathbf{R}. \tag{2.10}$$

In this equation,

$$\mathbf{C} = \mathbf{F}^T \cdot \mathbf{F} \tag{2.11}$$

is defined as the right Cauchy-Green deformation tensor. By taking $\mathbf{C}^T = \left(\mathbf{F}^T \cdot \mathbf{F}\right)^T = \mathbf{F}^T \cdot \left(\mathbf{F}^T\right)^T = \mathbf{F}^T \cdot \mathbf{F} = \mathbf{C}$, we can show that $\mathbf{C}$ is a symmetric tensor.

Then, consider the difference in squared lengths

$$\begin{aligned} ds^2 - dS^2 &= d\mathbf{R} \cdot \left(\mathbf{F}^T \cdot \mathbf{F}\right) \cdot d\mathbf{R} - d\mathbf{R} \cdot d\mathbf{R} \\ &= d\mathbf{R} \cdot (\mathbf{C} - \mathbf{I}) \cdot d\mathbf{R}, \end{aligned} \tag{2.12}$$

where $\mathbf{I}$ is the identity tensor.

The Lagrangian strain tensor $\mathbf{E}$ is defined as

$$ds^2 - dS^2 = 2\ d\mathbf{R} \cdot \mathbf{E} \cdot d\mathbf{R}. \tag{2.13}$$

Comparing this to Eq. (2.12, we then find that

$$\mathbf{E} = \frac{1}{2}\left(\mathbf{C} - \mathbf{I}\right) = \frac{1}{2}\left(\mathbf{F}^T \cdot \mathbf{F} - \mathbf{I}\right). \tag{2.14}$$

If we take the displacement vector $\mathbf{u} = \mathbf{r} - \mathbf{R}$ between the point P in B and its image in p in b (Fig. 2.1), using Eq. (2.8) we can further show that

$$\mathbf{F}^T = \boldsymbol{\nabla}\mathbf{r} = \boldsymbol{\nabla}\left(\mathbf{R} + \mathbf{u}\right), \tag{2.15}$$

where

$$\boldsymbol{\nabla}\mathbf{R} = \left(\mathbf{e_i}\frac{\partial}{\partial X_i}\right)\left(X_j\mathbf{e_j}\right) = \frac{\partial X_j}{\partial X_i}\mathbf{e_i}\mathbf{e_j} = \mathbf{e_i}\mathbf{e_i} = \mathbf{I}. \tag{2.16}$$

Thus,

$$\mathbf{F}^T = \mathbf{I} + \boldsymbol{\nabla}\mathbf{u}. \tag{2.17}$$

Substituting this into Eq. (2.14) we can then calculate the strain-displacement relation

$$\begin{aligned}
\mathbf{E} &= \frac{1}{2}\left(\mathbf{F}^T \cdot \mathbf{F} - \mathbf{I}\right) \\
&= \frac{1}{2}\left[\left(\mathbf{I} + \boldsymbol{\nabla}\mathbf{u}\right) \cdot \left(\mathbf{I}^T + \left(\boldsymbol{\nabla}\mathbf{u}\right)^T\right) - \mathbf{I}\right] \\
&= \frac{1}{2}\left[\mathbf{I} + \boldsymbol{\nabla}\mathbf{u} + \left(\boldsymbol{\nabla}\mathbf{u}\right)^T + \left(\boldsymbol{\nabla}\mathbf{u}\right) \cdot \left(\boldsymbol{\nabla}\mathbf{u}\right)^T - \mathbf{I}\right] \\
\mathbf{E} &= \frac{1}{2}\left[\boldsymbol{\nabla}\mathbf{u} + \left(\boldsymbol{\nabla}\mathbf{u}\right)^T + \left(\boldsymbol{\nabla}\mathbf{u}\right) \cdot \left(\boldsymbol{\nabla}\mathbf{u}\right)^T\right]
\end{aligned} \tag{2.18}$$

If small deformations are assumed, the final term in Eq. $(2.18)_4$ can be neglected. Here, however, we are interested in materials that undergo large (or finite) changes in shape and must consider the full nonlinear form.

2.2 Analysis of stress

Mechanical stress is a normalized measure for loading and, in general, describes a force vector acting over a unit area. For small deformations, changes in area become

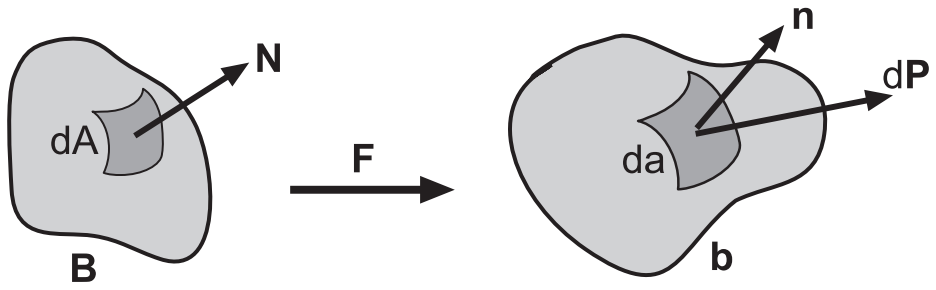

Figure 2.2: Deformation of differential area element $d\mathbf{A}$ in B into $d\mathbf{a}$ in b. [From Taber (2004).]

negligible, and whether we normalize forces with respect to the undeformed or deformed area is moot. When the deformations are large, however, distinctions about the area over which forces are being normalized must be made.

Consider a differential area element $d\mathbf{A}$ within B that, under the influence of the surface traction $d\mathbf{P}$, deforms into the area element $d\mathbf{a}$ (Fig. 2.2).

If we take

$$\begin{aligned} d\mathbf{A} &= \mathbf{N}\ dA \\ d\mathbf{a} &= \mathbf{n}\ da \end{aligned}, \tag{2.19}$$

where $\mathbf{N}$ and $\mathbf{n}$ are unit vectors normal to the differential areas dA and da, respectively, we can define the true traction vector

$$\mathbf{T}^{(\mathbf{n})} = \frac{d\mathbf{P}}{da} \tag{2.20}$$

and the Cauchy stress formula

$$\mathbf{T}^{(\mathbf{n})} = \mathbf{n} \cdot \boldsymbol{\sigma}, \tag{2.21}$$

where $\boldsymbol{\sigma}$ is called the Cauchy (or true) stress tensor.

We can also define a (pseudo)force vector $d\tilde{\mathbf{P}}$ that acts on $d\mathbf{A}$ (Fig. 2.3) , by the relation

$$d\mathbf{P} = \mathbf{F} \cdot d\tilde{\mathbf{P}} = d\tilde{\mathbf{P}} \cdot \mathbf{F}^T. \tag{2.22}$$

We call this a (pseudo)force, since it is fictitious (or non-physical). In actuality, it is the force $d\mathbf{P}$ that acts over the deformed area $d\mathbf{a}$ in the material.

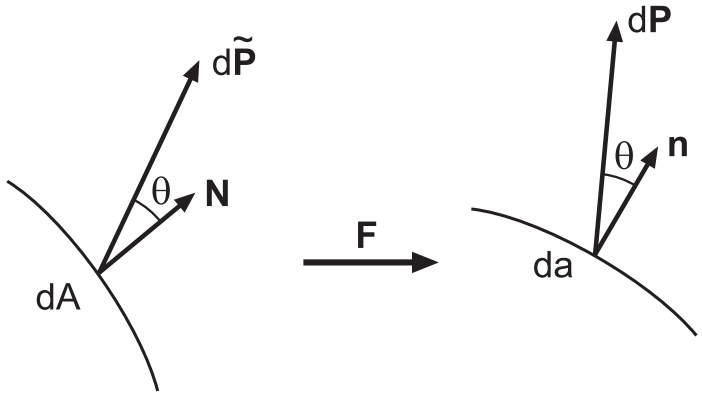

Figure 2.3: Force vector $d\mathbf{P}$ acting on deformed area da and (pseudo)force vector $d\tilde{\mathbf{P}}$ acting on undeformed area dA. [From Taber (2004).]

Then, similarly, using Eqns. $(2.19)_1$ and (2.22), we can define the (pseudo)traction vectors

$$\begin{aligned} \mathbf{T}^{(\mathbf{N})} &= \frac{d\mathbf{P}}{dA} \\ \tilde{\mathbf{T}}^{(\mathbf{N})} &= \frac{d\tilde{\mathbf{P}}}{dA} \end{aligned} \quad , \tag{2.23}$$

and, analogously, the first Piola-Kirchhoff stress tensor $\mathbf{t}$ and second Piola-Kirchhoff stress tensor $\mathbf{s}$

$$\begin{aligned} \mathbf{T}^{(\mathbf{N})} &= \mathbf{N} \cdot \mathbf{t} \\ \tilde{\mathbf{T}}^{(\mathbf{N})} &= \mathbf{N} \cdot \mathbf{s} \end{aligned} \quad . \tag{2.24}$$

Considering now Eqns. (2.19)–(2.24), we can show that

$$d\mathbf{P} = d\mathbf{a} \cdot \boldsymbol{\sigma} = d\mathbf{A} \cdot \mathbf{t} = d\mathbf{A} \cdot \mathbf{s} \cdot \mathbf{F}^T. \tag{2.25}$$

The deformed and undeformed areas are related by the expression

$$d\mathbf{a} = J \; d\mathbf{A} \cdot \mathbf{F}^{-1} \tag{2.26}$$

where $J = \det \mathbf{F}$. Using this relation, then, we can take

$$\boldsymbol{\sigma} = J^{-1}\mathbf{F} \cdot \mathbf{t} = J^{-1}\mathbf{F} \cdot \mathbf{s} \cdot \mathbf{F}^T, \tag{2.27}$$

which allows us to transform between any of the three different stress tensors.

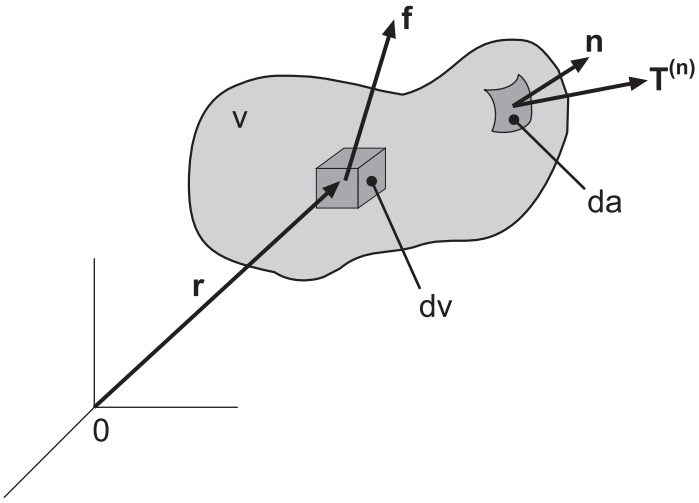

Figure 2.4: Forces acting on deformed body. [From Taber (2004).]

Now, if we consider a deformed body subjected to an assortment of body forces $\mathbf{f}(\mathbf{r}, t)$ and surface tractions $\mathbf{T}^{(\mathbf{n})}(\mathbf{r}, t)$ (Fig. 2.4), both the body and each of its individual constituent parts must obey Newton's laws of motion. Applying the conservation of linear momentum, we get

$$\int_a \mathbf{T}^{(\mathbf{n})}\, da + \int_v \mathbf{f}\, dv = \frac{d}{dt}\int_v \mathbf{v}\rho\, dv \tag{2.28}$$

where ρ is the mass density and $\mathbf{v}$ is the velocity of the center of mass of the differential volume element dv.

Using Eq. (2.21) and then applying the divergence theorem (cite?), the first term in this equation becomes

$$\int_a \mathbf{T}^{(\mathbf{n})}\, da = \int_a \mathbf{n}\cdot\boldsymbol{\sigma}\, da = \int_v \bar{\boldsymbol{\nabla}}\cdot\boldsymbol{\sigma}\, dv, \tag{2.29}$$

where $\bar{\boldsymbol{\nabla}}$ is the gradient operator in the deformed configuration.

Substituting this back into Eq. (2.28) and assuming conservation of mass, we get

$$\int_v \left(\bar{\boldsymbol{\nabla}}\cdot\boldsymbol{\sigma} + \mathbf{f} - \rho\frac{d\mathbf{v}}{dt}\right)\, dv = \mathbf{0}. \tag{2.30}$$

Since this must hold for arbitrary dv,

$$\bar{\boldsymbol{\nabla}} \cdot \boldsymbol{\sigma} + \mathbf{f} = \rho \frac{d\mathbf{v}}{dt}. \tag{2.31}$$

During morphogenesis, however, the deformations occur slowly enough that the inertial terms in these equations can be neglected, as well as any gravitational effects. The problem is thus a quasistatic one, and equilibrium can be enforced by

$$\bar{\boldsymbol{\nabla}} \cdot \boldsymbol{\sigma} = \mathbf{0}. \tag{2.32}$$

Similarly, using a Lagrangian description, the equilibrium equation takes the form

$$\boldsymbol{\nabla} \cdot \mathbf{t} = \mathbf{0}. \tag{2.33}$$

2.3 Constitutive equations

Deformation and mechanical stress are linked by the constitutive properties of the material, which are determined experimentally. If a material is assumed to be pseudoelastic, then any work done on the body is stored as strain energy. We can then define the scalar strain-energy density function W per unit volume. Owing to thermodynamic considerations (Taber, 2004), the constitutive equation then takes the form

$$\mathbf{s} = \frac{\partial W}{\partial \mathbf{E}}, \tag{2.34}$$

and materials describable by this equation are termed hyperelastic. Using Eq. (2.27, Eq. (2.34) can also be expressed in terms of the Cauchy and first Piola-Kirchhoff stress tensors:

$$\begin{aligned} \boldsymbol{\sigma} &= J^{-1}\ \mathbf{F} \cdot \frac{\partial W}{\partial \mathbf{E}} \cdot \mathbf{F}^T \\ \mathbf{t} &= \frac{\partial W}{\partial \mathbf{E}} \cdot \mathbf{F}^T \end{aligned} \quad . \tag{2.35}$$

We can alternatively express W in terms of $\mathbf{F}$, and these two constitutive equations then take the form:

$$\begin{aligned} \boldsymbol{\sigma} &= J^{-1}\ \mathbf{F} \cdot \frac{\partial W}{\partial \mathbf{F}^T} \\ \mathbf{t} &= \frac{\partial W}{\partial \mathbf{F}^T} \end{aligned} \quad . \tag{2.36}$$

Many soft tissues are assumed to be incompressible (i.e., $J = \det \mathbf{F} = 1$) (cite?). In such cases, the normal stress components may only be solved up to a hydrostatic pressure p, and we must include a $-p\,\mathbf{I}$ term in the Cauchy stress equation. Eq. $(2.36)_1$ then becomes

$$\boldsymbol{\sigma} = J^{-1}\ \mathbf{F} \cdot \frac{\partial W}{\partial \mathbf{F}^T} - p\ \mathbf{I}, \tag{2.37}$$

and using Eq. (2.27) and $J = 1$, the first and second Piola-Kirchhoff stress tensors are given by

$$\begin{aligned} \mathbf{t} &= \mathbf{F}^{-1} \cdot \boldsymbol{\sigma} = \frac{\partial W}{\partial \mathbf{E}} \cdot \mathbf{F}^T - p\ \mathbf{F}^{-1} = \frac{\partial W}{\partial \mathbf{F}^T} - p\ \mathbf{F}^{-1} \\ \mathbf{s} &= \mathbf{F}^{-1} \cdot \boldsymbol{\sigma} \cdot \mathbf{F}^{-T} = \frac{\partial W}{\partial \mathbf{E}} - p\ \mathbf{F}^{-1} \cdot \mathbf{F}^{-T} \end{aligned} \quad . \tag{2.38}$$

2.4 Growth

We use the Rodriguez et al. (1994) theory of finite volumetric growth to model the mechanics of growing soft tissues. The total deformation gradient tensor $\mathbf{F}$ is decomposed into both a growth tensor $\mathbf{G}$ and an elastic deformation gradient tensor $\mathbf{F}^*$ (Fig. 2.5) by

$$\mathbf{F} = \mathbf{F}^* \cdot \mathbf{G}. \tag{2.39}$$

Similar to thermal expansion, the zero-stress state of each (infinitesimal) material element changes as it grows uniformly according to $\mathbf{G}$. Mechanical stress then depends on only on $\mathbf{F}^*$, which both enforces geometric compatibility between material elements and governs how they deform under any applied loads.

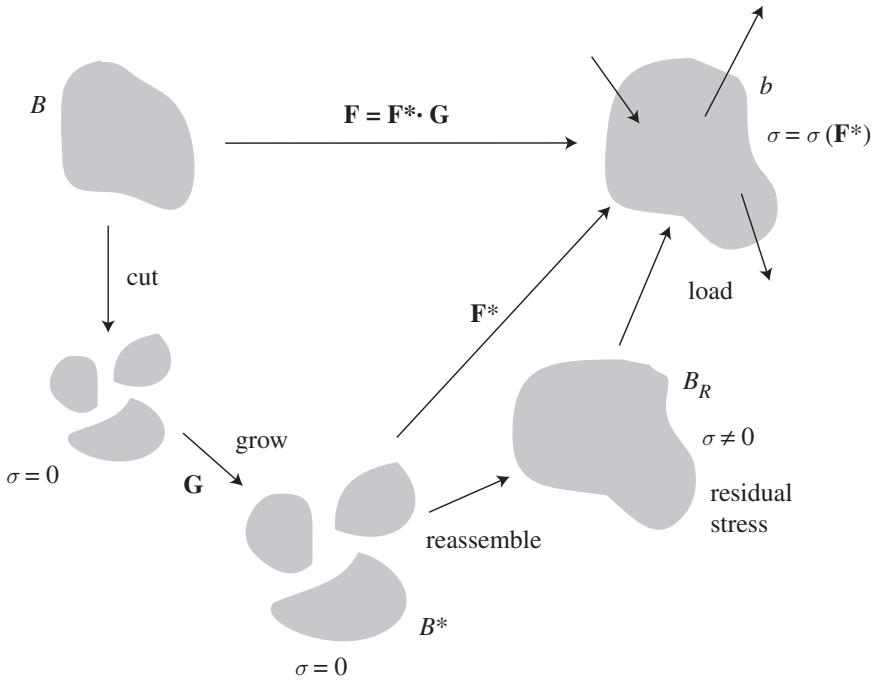

Figure 2.5: Configurations for a growing body: reference state B; current zero-stress state B^*; current unloaded state B_R; current loaded state b. $\mathbf{G}$ represents the growth tensor; $\mathbf{F}^*$, the elastic deformation gradient tensor, and $\mathbf{F}$, the total deformation gradient tensor. [From Taber (2009).]

The strain energy density function W therefore depends on $\mathbf{F}^*$ instead of $\mathbf{F}$ as it does for a passive (or non-growing) material. Then, for an incompressible material (where $J^* = 1$) the Cauchy stress equation becomes

$$\boldsymbol{\sigma} = \mathbf{F}^* \cdot \frac{\partial W}{\partial \mathbf{F}^{*T}} - p\,\mathbf{I}. \tag{2.40}$$

Chapter 3

On measuring stress distributions in epithelia

Summary

Many biological tissues are organized as epithelia (i.e., thin cell sheets). Herein, we present a technique to estimate the stress distribution and local material properties in an epithelial membrane. Circular holes are perforated through the tissue to determine the principal stretch ratios; experimentally measured changes in hole geometry are used in combination with finite element modeling to evaluate the stresses and constitutive response. The method is demonstratively applied to the embryonic chick blastoderm, since mechanical stresses have been identified as potential regulators of early development. Due to its small scale, other more traditional mechanical tests have proven intractable for this tissue.

3.1 Introduction

Many biological tissues adaptively respond to changes in their mechanical environment. Although the mechanisms that drive this adaptation are not fully understood, there is ample evidence suggesting a linkage between tissue growth and mechanical stress (Taber, 1995). Epithelia (i.e., thin cell sheets) are commonplace in both developing and mature organisms. In fact, so indispensable is its role in biology that the epithelium was likely the first true tissue type to arise during evolution (Davies,

2005). Here, we present a technique for estimating anisotropic distributions of stress in epithelia. Such a method is necessary to develop a clearer understanding of the apparent relationship between growth and stress in these tissues.

Our technique is a variation of the hole-drilling method for measuring residual stress, which was first proposed in the 1930s (Mathar, 1934; Rendler and Vigness, 1966). Briefly, a circular drill is used to bore a small hole into the surface of a material. The deformation around the hole is measured with strain gages and used, with the material's constitutive properties, to determine the stress field. Use of this method, however, is generally limited to structures of Hookean material that undergo small deformations. By contrast, biological tissues often undergo large strains and have been shown to exhibit nonlinear constitutive behavior (Lanir and Fung, 1974; Humphrey et al., 1990; Zamir and Taber, 2004a). An early method for investigating mechanical stress in a soft biological tissue (namely, skin) was introduced by Karl Langer in 1862 (Langer, 1978a,b). He excised small circular plugs of tissue from the skin of cadavers and assessed the shapes of the resulting wounds. If a wound opened and remained circular, a state of isotropic tension was revealed. If a wound became elliptical, a line of dominant (or anisotropic) tension was indicated, with its direction corresponding to the major axis of the ellipse.[7]

In the present work, stress distributions in epithelia are estimated from measured changes in hole geometry and computational modeling. In addition, our method offers valuable insight regarding the local constitutive properties of the material. As an experimental model we consider the case of the embryonic chick blastoderm, though our theoretical findings are not limited to this situation alone. During embryonic development, it is well established that mechanical forces give rise to the creation and subsequent evolution of biological form (a process known as morphogenesis), and recent work in our lab has suggested a mechano-regulatory role for the stresses that develop during epithelial morphogenesis (Taber, 2008).

[7]Interestingly, these experiments were the product of an early clinical investigation. A patient intent on suicide had presented with elliptically-shaped chest wounds. It was unclear, however, whether these lesions were the doings of a circular awl as the patient contended, or, due to their elliptical shape, a penknife blade. To settle the matter, surgical experiments on cadavers were performed (Langer, 1978a).

3.2 Methods

3.2.1 Theoretical framework

Rivlin and Thomas first studied the effects of a circular hole in a stretched, hyperelastic sheet (Rivlin and Thomas, 1951). They considered the behavior of an isotropic, incompressible circular membrane with a single circular hole under applied axisymmetric loads. Their work was later extended by accounting for the effects of non-axisymmetric loading (Oden and Key, 1972) and material anisotropy (David and Humphrey, 2004). Using the commercial finite element (FE) package COMSOL Multiphysics (v3.4; COMSOL AB), we analyze two related problems, each with particular relevance for our epithelial perforation experiments. The first involves the deformation of a membrane with two holes. Since our method uses hole geometry to estimate stress, this model offers insight into how the spacing between the holes can influence their geometry. The second problem considers the effects of anisotropic stretch. In particular we are interested in the relationship between hole geometry and the principal stretch ratios in the membrane.

Equibiaxially stretched membrane with two circular holes

Consider equibiaxial deformation of a thin, square, nearly incompressible sheet with two holes that are circular in the unloaded configuration (Fig. 3.1a). (For isotropic materials, perforating an equibiaxially pre-stretched membrane with circular holes is equivalent to stretching a membrane that already contains circular holes (David and Humphrey, 2004)). Displacements are prescribed along the boundaries of the sheet to impose the equibiaxial stretch ratio λ. In general epithelia are thin structures, so a state of plane stress is assumed. The deformation gradient tensor in the plane of the membrane is given by

$$\mathbf{F} = \begin{bmatrix} 1 + \frac{\partial u}{\partial X} & \frac{\partial u}{\partial Y} \\ \frac{\partial v}{\partial X} & 1 + \frac{\partial v}{\partial Y} \end{bmatrix}, \tag{3.1}$$

where u and v represent material point displacements in the X and Y directions, respectively. The constitutive response for an isotropic membrane is assumed to be

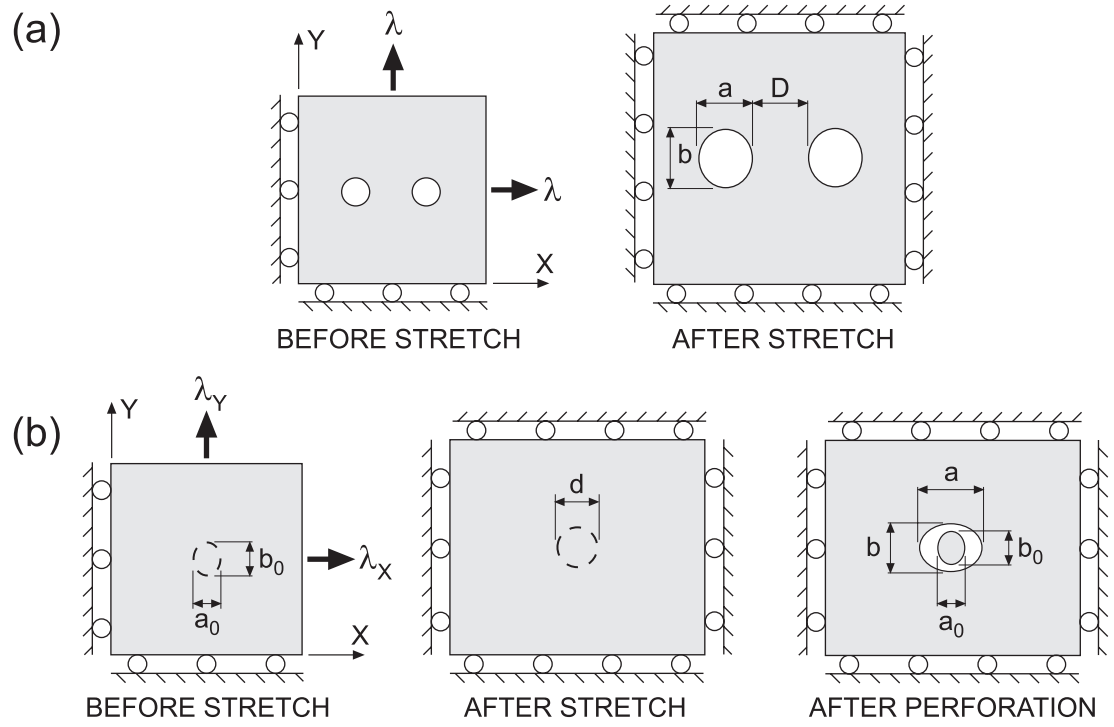

Figure 3.1: Model schematics for (a) an equibiaxially stretched membrane with two circular holes and (b) the circular perforation of a biaxially stretched membrane. Dashed lines indicate internal boundaries.

describable with the exponential strain-energy density function

$$W = \frac{C_1}{C_2}\left[e^{C_2(\bar{I}_C - 3)} - 1\right] + p\left(1 - J - \frac{p}{2\kappa}\right), \tag{3.2}$$

where C_1 is a material constant with units of stress, C_2 is a non-dimensional material constant, κ is the bulk modulus, $J = \det \mathbf{F}$, p is a penalty variable introduced for nearly incompressible materials, and $\bar{I}_C = J^{-2/3} \operatorname{tr} \mathbf{C}$ is the modified first invariant of the right Cauchy-Green deformation tensor, $\mathbf{C} = \mathbf{F}^T \cdot \mathbf{F}$. Material nonlinearity is varied by changing the magnitude of C_2; as $C_2 \to 0$, the material approaches a neo-Hookean response. To ensure near incompressibility we take $\kappa > 10^6 * C_1$. The Cauchy stress tensor is given by the relation

$$\boldsymbol{\sigma} = J^{-1}\mathbf{F}.\frac{\partial W}{\partial \mathbf{F}^T}. \tag{3.3}$$

In the deformed membrane, the axes of the elliptical holes are described by the lengths a and b, and D is the distance separating the two holes (Fig. 3.1a). The ratio D/a characterizes the hole spacing, and b/a is a measure hole circularity.

Circular perforation of a biaxially pre-stretched membrane

An equivalent intact membrane is subjected to an arbitrary biaxial stretch, characterized by the stretch ratios λ_X and λ_Y (Fig. 3.1b). Displacements are prescribed along the exterior boundaries of the membrane to impose the stretch. The constitutive response is again defined by Eq. (3.2). An internal elliptically-shaped boundary is specified within the undeformed membrane; the axes of this ellipse are given by a_0 and b_0. The lengths of the axes are chosen so that, when the biaxial stretch is imposed, the internal boundary deforms into a circle with diameter d. Thus,

$$a_0 = \frac{d}{\lambda_X}, \quad b_0 = \frac{d}{\lambda_Y}. \tag{3.4}$$

After the stretch, the solver is stopped, and the governing equations inside the region enclosed by the (now) circular boundary are inactivated. Boundary conditions along the circle are then changed from internal to traction-free. The solver is resumed, and the stress in the membrane causes the circular hole to deform into an ellipse defined

by the axes a and b. (The inactive region, now unloaded, would recover its initial geometry.)

3.2.2 Embryo preparation and perforation experiments

Fertilized White Leghorn chicken eggs were incubated in a humidified, forced draft incubator at 38°C for 24 to 26 hours to yield embryos at Hamburger and Hamilton (HH) stage 6 (Hamburger and Hamilton, 1951). At this point the entire embryo is organized as a flat layered sheet called the blastoderm. The procedure used to harvest whole embryos has been described previously . Briefly, an annular filter paper ring was placed over the embryo, and the surrounding membrane adhered to the paper. The paper ring was then dissected from the egg, keeping the membrane and embryo intact, thus preserving the stresses normally present in the tissue. The embryos were laid ventral side up, placed atop a 3% agar gel, and covered with a thin layer of PBS. A hollow, pulled glass micropipette, machined to an outer diameter of approximately 200 μm, was used to punch through the embryonic blastoderm at multiple locations. Via capillary suction and the downward force of the pipette, circular plugs of the tissue were excised (Fig. 3.2).

3.3 Results and Discussion

3.3.1 Effects of hole spacing

If hole geometry is used to estimate the stress in the membrane, we must make sure the holes are spaced far enough apart so they do not influence one another's shapes. To determine a sufficient spacing distance, we employed our equibiaxial stretching model (Section 3.2.1). Serial solutions to the model were generated by varying 1) the distance between the holes, 2) the equibiaxial stretch ratio λ, and 3) the material constant C_2. The ratios D/a and b/a were evaluated in the deformed configuration (i.e., after the imposed stretch), which enabled us to compare their magnitudes with those measured in experiments. Asymmetric stress concentrations develop near the holes, making them become non-circular. However, if the holes are to connote the

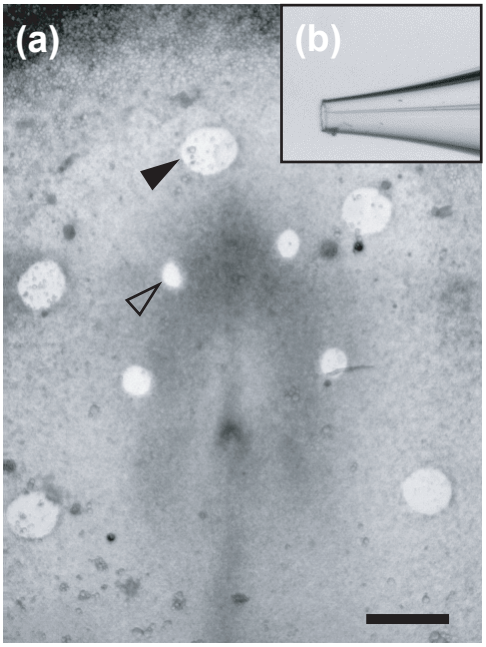

Figure 3.2: (a) Perforation experiment of HH stage 6 chick blastoderm. (b) Tip of machined micropipette used to create holes. Scale bar = 500 μm.

imposed isotropic stress field in the membrane at-large, they should remain nearly circular as the membrane deforms (i.e., b/a should be approximately equal to 1).

For two values of stretch, the circularity (b/a) is plotted as a function of hole spacing (D/a) for various C_2 (Fig. 3.3). As the distance between the holes increases, they become more circular. Moreover, for each value of λ and C_2, b/a is sufficiently close to 1 for $D/a \gtrsim 3$. So, independent of the membrane constitutive properties and applied in-plane stretch, this ratio ($D/a = 3$) can serve as a guide for determining the hole spacing in our perforation experiments.

3.3.2 Effects of anisotropic stretch

For an isotropic membrane, experimental holes of elliptical shape are taken to indicate regions of anisotropic stress or stretch in the membrane. Hole shape is characterized by the axes of the best-fit ellipse, and the lengths of these axes are used to estimate the principal stretch ratios. (Axis orientation is used to determine the principal directions.) This relationship, however, is somewhat unclear. Is axis length a function

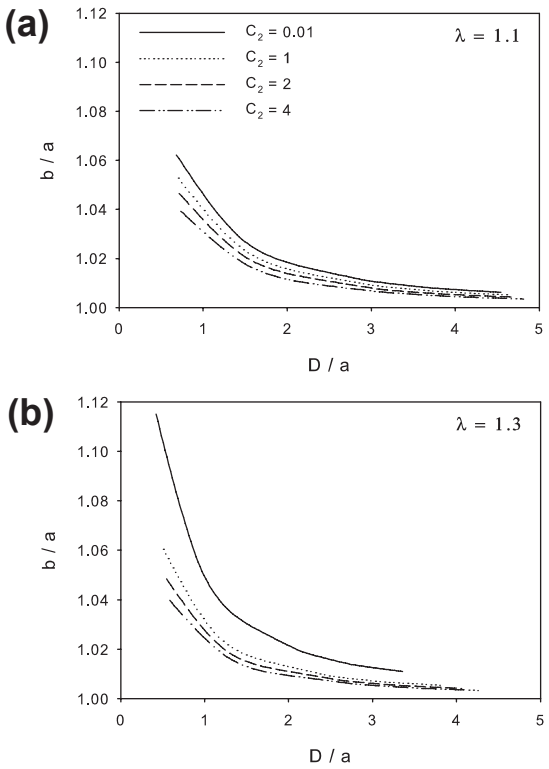

Figure 3.3: Effects of hole spacing (D/a) on hole circularity (b/a) for (a) $\lambda = 1.1$ and (b) $\lambda = 1.3$

of the stretch in the direction of the axis only? Or is it also influenced by the amount of transverse stretch?

So, using our circular perforation model (Section 3.2.1), we assign different stretches in the transverse Y-direction ($\lambda_Y = 1.0, 1.1, 1.2$) to a series of membranes with $C_2 = 0.01$ and $\lambda_X = 1.3$. In each case, a circular region of diameter d is removed from the stretched membrane, and the dimensions of the resultant holes (a and b) are used to determine the influence of transverse stretch on hole shape (Fig. 3.4). The results show that the value of a is nearly identical for each of the imposed transverse stretches. This suggests that, for $C_2 = 0.01$, the axis length a is approximately independent of the transverse stretch λ_Y (i.e., $a = a(\lambda_X, \lambda_Y) \approx a(\lambda_X)$). As material nonlinearity increases, however, hole geometry becomes more dependent on transverse stretch. For the values of C_2 considered in this paper, however, our approximation still holds. Thus, if we assume material isotropy and uniformity, a comparison between

individual axis lengths should be sufficient to estimate relative differences in stretch. The magnitude of the perpendicular axis length need not be taken into account.

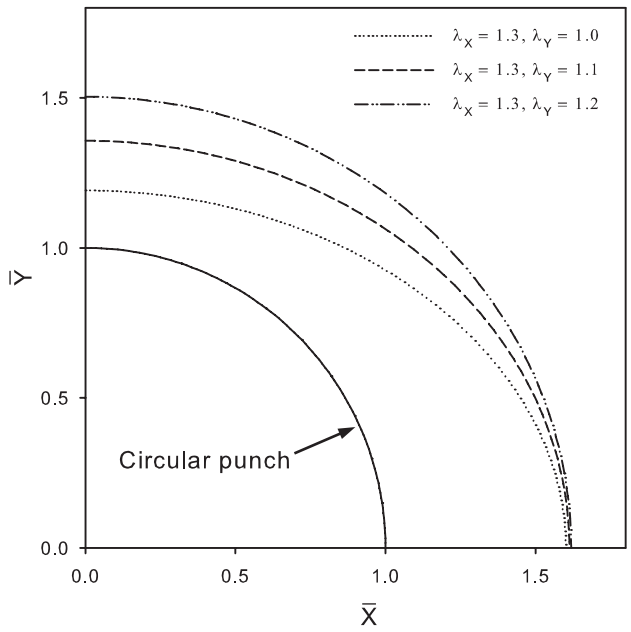

Figure 3.4: Effects of transverse stretch (λ_Y) on hole shape for fixed λ_X, where $\bar{X} = 2X/d$ and $\bar{Y} = 2Y/d$.

Now, since $a \approx a\,(\lambda_X)$, we can examine the effects of material nonlinearity on this relationship. The value of λ_Y is arbitrary, so it is held constant at 1. We subject a series of membranes to different pure uniaxial stretches in the X-direction. A circular region of diameter d is (here again) deactivated in the deformed configuration. The normalized (far-field) stress in the membrane (σ_{XX}/C_1) is plotted as function of the stretch ratio λ_X (Fig. 3.5a). The stress is relatively independent of C_2 for $0.9 < \lambda_X < 1.1$ (i.e., in the linear regime); however, for $\lambda_X > 1.1$, the stress increases dramatically with C_2. The elliptical axis (a), as normalized by the diameter of the circular punch (d), is also plotted against the stretch ratio λ_X (Fig. 3.5b). It bears a similar domain dependence on C_2, but as the material becomes more nonlinear, a/d decreases and the hole opens to a lesser extent. The same holds true for b/d as a function of λ_Y (Fig. 3.5c).

The dependence of hole geometry on C_2 can be used to gather information about the local constitutive properties of the material. If the circular plug of tissue excised during the experiments (Fig. 3.5d) is recoverable, a, a_0, b, b_0, and d are all measurable

quantities. The principal stretch ratios λ_X and λ_Y can be determined from Eqs. (3.4). For a single hole, plotting experimental a/d vs. λ_X produces a single point on Fig. 3.5b, a point which can then be compared to the family of curves of varying C_2. For $\lambda_X > 1.1$, C_2 can be estimated by finding the curve which passes through the lone plotted point. This value of C_2 then is based on experimental deformation in the X-direction. If $\lambda_X < 1.1$, however, the point would be expected to lie along the linear regime of the curves, where C_2 is not unique and therefore unidentifiable. An estimation of C_2 based on deformation in the Y-direction is similarly found using Fig. 3.5c and an experimental b/d vs. λ_Y point. If the material is isotropic, the two estimations for C_2 should be identical. If they differ, our assumed W is invalid, and a local material anisotropy is indicated in the material.

This method unfortunately does not offer a direct way of measuring C_1. Thus, to obtain a complete description of W for a material, C_1 must be determined experimentally by some other means, such as microindentation testing (Zamir and Taber, 2004a). If, however, the principal stretch ratios, C_1, and C_2 are all known, and material isotropy has been established, then the quantitative stresses in the membrane can be calculated using Eq. (6.20). For unknown C_1, only $\boldsymbol{\sigma}/C_1$ is available. If Eq. (3.2) is shown to be invalid, an alternative form of W must be used.

3.3.3 Illustrative Example

The perforation experiments show that the distribution of stress varies dramatically across the HH stage 6 blastoderm (Fig. 3.2a); the same pipette punch (see Fig. 3.2b) was used to create each wound in the membrane. Though we recognize that the blastoderm is not structured as a simple monolayered epithelium and that, in general, each of the germ layers may possess different mechanical properties, our perforation experiments still offer a description of tissue stress, albeit averaged across the thickness of the blastoderm.

A comparison of the (inner) pipette diameter with each hole's dimensions readily indicates areas of biaxial tension (closed arrowhead) and compression (open arrowhead). Capillary suction in the pipette often made recovery of the excised tissue plugs difficult. At times, however, the plug was left behind and could be used to estimate the

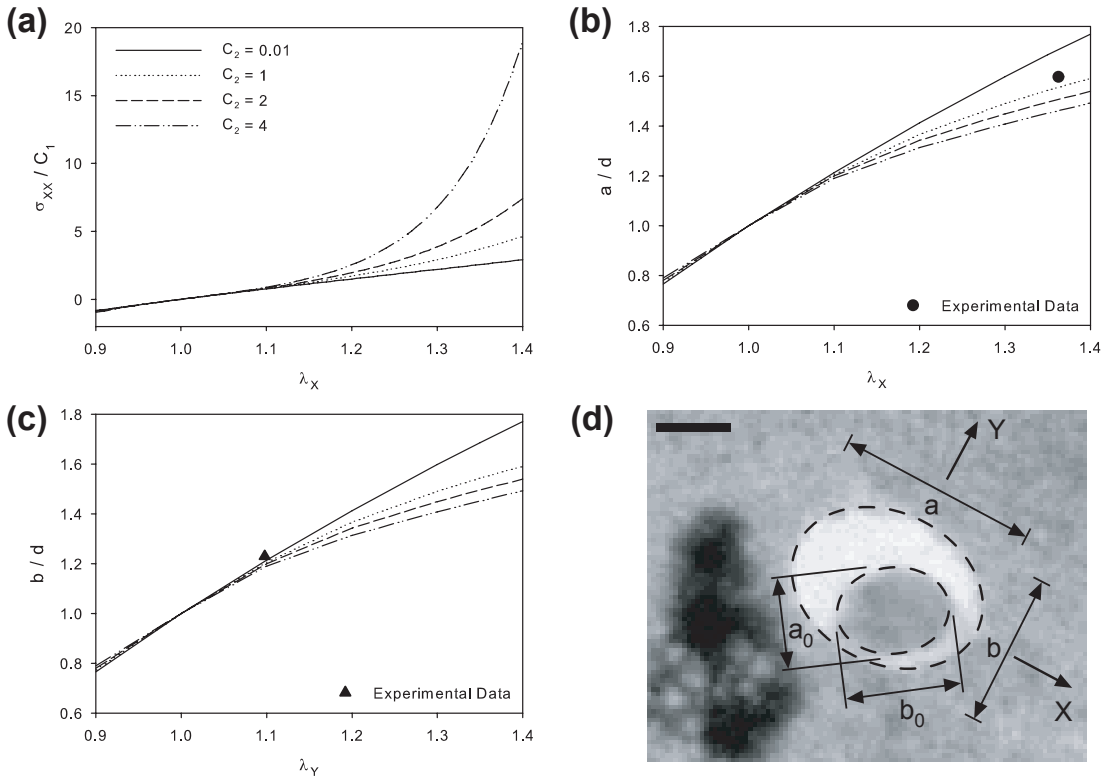

Figure 3.5: Estimation of constitutive properties. (a) Effects of C_2 on far-field normal stress for pure uniaxial stretch in X-direction. (b,c) Dependence of hole shape on λ_X and λ_Y, respectively, for varying C_2. (d) Perforation experiment of early chick blastoderm (different embryo from Fig. 3.2). The excised tissue is circumscribed by an ellipse with axes a_0 and b_0. Scale bar = 100 μm.

material properties of the blastoderm (see Fig. 3.5d, in a different embryo). Here, the axes a_0 and b_0 were measured at 122 and 151 μm, respectively. The inner diameter of the pipette (166 μm) was taken as d, and a and b had lengths of 265 and 204 μm, respectively. These lengths are used to calculate $a/d = 1.60$, $b/d = 1.23$, $\lambda_X = 1.36$ and $\lambda_Y = 1.10$, which are plotted on Figs. 3.5b&c. An estimation for C_2 is indeterminate from Fig. 3.5c, as the experimental data point lies along the linear portion of the curves. (The fact that the point is almost exactly superimposed on the curves, however, helps validate our theoretical results.) On Fig. 3.5b, our experimental point indicates a C_2 value of approximately 0.5 (as confirmed by computational model, not shown). Unfortunately, here material (an)isotropy could not be determined since a second estimation for C_2 was unavailable.

3.4 Conclusions

Our perforation technique uses experiments and computational modeling to estimate the stress distribution and local constitutive properties in an epithelium. The principal stretch ratios in the tissue are determined via measured changes in hole geometry. Though our theoretical results are limited to isotropic, incompressible materials, this method can be used to verify material isotropy (even in cases of anisotropic stretch) and provide a quantitative estimate of the stress field in the membrane.

Chapter 4

Mechanics of head fold formation: investigating tissue-level forces during early development

Summary

During its earliest stages, the avian embryo is approximately planar. Through a complex series of folds, this flat geometry is transformed into the intricate three-dimensional structure of the developing organism. Formation of the head fold (HF) is the first step in this cascading sequence of out-of-plane tissue folds. The HF establishes the anterior extent of the embryo and initiates heart, foregut, and brain development. In this paper, we use a combination of computational modeling and experiments to determine the physical forces that drive HF formation. Using chick embryos cultured ex ovo, we measured the following: (1) changes in tissue morphology in living embryos using optical coherence tomography (OCT), (2) morphogenetic strains (deformations) through the tracking of tissue labels; and (3) regional tissue stress estimates using changes in the geometry of circular wounds punched through the blastoderm. To determine the physical mechanisms that generate the HF, we created a three-dimensional computational model of the early embryo, consisting of pseudoelastic plates representing the blastoderm and vitelline membrane. Based on previous experimental findings, we simulated the following morphogenetic mechanisms: (1) convergent extension in the neural plate (NP); (2) cell wedging along the anterior NP border; and (3) autonomous in-plane deformations outside the NP. Our

numerical predictions agree relatively well with the observed morphology, as well as our measured stress and strain distributions. The model also predicts the abnormal tissue geometries produced when development is mechanically perturbed. Taken together, the results suggest that the proposed morphogenetic mechanisms provide the main tissue-level forces that drive HF formation.

4.1 Introduction

The early metazoan embryo is constructed primarily out of thin epithelia (Davies, 2005). During morphogenesis, these 2D epithelial sheets are shaped (through a series of folds and in-plane deformations) into the complex 3D structures that make up the embryonic body plan. Physical forces play an indispensable role in this process, and recent work has shown that mechanical loads can influence gene expression patterns during development (Farge, 2003; Desprat et al., 2008; Wozniak and Chen, 2009). Still, while much work has been done to identify precursor cell populations and follow their differentiation into specific tissues, relatively few investigators have quantified the tissue deformations involved in early embryogenesis or identified the mechanical forces that drive them (Hutson et al., 2003; Zamir et al., 2006; Rauzi et al., 2008; Blanchard et al., 2009).

Here we address the mechanics of head fold (HF) formation in the early chick embryo (Fig. 4.1). This crescent-shaped fold, conserved across amniotes and mammals, forms at the anterior end of the neural plate (NP) and constitutes the first bounding body fold. It initiates both foregut and heart development (Bellairs, 1953; Stalsberg and DeHaan, 1969; Schoenwolf and Smith, 2000) and is the first major 3D structure to form in the chick embryo. The biophysical mechanisms that drive HF formation remain poorly understood.

In this paper, we combine computational modeling with data culled from experiments on chick embryos to investigate the mechanical forces that shape the HF. Mathematical models offer particular insight here, allowing us to test whether a given set of forces could plausibly generate the tissue deformations observed during morphogenesis. Our results indicate that a combination of the following morphogenetic processes likely drive HF formation: (1) convergent extension within the NP, (2) coordinated,

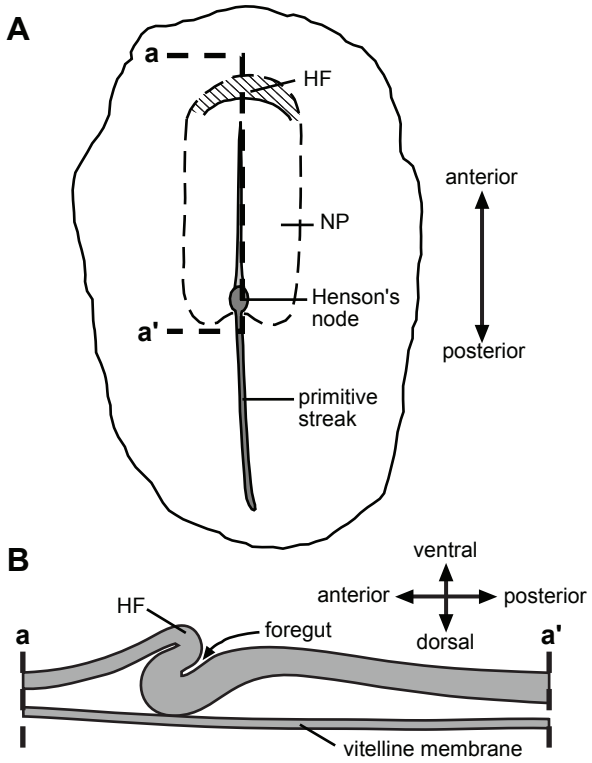

Figure 4.1: **The head fold (HF) is the first major 3D structure to form in the chick embryo. (A)** Ventral schematic view of HH stage 7 embryo. The crescent-shaped HF forms at the anterior end of the neural plate (NP). Prior to HF formation, the chick blastoderm is approximately planar. **(B)** Sagittal view of midline section a-a'. The blastoderm is in local contact with the vitelline membrane and doubled over into an "S"-shaped configuration.

active cell wedging at the anterior NP border, and (3) epidermal shaping outside the NP. Our approach can be readily generalized to other morphogenetic processes and offers insight into how forces are organized at the tissue level to create biological form.

4.2 Materials and methods

4.2.1 Experimental methods

Embryo preparation and culture

Fertilized White Leghorn chicken eggs were incubated in a humidified, forced draft incubator at 38°C for 23 to 29 hours to yield embryos between Hamburger and Hamilton (HH) stages 5 and 7 (Hamburger and Hamilton, 1951). Whole embryos were harvested using the filter paper carrier method described in Voronov and Taber (2002). The embryo and underlying vitelline membrane (VM) were kept intact, thereby preserving the stresses normally present in the tissue. To remove the effects of surface tension, each embryo was completely submerged under a thin layer of liquid culture media and incubated at 38°C in 95% O_2 and 5% CO_2 (Voronov and Taber, 2002).

Manipulation of embryos

Endoderm and mesoderm were removed from a group of HH stage 5 embryos (n=6) to determine if the forces behind HF formation are ectodermal in origin. Small amounts ($\sim$1 nL) of 3-5% collagenase in PBS were injected between the ectoderm and endo/mesoderm using pulled glass micropipettes and a pneumatic pump (PicoPump PV830, World Precision Instruments). Embryos were incubated at 38°C for 30 minutes, and the endo/mesoderm were removed using glass needles.

To perturb normal development, the VM was removed or the blastoderm was cut to relieve tissue stresses. Each microsurgery was performed under a dissecting microscope using needles fashioned from pulled glass micropipettes.

Optical coherence tomography (OCT)

OCT was used to obtain 3D images of living embryos; its depth of field ($\sim$2 mm) and spatial resolution ($\sim$10 μm) are well-suited for this purpose (Huang et al., 1991; Fujimoto, 2003). Cross-sectional image stacks were reconstructed into 3D volumes and optically sectioned using Volocity (Improvision, Waltham, MA). Time-lapse experiments were conducted with the custom-built OCT system described previously (Filas et al., 2007, 2008).

Tissue stress estimates

Machined glass micropipettes were used to excise circular plugs of tissue from HH stage 4 (n=3) and stage 6 (n=9) embryos. Bright field images of each wounded embryo were captured with a dissecting microscope (Leica MZ8) and attached video camera. Approximately 30–45 seconds elapsed between wounding and image capture.

To rule out the possibility that our results were affected by a healing response, as has been reported in embryos at nearly equivalent developmental stages (Clark et al., 2009; Joshi et al., 2010), we stained F-actin using rhodamine phalloidin (Molecular Probes). After wounding, embryos were incubated at room temperature for varying periods of time and fixed in 4% paraformaldehyde. Each embryo was then incubated overnight at 4°C in a solution containing rhodamine phalloidin (Molecular Probes) diluted 1:40 in phosphate buffered saline (PBS) with 0.1% Triton X-100 (Sigma) and 1% bovine serum albumin (BSA) (Sigma). A stack of fluorescent images for each stained circular wound was generated using a Leica DMLB microscope with a computerized z-motor (Improvision) and the software package Openlab 5.5.0 (Improvision). Image stacks were then deconvolved using the Volume Deconvolution routine in Openlab. These experiments confirmed that after 30–45 seconds an intact contractile ring had not yet assembled around the wounds (Fig. 4.2).

As described in Chapter 3, wound geometry was used to characterize regional tissue stress (force per unit area). For each wound, the Analyze Particles routine in ImageJ (NIH) was used to determine the area, major axis (a), and minor axis (b) of the best-fit ellipse. A state of tension (or compression) was indicated if the wound area

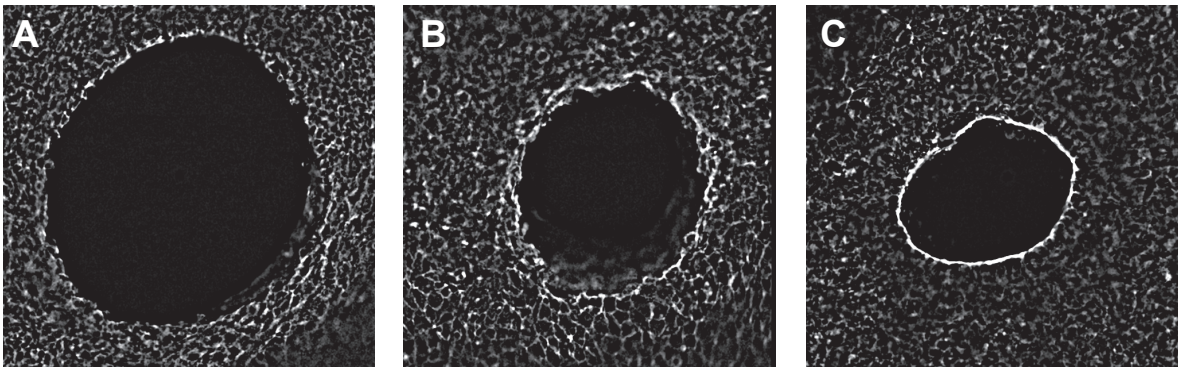

Figure 4.2: F-actin distributions around punched circular wounds in the chick blastoderm after (A) 45 sec, (B) 5 min, (C) 1 hr.

was greater (or smaller) than that of the punch (with diameter d). If the wound remained circular (that is, if the anisotropy index $b/a \to 1$), a state of isotropic stress was identified; elliptical wounds, alternatively, indicated anisotropic stress.

Tissue labeling and tracking

Tissue deformations were quantified by tracking the motion of material point markers. Ectodermal cells were labeled using the lipophilic fluorescent dyes DiI and DiO (Molecular Probes, Eugene, OR) which incorporate into the cell membrane. Embryos at HH stage 5 (n=6) were placed dorsal side up in 35 mm culture dishes and covered with PBS. Glass needles were used to remove the VM and thereby expose the ectoderm. Iron particles, soaked in saturated DiI (or DiO) at room temperature, were then sprinkled across the embryo. After 10 minutes of 38°C incubation, a strong magnet was used to remove the particles, leaving fluorescently labeled cells behind. Using this technique, hundreds of cells could be easily (and simultaneously) labeled.

We repeated this protocol on another embryo using CellTracker CM-DiI (Molecular Probes) to ensure that only cells in the ectoderm were being labeled (Fig. 4.3A). This fluorescent marker persists after processing for paraffin sections, so the embryo was fixed in 4% paraformaldehyde, embedded in paraffin, and sliced into 10 μm parasagittal sections.

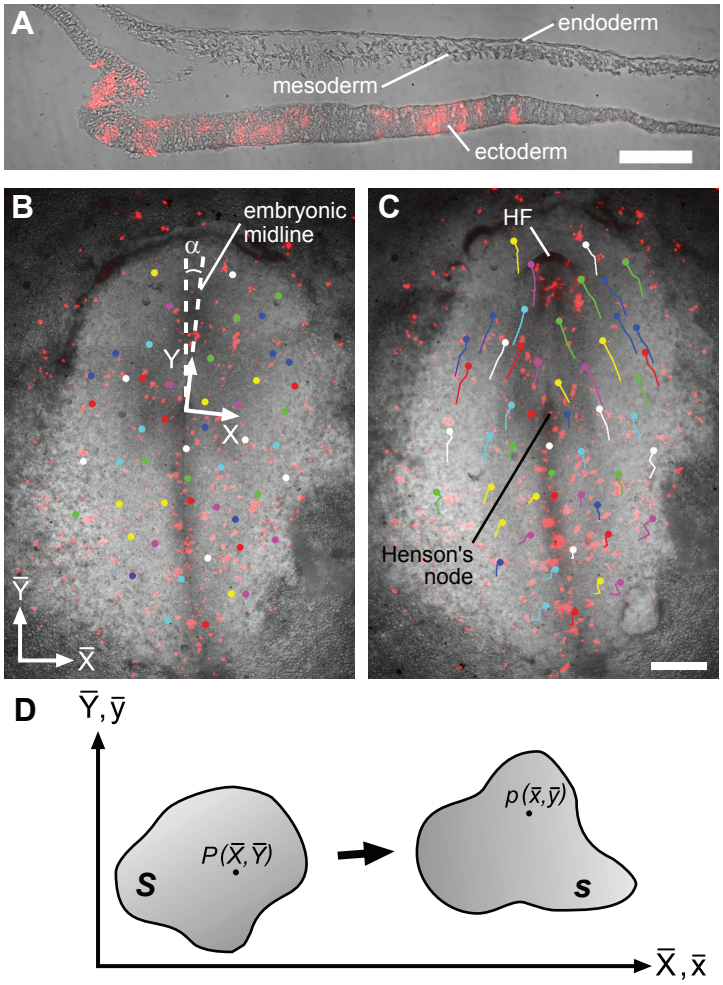

Figure 4.3: **Tissue deformation during head fold (HF) morphogenesis is quantified using tracked tissue labels. (A)** 10 μm parasagittal section of HH stage 6 embryo. The ectoderm was labeled with fluorescent dye at HH stage 5, cultured ex ovo until the HF had formed, and then fixed for paraffin sectioning. The fluorescent label was not present in any endodermal or mesodermal cells, confirming that any cells labeled using this technique reside in the ectoderm. Scale bar = 100 μm. **(B,C)** Fluorescently labeled embryo at HH stage 5 (B) and stage 6 (C). The motion of labeled cells was tracked in image coordinates $\left(\bar{X}, \bar{Y}\right)$. Representative label tracks are shown. An embryo coordinate system (X, Y), oriented transverse (X) and parallel (Y) to the embryonic midline and centered at Henson's node, was used to compute Lagrangian strains (α = angle between $\bar{Y}$ and Y axes). Scale bar = 500 μm. **(D)** Deformation of a 2D surface. The point $P\left(\bar{X}, \bar{Y}\right)$ on surface S deforms into the point $p\left(\bar{x}, \bar{y}\right)$ on surface s.

Initial bright field and fluorescent images of whole embryos were captured using a Leica DMLB microscope and attached video camera (Retiga 1300). Embryos were then cultured until the HF had formed at HH stage 6, approximately 2–4 hours later. Subsequent time-lapse images were captured at approximately 30–45 minute intervals. The motion of labeled cells was tracked using the Manual Tracking plugin in ImageJ (Fig. 4.3B,C), and the positions of selected labels were recorded in image coordinates $\left(\bar{X}, \bar{Y}\right)$ at each timepoint, where the origin of the $\bar{X}, \bar{Y}$-system is the lower left corner of the camera frame and $\bar{X}$ and $\bar{Y}$ are the horizontal and vertical coordinate axes, respectively.

Strain analysis

Tissue marker coordinates were used to calculate morphogenetic strains. Briefly, consider a planar surface S that deforms into the planar surface s (Fig. 4.3D), where the point $P\left(\bar{X}, \bar{Y}\right)$ on S moves to the location $p\left(\bar{x}, \bar{y}\right)$ on s. There is a one-to-one mapping between each point on S and s, giving $\bar{x} = \bar{x}\left(\bar{X}, \bar{Y}\right)$ and $\bar{y} = \bar{y}\left(\bar{X}, \bar{Y}\right)$. Lagrangian strains characterize the deformation from S to s and are referred to basis vectors in the reference configuration (i.e., S). In image coordinates $\left(\bar{X}, \bar{Y}\right)$, they are defined as

$$
\begin{aligned}
E_{\bar{X}\bar{X}} &= \frac{1}{2}\left[\left(\frac{\partial \bar{x}}{\partial \bar{X}}\right)^2 + \left(\frac{\partial \bar{y}}{\partial \bar{X}}\right)^2 - 1\right] \\
E_{\bar{Y}\bar{Y}} &= \frac{1}{2}\left[\left(\frac{\partial \bar{x}}{\partial \bar{Y}}\right)^2 + \left(\frac{\partial \bar{y}}{\partial \bar{Y}}\right)^2 - 1\right] \\
E_{\bar{X}\bar{Y}} &= \frac{1}{2}\left[\frac{\partial \bar{x}}{\partial \bar{X}}\frac{\partial \bar{x}}{\partial \bar{Y}} + \frac{\partial \bar{y}}{\partial \bar{X}}\frac{\partial \bar{y}}{\partial \bar{Y}}\right]
\end{aligned}
\tag{4.1}
$$

The first image in each time-lapse stack (corresponding to HH stage 5) was taken as the reference configuration. As described by Filas et al. (2007), the MATLAB routine *gridfit* was used to fit 2D surfaces through the set of marker coordinates to generate $\bar{x}\left(\bar{X}, \bar{Y}\right)$ and $\bar{y}\left(\bar{X}, \bar{Y}\right)$, which give the strain components in image coordinates by equation (4.1). The following equations (Taber, 2004) were then used to transform these strains into components relative to an embryo coordinate system (X, Y) (Fig. 4.3B), which is oriented transverse (X) and parallel (Y) to the embryonic

midline:

$$\begin{aligned} E_{XX} &= E_{\bar{X}\bar{X}} \cos^2\alpha + E_{\bar{Y}\bar{Y}} \sin^2\alpha + 2E_{\bar{X}\bar{Y}} \cos\alpha \sin\alpha \\ E_{YY} &= E_{\bar{X}\bar{X}} \sin^2\alpha + E_{\bar{Y}\bar{Y}} \cos^2\alpha - 2E_{\bar{X}\bar{Y}} \cos\alpha \sin\alpha \\ E_{XY} &= E_{\bar{X}\bar{Y}} \left(\cos^2\alpha - \sin^2\alpha\right) + (E_{\bar{Y}\bar{Y}} - E_{\bar{X}\bar{X}}) \cos\alpha \sin\alpha \end{aligned} \tag{4.2}$$

where α indicates the angle between the embryonic midline and the $\bar{Y}$ axis.

Statistics

To analyze our wound geometry data, a two-level nested ANOVA with the Tukey post-hoc test was implemented in a spreadsheet (Sokal and Rohlf, 1981; Zar, 2010). Circular statistics were used to characterize wound orientation (Zar, 2010).

4.2.2 Computational Methods

Finite element model

To study the mechanical forces that drive HF formation, we constructed a nonlinear, 3D finite element (FE) model using COMSOL Multiphysics (Version 3.4, COMSOL AB, Providence, RI). As shown later, contact between the embryonic blastoderm and VM is an important factor. Hence, the model geometry consists of the blastoderm and VM separated by a narrow interstitial space (Fig. 4.4), and a plane of symmetry is specified along the midline. Frictionless contact between the blastoderm and VM is assumed, with an augmented Lagrangian approach used to solve for the contact pressure. Consistent with our OCT images of HF-stage embryos (see below), the NP is twice as thick as the surrounding epithelium.

To model the mechanics of morphogenesis, we use the theory of Rodriguez et al. (1994) to simulate finite volumetric growth. The main idea is that the total deformation of a psuedoelastic body, described by the deformation gradient tensor $\mathbf{F}$, can be decomposed into a growth tensor $\mathbf{G}$ and an elastic deformation gradient tensor $\mathbf{F}^*$ via the relation $\mathbf{F} = \mathbf{F}^* \cdot \mathbf{G}$. During growth, $\mathbf{G}$ changes the zero-stress configuration of each material element, while $\mathbf{F}^*$ generates stress and enforces geometric compatibility between elements. This theory has been used to model a number of morphogenetic

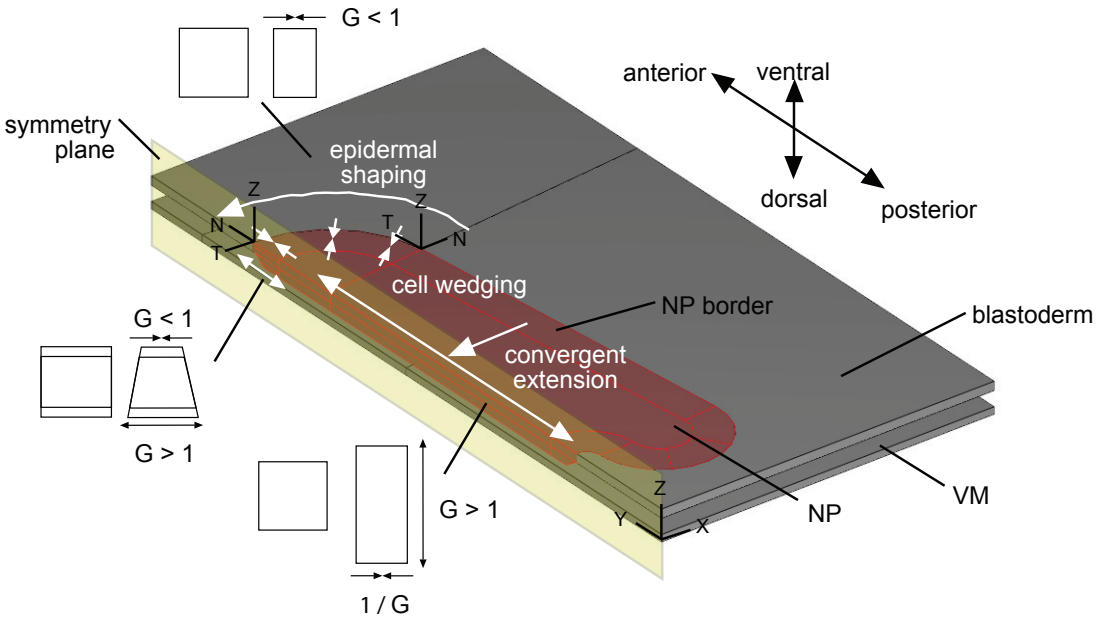

Figure 4.4: **Computational model of head fold formation.** The model geometry consists of the blastoderm and vitelline membrane (VM) separated by a narrow interstitial space. A plane of symmetry is specified along the embryonic midline, and frictionless mechanical contact between the blastoderm and VM is assumed. The growth tensor **G** drives morphogenesis in the model. Cell wedging along the anterior border of the neural plate (NP), convergent extension of the NP, and epidermal shaping outside the NP were simulated by specifying the growth components $G_i(t)$ in each active region (schematics and white arrows). See text for details.

processes (Taber, 2001, 2008). An introductory treatment can found in section 3 of Taber (1995).

To model anisotropic growth, two coordinate systems are defined (Fig. 4.4). The first is the global embryo coordinate system (X, Y, Z), where the X and Y axes coincide with the transverse and longitudinal embryonic axes, respectively. The second is a local curvilinear coordinate system (N, T, Z), defined such that the N and T axes are oriented normal and tangent, respectively, to the NP border (and thus to the prospective HF). We assume that growth occurs along orthogonal directions defined by the unit vectors $\mathbf{e}_1$, $\mathbf{e}_2$, and $\mathbf{e}_3$, which are rooted in the reference configuration with $(1, 2, 3) = (X, Y, Z)$ or (N, T, Z). The growth tensor thus has the form $\mathbf{G} = G_1\mathbf{e}_1\mathbf{e}_1 + G_2\mathbf{e}_2\mathbf{e}_2 + G_3\mathbf{e}_3\mathbf{e}_3$, where the G_i are growth stretch ratios. As discussed below, the components of $\mathbf{G}$ are specified functions of time in each active region of the model.

Mechanical properties

Tissue stress depends on the elastic deformation $\mathbf{F}^*$ through the material constitutive relations. As a first approximation, embryonic tissues can be treated as pseudoelastic materials (Zamir et al., 2003; Zamir and Taber, 2004b,a) with viscoelastic material effects (e.g., stress relaxation) ignored. The blastoderm and VM are thus modeled as isotropic sheets of nearly incompressible material, characterized by the modified neo-Hookean strain-energy density function

$$W = \frac{\mu}{2}\left(\bar{I}^* - 3\right) + p\left(1 - J^* - \frac{p}{2\kappa}\right), \tag{4.3}$$

where μ is the small-strain shear modulus, κ is the bulk modulus, $J^* = \det \mathbf{F}^*$ is the elastic dilatation ratio, p is a penalty variable introduced for nearly incompressible materials, and $\bar{I}^* = J^{*-2/3}\,\mathrm{tr}\left(\mathbf{F}^{*T}\cdot\mathbf{F}^*\right)$ is a modified strain invariant. In terms of W, the Cauchy stress tensor is given by (Taber, 2004)

$$\boldsymbol{\sigma} = J^{*-1}\mathbf{F}^*\cdot\frac{\partial W}{\partial \mathbf{F}^{*T}}. \tag{4.4}$$

Microindentation tests in our laboratory have suggested that the bending rigidity (stiffness) of the NP (D_{NP}) is approximately twice that of the surrounding epithelium (D_S). For a concentrated load on a simply supported circular plate, the linear solution gives the bending rigidity $D \sim Eh^3$, where E is the elastic modulus and h is the plate thickness (Timoshenko and Woinowsky-Krieger, 1959). Inputting thickness values for the NP and surrounding epithelium based on our OCT images, this solution yields $E_S \approx 2E_{NP}$, which gives $\mu_S \approx 2\mu_{NP}$ since μ is linearly related to E. Other microindentation experiments have shown the VM to be approximately 3 times stiffer than the NP, which (following a similar process) gives $\mu_{VM} \approx 100\mu_{NP}$.

Simulation of morphogenetic processes

The growth tensor $\mathbf{G}$ drives morphogenesis in our model. The growth components $G_i(t)$ for each active region were selected by manual iteration. Parameter values were rejected if the model did not qualitatively match the observed HF morphology, as well as the measured stress and strain distributions in normal embryos. The selected $G_i(t)$ were further tested using data from mechanically perturbed embryos. Our proposed mechanism for HF formation consists of three main morphogenetic processes (Fig. 4.4):

- **Active cell wedging:** Actively generated, wedge-shaped cells have often been implicated in epithelial invaginations (Ettensohn, 1985; Haigo et al., 2003). In the chick embryo, Lawson et al. (2001) have reported cell wedging along the NP border, a phenomenon that appears intrinsic to the NP border zone and thus independent of any external loads (Moury and Schoenwolf, 1995). We model this wedging along the anterior NP border by specifying $G_N < 1$ along the ventral side of the blastoderm and $G_N > 1$ along the dorsal side, where N is the direction normal to the border (Fig. 4.4). This changes a cuboidal element into a wedge-shaped element. Cytoskeletal contraction has been linked to cell wedging (Lee and Nagele, 1985; Gorfinkiel et al., 2009; Martin et al., 2009), and moreover, microindentation data from our laboratory suggests the HF stiffens as it forms. A concomitant material stiffening thus accompanies our simulated wedging (i.e., μ_{NP} increases by a factor of 5).

- **Convergent extension:** During neurulation the NP elongates longitudinally and shortens transversely, a process known as convergent extension (Smith and Schoenwolf, 1997; Colas and Schoenwolf, 2001; Ezin et al., 2009). This behavior appears intrinsic to the NP itself and has been attributed to both cell intercalation (Schoenwolf and Alvarez, 1989; Ezin et al., 2009) and coordinated cell division (Sausedo et al., 1997). The mitotic cycle of neuroepithelial cells at this stage of development is approximately 8–12 hours in length (Schoenwolf, 1994). Since HF formation occurs over a shorter time period (typically, 2–4 hours), we assume cell intercalation is the dominant process and model convergent extension by specifying $G_X < 1$ and $G_Y = 1/G_X$ in the NP (Fig. 4.4). No change in material properties accompanies this growth, and the components of $\mathbf{G}$ specify an isochoric deformation (i.e., no volume change), since we are concerned solely with cell rearrangement.

- **Epidermal shaping:** The epidermal (or non-neuroepithelial) ectoderm undergoes autonomous changes in shape during neurulation (Moury and Schoenwolf, 1995). In particular the epidermis anterior to the NP (and thus, the prospective HF) narrows transversely. We model this epidermal shaping by specifying $G_T < 1$ along the blastoderm anterior to the NP, where T indicates the direction tangent to the NP border (Fig. 4.4).

Finally, our hole-punching experiments (see below) have shown that the blastoderm is in a state of equibiaxial tension before the HF forms. We therefore apply initial equibiaxial tensile stresses along the peripheral boundary of the blastoderm. The magnitude of this tension is based on experimental estimates of the amount of stretch in the tissue.

4.3 Results

4.3.1 Head fold geometry is distinctly three-dimensional

During the first day of development, the chick blastoderm is organized as a flat, laminar disk (Patten, 1971). It is composed of three separate germ layers (endoderm,

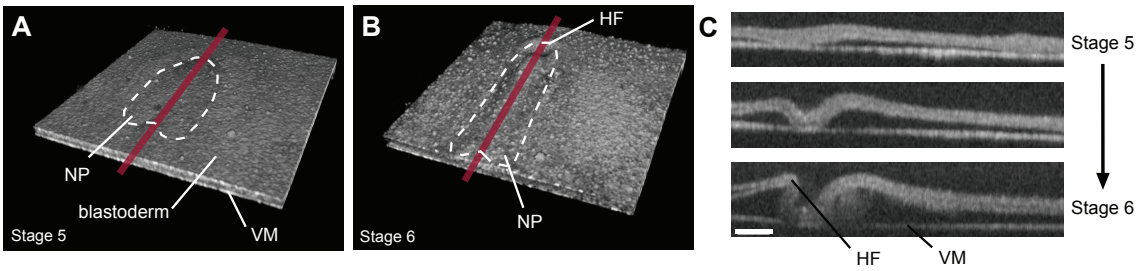

Figure 4.5: **OCT reveals 3D head fold (HF) geometry in living embryos. (A,B)** 3D OCT reconstructions of developing chick embryo at HH stage 5 (A) and stage 6 (B). The imaging window is 2 mm square (VM = vitelline membrane; NP = neural plate). **(C)** Optical midline sections (red lines in (A) and (B)) show the blastoderm doubling over on itself and contacting the VM as the HF forms. Scale bar = 200 μm.

mesoderm, and ectoderm) and underlies the vitelline membrane (VM). During these early stages, there are few visible landmarks to distinguish the embryonic body from the surrounding extra-embryonic tissues (Lillie, 1952). At 24 hours of incubation, however, a conspicuous crescent-shaped fold (the HF) forms at the anterior end of the thickened neural plate, where the blastoderm transitions to a thinner epithelium (Fig. 4.1).

Using our time-lapse OCT system, we generated three-dimensional images of the developing HF in living embryos (Fig. 4.5A,B). Optical sections along the embryonic midline show that, as the HF forms, the blastoderm bends locally at the NP border, contacts the VM, and doubles over onto itself (Fig. 4.5C). The tissue is tucked into an "S"-shaped configuration, with the HF lifted above the plane of the surrounding blastoderm.

4.3.2 Isolated ectoderm creates a head fold

Our proposed mechanism for HF morphogenesis involves active forces generated in the ectoderm. To establish whether ectoderm alone can produce a HF, we cultured isolated ectoderm from HH stage 5 (pre-HF) embryos (Fig. 4.6). Within 2 hours, these explants developed a HF (Fig. 4.6C), suggesting that the forces which create this structure have an ectodermal origin.

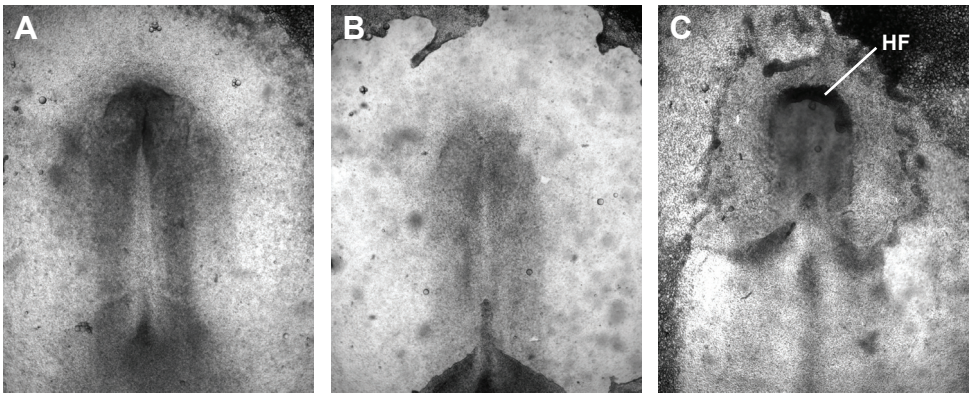

Figure 4.6: **Forces that create the head fold (HF) are ectodermal in origin.** The ectoderm was isolated in a group of HH stage 5 embryos (n=6). **(A)** Representative embryo before treatment, **(B)** immediately after dissection of endoderm and mesoderm, and **(C)** after 2 hours incubation. Isolated ectodermal explants still developed a HF.

4.3.3 Tissue deformation is inhomogeneous and anisotropic

We used ectodermal cell displacements to characterize the kinematic behavior of the blastoderm during HF formation. Fluorescent labels were tracked in the manner of dynamic fate mapping studies (Redkar et al., 2001; Cui et al., 2009; Ezin et al., 2009). Here, however, the goal was to quantify the global deformation of the tissue, rather than determine the eventual fate of individual cells.

Tracking the motion of tissue labels, we computed 2D Lagrangian strain distributions during HF formation (Fig. 4.7). During this process, most of the blastoderm remains relatively flat, so 2D Lagrangian strains can be used to capture the salient kinematic behavior outside the immediate HF region. The strain components E_{XX} and E_{YY} characterize relative length changes of line elements originally oriented parallel to the X and Y axes, respectively; E_{XY} is a measure of angle changes between line elements.

Strain distributions (measured for HH stage 6 relative to stage 5) were inhomogeneous and anisotropic, but remained relatively symmetric about the embryonic midline (Fig. 4.7). Negative transverse strains were present near the HF, and the shear distribution was primarily organized as a pair of bilateral peaks that spanned across the lateral NP border. Meanwhile, the NP elongated longitudinally ($E_{YY} > 0$) and shortened transversely ($E_{XX} < 0$). At intermediate timepoints, the overall strain

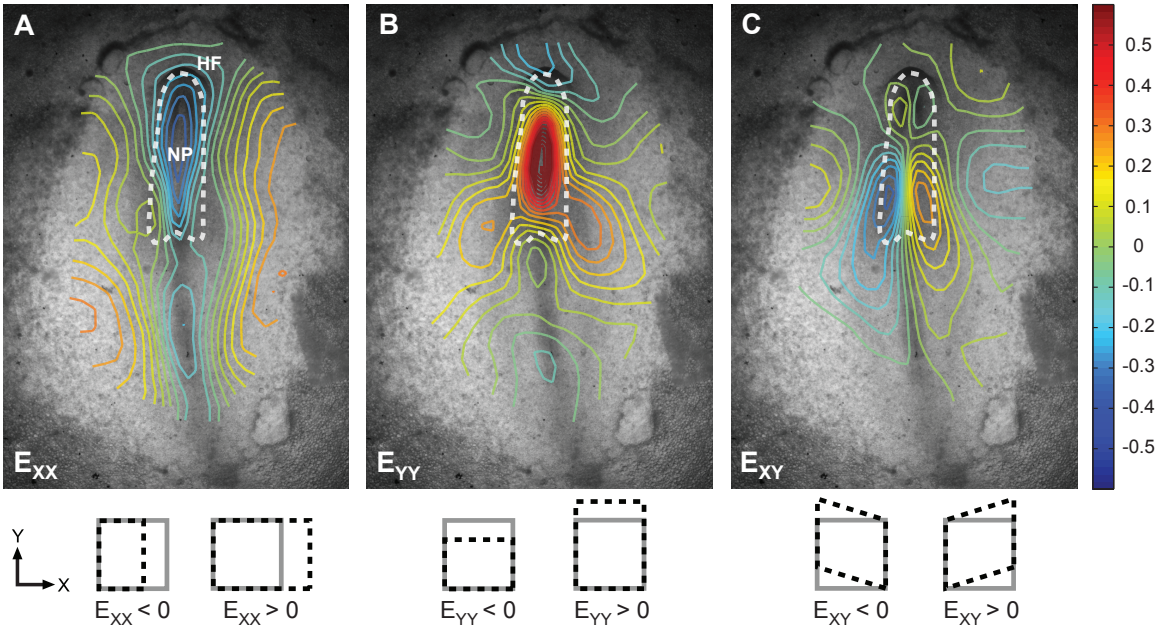

Figure 4.7: **Measured morphogenetic strain distributions are inhomogeneous.** Lagrangian strain contours were calculated for HH stage 6 relative to stage 5. **(A)** Transverse (E_{XX}) and **(B)** longitudinal (E_{YY}) strains characterize the length changes of line elements originally oriented along the X and Y axes, respectively. **(C)** The shear strains (E_{XY}) correspond to angle changes between line elements. Each distribution was non-uniform and relatively symmetric about the embryonic midline. Contours from representative embryo (n=5) are shown. The neural plate (NP) elongated longitudinally ($E_{YY} > 0$) and shortened transversely ($E_{XX}) < 0$, while the normal strains near the head fold (HF) were negative ($E_{XX} < 0$ and $E_{YY} < 0$) . A local peak in shear overlapped the lateral NP border.

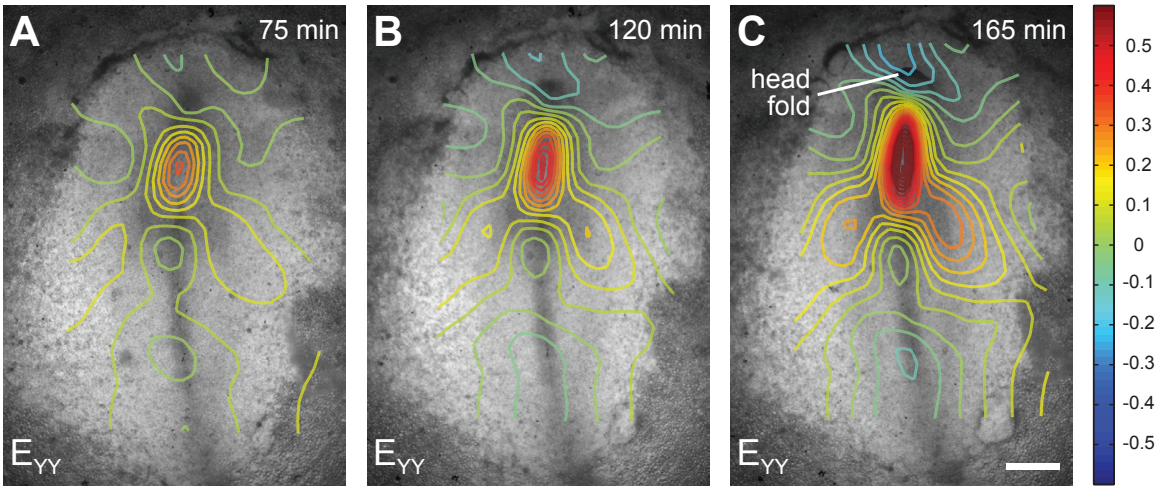

Figure 4.8: **Evolving longitudinal strain distributions.** Longitudinal Lagrangian strains were calculated relative to HH stage 5 after (A) 75 min, (B) 120 min, and (C) 165 min of incubation. These strains characterize the length changes of line elements originally oriented along the Y-axis (in the stage 5 embryo). The overall strain patterns were remarkably similar in time. Scale bar = 500 μm.

patterns were remarkably similar; only the component magnitudes varied in time (Fig. 4.8).

4.3.4 Stress inhomogeneity and anisotropy develops as head fold forms

We estimated the stress distribution in the blastoderm at different stages of development by excising circular plugs of tissue and measuring the resultant hole geometry immediately after wounding (Fig. 4.9). With a and b being the major and minor axes of the ellipse fit to a given wound, we computed the wound area, anisotropy index (b/a), and orientation (direction of the major axis). Wound geometry was compared to that of the circular punching pipette of diameter d.

At stage 4, before either the HF had formed or NP had elongated, the wounds were relatively circular, about 45% larger than the punching pipette, and similarly sized both inside and outside the NP (black and red holes/bars in Fig. 4.9B,E,F). These data indicate that the blastoderm is initially in a state of approximately uniform, isotropic tension.

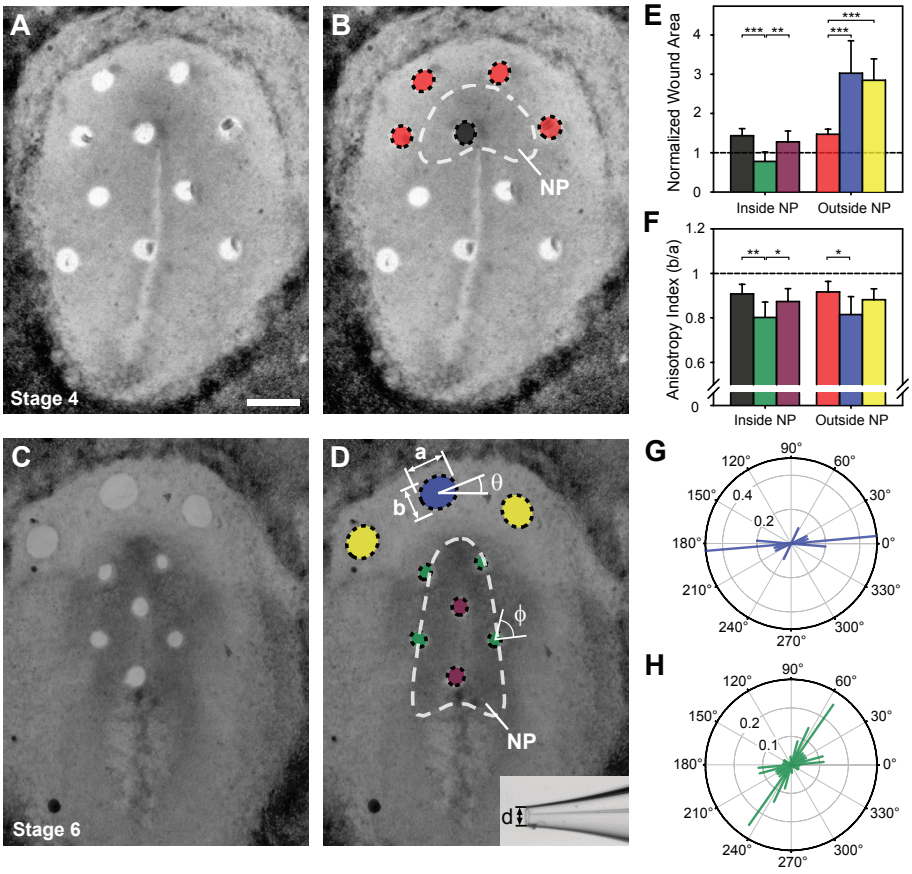

Figure 4.9: **Stress anisotropy develops as head fold (HF) forms. (A-D)** Hole punching experiment of (A,B) HH stage 4 and (C,D) stage 6 embryo (NP = neural plate). (Note that A and B are the same image, as are C and D.) Wound geometry was used to estimate regional tissue stress. Best-fit ellipses were computed for each wound with major and minor elliptical axes a and b, respectively. Wound area and anisotropy index (b/a) were compared to that of the circular punching pipette with diameter d (D, inset). Scale bar = 500 μm. At stage 4, red = outside NP and black = inside NP; at stage 6, blue = anterior to HF, yellow = lateral to HF, green = NP border, purple = middle NP. θ = angle measured from transverse embryonic (or X) axis, ϕ = angle measured from normal to NP border. **(E,F)** Quantitation of (E) wound area (normalized to the area of the pipette), and (F) anisotropy index both inside and outside the NP, as indicated (black, n=3; red, n=3; blue, n=9; yellow, n=7; green, n=9; purple, n=4). * = $P < 0.05$, ** = $P < 0.01$, *** = $P < 0.001$ (nested ANOVA with Tukey post-hoc test). **(G,H)** Relative frequency circular histograms of wound orientation (G) anterior to the HF and (H) along the NP border in stage 6 embryos. The 95% confidence intervals for (G) θ and (H) ϕ were $10° \pm 14°$ and $43° \pm 11°$, respectively. At stage 4, the blastoderm is approximately in a state of isotropic, uniform tension. During HF formation, however, the mechanical stresses become markedly anisotropic and non-uniform, especially anterior to the HF and along the NP border.

As the HF forms (at stage 6), the stresses in the blastoderm become markedly non-uniform and anisotropic (other colors in Fig. 4.9D,E,F). Outside the NP, wound size increased dramatically, indicating a significant rise in tension from that at stage 4. Moreover, anterior to the NP (blue), this state of increased tension was anisotropic, as revealed by the wounds becoming more elliptical (b/a smaller). Along the NP border (green), the wounds were smaller (approximately 78% the size of the punching pipette) and indicated the presence of compressive stresses. Here again, the elliptical shape of the wounds connoted a definite anisotropy to the stresses in this region. In the middle of the NP (purple), however, the wound size was similar to that at stage 4 (about 28% larger than the pipette area) and revealed a relatively constant, tensile stress state.

We used wound orientation to characterize the direction of anisotropy. Anterior to the NP, a dominant line of tension was oriented along the transverse embryonic axis (Fig. 4.9D,G). Meanwhile, along the NP border, the anisotropy was oriented oblique to the border, as indicated by the anterior slant of the wounds in this region (Fig. 4.9D,H).

4.3.5 Model captures head fold geometry during normal development

As discussed in section 4.2, our computational model consists of two flat plates, corresponding to the blastoderm and VM, separated by a narrow interstitial space (Fig. 4.4). The simulation includes three morphogenetic processes: (1) convergent extension of the NP, (2) cell wedging along the anterior NP border, and (3) autonomous epidermal shaping anterior to the NP.

The magnitudes of the driving forces, i.e., the components of the growth tensor $\mathbf{G}$, were determined using data from normal embryos (Fig. 5.8). With these values, the model produces a characteristic crescent-shaped HF (Fig. 4.11A), and a midline section through the model shows the HF raised above the plane of the surrounding blastoderm as observed in experiments (Fig. 4.11B).

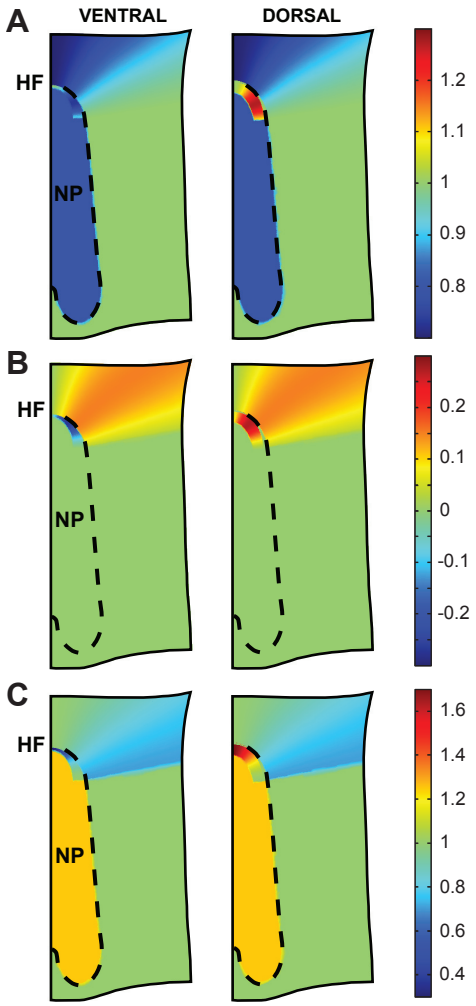

Figure 4.10: **Components of the growth tensor G in model.** Specified spatial variation of the growth components along the dorsal and ventral surfaces of the blastoderm in Cartesian coordinates. **(A)** G_{XX}, **(B)** G_{XY}, and **(C)** G_{YY}. Simulated cell wedging (along the anterior border of the neural plate (NP)) produces the only difference between the ventral and dorsal distributions. (HF = head fold)

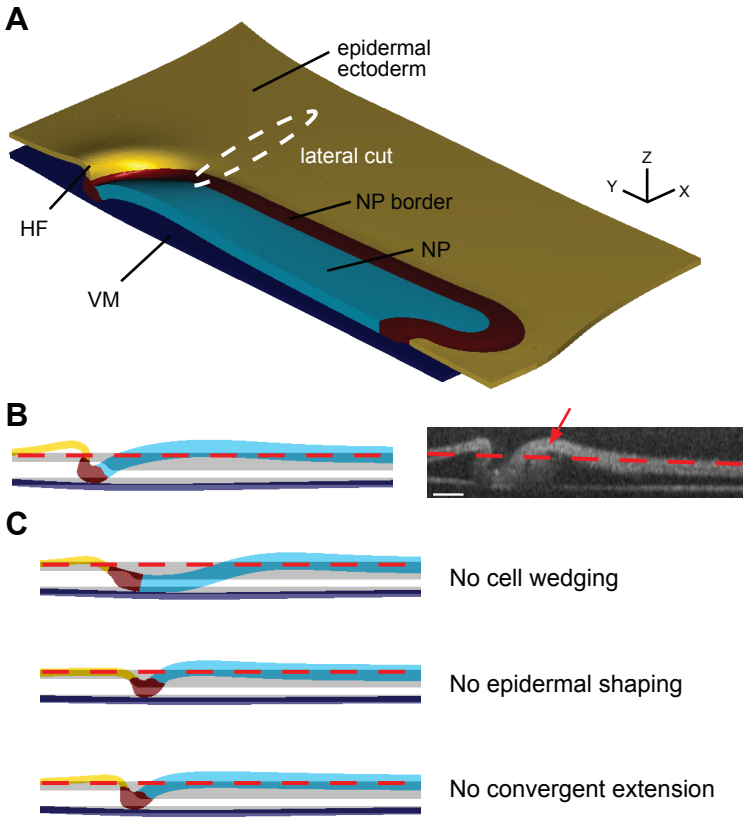

Figure 4.11: **Model captures normal head fold (HF) morphology (A)** The deformed model geometry has a characteristically crescent-shaped HF. **(B)** A midline section of the model (left) shows the HF lifted above the plane of surrounding material (red dashed line) and captures the key geometrical features seen experimentally via OCT (right). The model, however, was unable to completely reproduce the local curvature in the blastoderm just posterior to the HF (red arrow). Gray (shadowed) section indicates the undeformed model geometry. Scale bar = 200 μm. **(C)** Removing any one of our morphogenetic forces alters the simulated HF geometry.

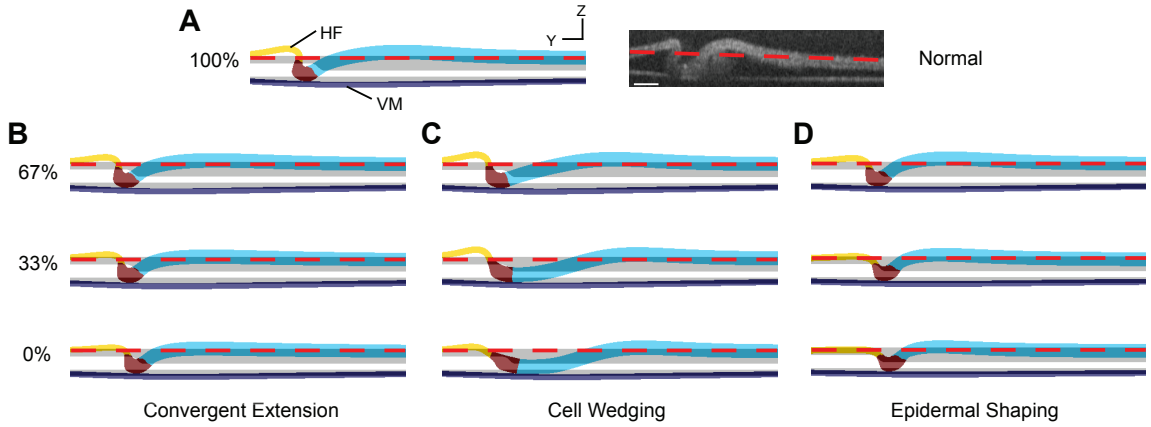

Figure 4.12: **Model robustness.** The components of the growth tensor **G** were varied to incrementally (and individually) phase out each of the morphogenetic forces in the model and determine the resultant effect on predicted HF morphology. Midline sections were then compared to **(A)** the original model. Percentages represent the percent reduction of the components of **G** from normal values. Variations of up to 33% for **(B)** convergent extension, **(C)** cell wedging, and **(D)** epidermal shaping did not drastically change the shape of the HF. Scale bar = 200 μm.

All three morphogenetic processes, which occur simultaneously in the embryo, are required (Fig. 4.11C). The model solution is fairly robust; variations of up to 33% in the growth parameters do not drastically modify the deformed geometry (Fig. 4.12). This solution, however, is not necessarily unique. Thus, to strengthen our confidence in the model, we tested it using additional experimental data.

4.3.6 Model qualitatively matches measured strain distributions

Global changes in shape do not uniquely characterize the kinematics of a deforming body, as multiple strain patterns can produce the same overall change in shape. So, to further test the model, we compared strain distributions given by the model to our experimental strain data (Fig. 4.13). For consistency with the experimental strains, 2D numerical strains were calculated by considering only displacements parallel to the XY-plane. Both model and experimental strains are computed with respect to the initially stretched configuration at stage 5.

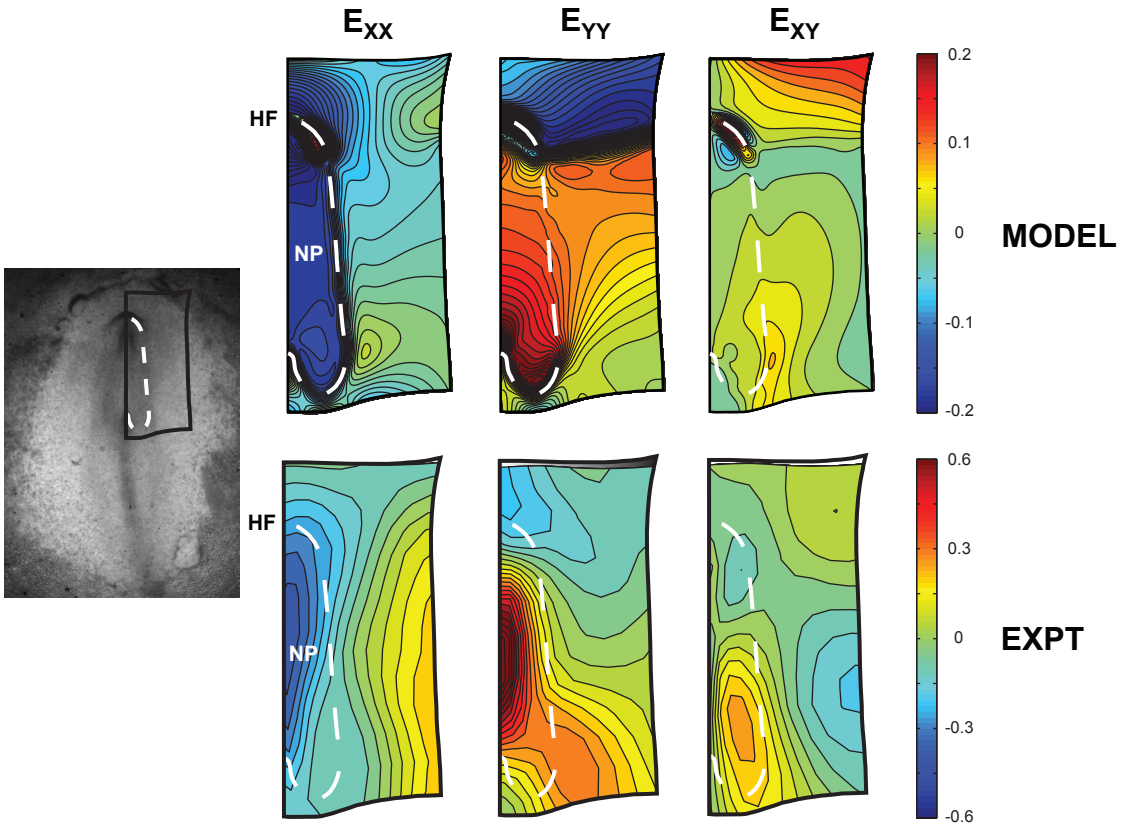

Figure 4.13: **Numerical strain fields qualitatively match experiments.** Transverse (E_{XX}), longitudinal (E_{YY}), and shear (E_{XY}) strain contours were computed in the model and compared with our experimental strain data (see Fig. 4.7). The strain fields are in reasonable agreement. Both show $E_{XX} < 0$ and $E_{YY} > 0$ in the neural plate (NP), and $E_{XX} < 0$ and $E_{YY} < 0$ anterior to the NP. The model also predicts continuous E_{XY} across the NP border and the local E_{XY} peak near the border. (HF = head fold)

The strain fields are in reasonable agreement qualitatively (Fig. 4.13), as both show transverse shortening ($E_{XX} < 0$) and longitudinal elongation ($E_{YY} > 0$) in the NP, as well as shortening in both directions anterior to the NP ($E_{XX} < 0$ and $E_{YY} < 0$). Moreover, the model predicts the continuous shear strains (E_{XY}) across the NP border, as well as the local peak near the border. The model, however, does not capture all of the striking spatial patterns seen experimentally, namely the mediolateral E_{XX} gradient (Fig. 4.13).

4.3.7 Model captures experimental anisotropy in tissue stress

We also compared the stresses in the model to the results from our hole punching experiments. The eigenvalues and eigenvectors of the Cauchy stress tensor $\boldsymbol{\sigma}$ specify the principal stresses (σ_1, σ_2) and principal stress directions, respectively, and provide a coordinate-invariant description of the stress state at each material point. We computed normalized principal Cauchy stresses ($\bar{\sigma}_{1,2} = \sigma_{1,2}/\mu_S$) to identify regions of tension and compression in the model. Because each hole was punched through the full thickness of the blastoderm, all model stresses were averaged across the thickness of the membrane.

Consistent with our hole punching experiments (Fig. 4.9B), an initial equibiaxial tension was specified along the boundary of the model blastoderm, yielding a normalized isotropic pre-stress of 0.22 within the NP and 0.43 in the surrounding epithelium. After the HF forms, principal stress distributions given by the model show qualitative agreement with our hole punching data (Figs 4.14A,B). As in experiments, the model predicts compressive stresses along the NP border and anterior NP, and captures the strongly tensile stresses outside the NP.

We also used the computed principal stress distributions to simulate our hole punching protocol. At points corresponding to experimental wound locations, the principal stresses were extracted from the HF model and imported into a relatively simple plane-stress model, consisting of a materially identical square membrane. The imported principal stresses were specified along the membrane edges, and a circular hole was introduced at the center of the stretched membrane to simulate wounding. The deformed wound geometry was compared to experiments, and principal stress directions in the HF model were compared against experimental measures of wound orientation. Further details for such a model can be found in chapter 3.

The sizes and shapes of the holes given by this method qualitatively match the wound geometries from our hole punching experiments (Fig. 4.14B). For example, anterior to the HF, the simulated wound indicates a state of anisotropic tension similar to that seen experimentally (Fig. 4.14B). Moreover, the predicted dominant line of tension, oriented along the transverse embryonic (or X) axis, also matched our experiments (Fig. 4.14C). The model also captures the anisotropic compression observed along the

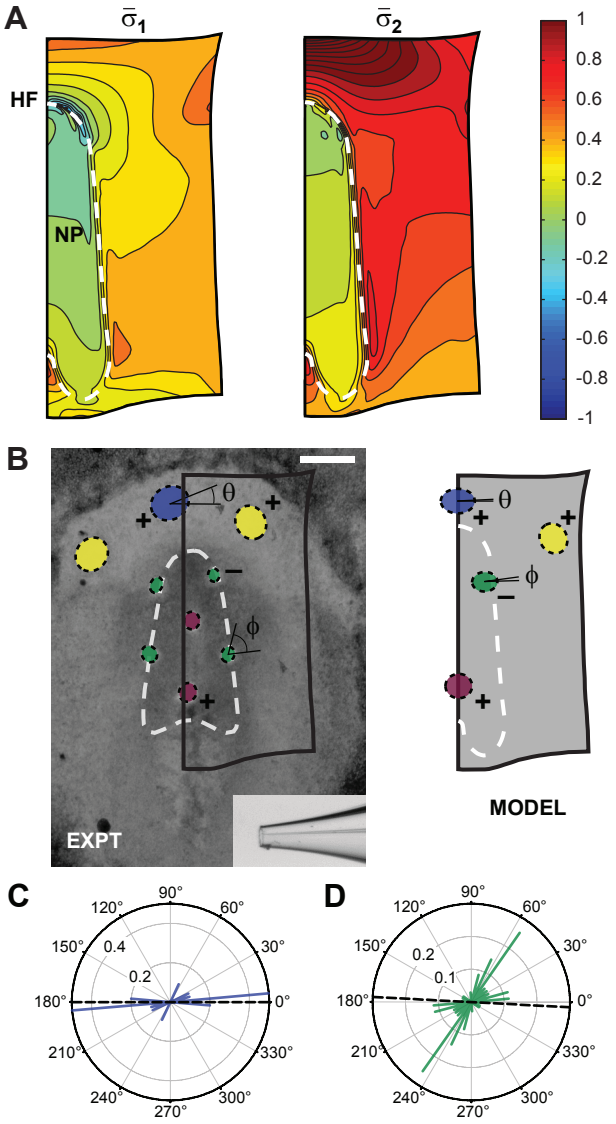

Figure 4.14: **Model predicts anisotropy in tissue stress.** The principal stresses in the model agree qualitatively with our hole punching experiments. **(A)** Normalized principal Cauchy stress contours ($\bar{\sigma}_{1,2} = \sigma_{1,2}/\mu_S$) given by the model indicate strongly tensile and anisotropic stresses anterior to the head fold (HF), compressive stresses along the anterior neural plate (NP) and NP border, and a nearly isotropic, tensile stress state in the posterior NP. **(B)** Simulations of our hole punching experiments predict similar wound shapes (see Fig. 4.9; blue = anterior to HF, yellow = lateral to HF, green = NP border, purple = middle NP). The symbols + and − indicate tension and compression, respectively. **(C,D)** Simulated wound orientation data (C) anterior to the HF and (D) along the NP border was compared with experiments. The model predicts a dominant line of tension anterior to the HF at $\theta = 0°$ (dashed black line in (C)), similar to the $\theta = 10° \pm 14°$ observed experimentally (blue bars). Along the NP border, the simulation gives $\phi = -3°$ (dashed black line in (D)), whereas in experiments, $\phi = 43° \pm 11°$ (green bars).

NP border, though the hole is oriented nearly normal to the NP border, not oblique as observed experimentally (Fig. 4.14D).

4.3.8 Model predicts abnormal morphology when development is perturbed

Mechanical perturbations were used to test the predictive capabilities of the model. Our OCT images (Fig. 4.5C) suggest that contact with the VM constrains the deformation of the blastoderm as it folds. To determine its role in shaping the HF, we removed the VM from stage 5 embryos and followed their development for 2–3 hours of culture. Midline sections reveal abnormal HF geometry, with the fold being less sharp and the HF no longer elevated above the plane of surrounding blastoderm (Fig. 4.15A).

We simulated this experiment by removing the VM in the model, without changing any of the other model parameters. The predicted morphology is similar to that seen in our OCT images (Fig. 4.15E, middle row), though the V-shaped blastoderm is not as symmetric in the model as in the actual embryo.

In a separate set of experiments, we altered the stress field in the tissue by cutting through the lateral blastoderm (outside the NP) in embryos that had already formed a HF (Fig. 4.15B-D). These linear cuts relieved the stress at these locations, and the opening of the wounds indicated a state of tension consistent with our punch experiments (Fig. 4.9D). OCT images showed that, immediately after cutting, the HF began to unfurl (Fig. 4.15B,C). After an hour of incubation (Fig. 4.15D), the HF had unfolded even further, indicating a vital morphogenetic role for the tension outside the NP.

To model this experiment, a lateral incision was simulated by removing a thin, elliptic cylindrical volume of material from the blastoderm (Fig. 4.11A). The simulation was then run with none of the model parameters modified. The predicted shape of the blastoderm is remarkably similar to that in the treated embryos, as the invagination is V-shaped with the HF being much less prominent and remaining close to the plane of the embryo (Fig. 4.15E, bottom row).

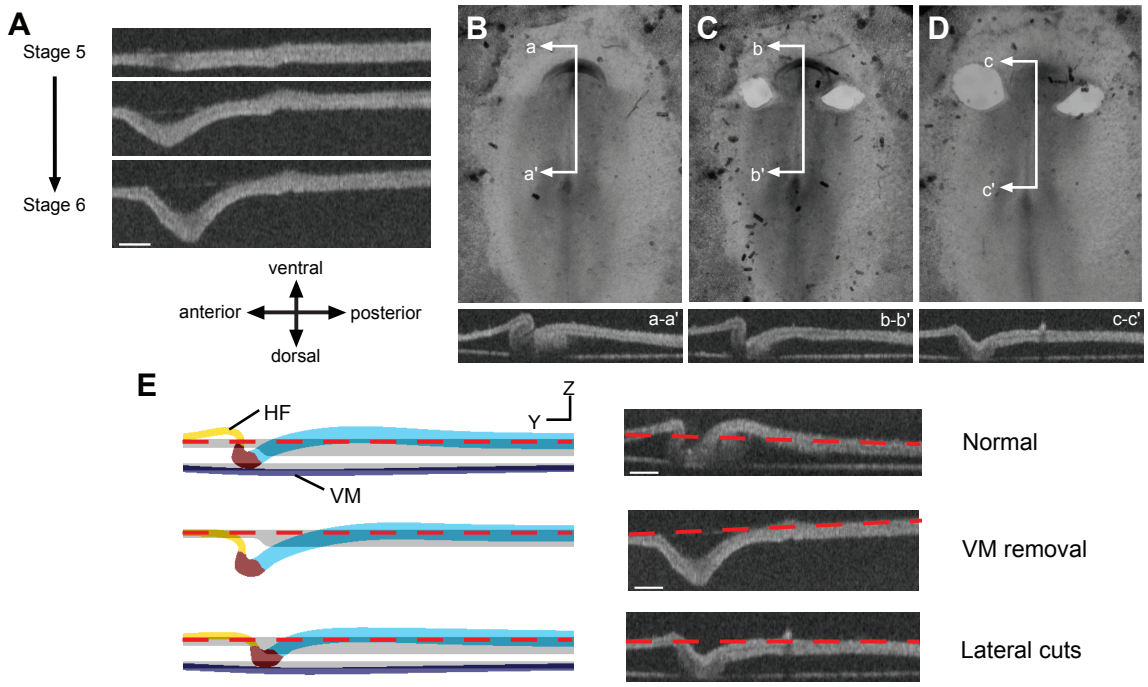

Figure 4.15: **Effect of mechanical perturbations on head fold (HF) morphology. (A)** Midline time-lapse OCT sections of embryo after removal of the vitelline membrane (VM) at HH stage 5 (n=3). **(B-D)** Linear cuts in lateral blastoderm (n=4) reveal tensile stress state. Midline OCT sections (B) before treatment (a-a'), (C) immediately after cutting (b-b'), and (D) after 1 hour incubation (c-c') show the HF progressively unfurling. **(E)** Simulating each of these perturbations by eliminating the VM (middle row) and removing a thin, elliptical cylindrical volume of lateral blastoderm (bottom row, see Fig. 4.11A) produced similarly abnormal tissue geometries. Scale bars = 200 μm.

Taken together, these results show that our model captures the fundamental mechanical behavior of the embryo during HF formation. The ability of the model to predict the abnormal tissue geometries encountered during mechanical perturbations offers further support for our proposed morphogenetic mechanisms.

4.4 Discussion

The mechanical forces that shape developing tissues have long intrigued embryologists. In fact, before the introduction of modern genetic and molecular techniques, much of the language used to describe morphogenesis was decidedly mechanical in nature (Bellairs, 1953; Stalsberg and DeHaan, 1968; Patten, 1971; Ettensohn, 1985). Though this biophysical thinking about embryogenesis largely fell out of favor in the 1970's and 80's, recent work has begun to connect our accumulated genetic and molecular understanding of development with physical morphogenetic mechanisms (Davidson, 2008; Lecuit, 2008; Wozniak and Chen, 2009; Zhou et al., 2009). New progress on the mechanics of morphogenesis is being made in the study of Drosophila dorsal closure (Blanchard et al., 2009; Gorfinkiel et al., 2009; Solon et al., 2009) and germ band extension (Rauzi et al., 2008; Blanchard et al., 2009), avian gastrulation (Zamir et al., 2006), amphibian neurulation (Chen and Brodland, 2008), cardiac looping (Taber, 2006; Ramasubramanian et al., 2008), and vertebrate convergent extension (Zhou et al., 2009; Davidson et al., 2010).

Here, we propose a new hypothesis for the mechanics of HF formation. As discussed below, our hypothesis is based on experimental studies going back more than a century.

4.4.1 Need for a new hypothesis

The HF is a crucial, yet somewhat overlooked, event in morphogenesis. Besides its role in initiating neurulation, the HF is closely linked to formation of the primitive foregut and heart tube in both chicks (Bellairs and Osmond, 2005) and humans

(Moore et al., 2000; Oostra et al., 2007). In particular, the HF creates the rudimentary foregut pocket (Lillie, 1952; Bellairs, 1953; Schoenwolf and Smith, 2000) and serves as the initial site of fusion for the precardiac epithelia (Stalsberg and DeHaan, 1969; Wei et al., 2001; Moreno-Rodriguez et al., 2006). The out-of-plane bending of the blastoderm convects and rotates the heart fields into their proper ventral position, enabling them to form a tube along the ventral aspect of the embryo (Drake and Jacobson, 1988; de la Cruz and Sanchez-Gomez, 1998; Slack, 2006; Abu-Issa and Kirby, 2008). The importance of the HF to these processes was convincingly demonstrated in the classic experiment by DeHaan (1959), where a simple incision through the HF disrupted both heart field fusion and foregut formation.

HF formation was, in fact, one of the very first morphogenetic processes to draw the attention of early embryologists. As early as 1881, in his seminal *Treatise on Comparative Embryology*, Francis Balfour described the avian HF as a "tucking in" of the blastoderm, a description which seemed to suggest a role for active folding of the tissue (Balfour, 1881; Foster and Balfour, 1883). A few years later Shore and Pickering (1889) explicitly challenged this idea, proposing instead that differential growth drives HF morphogenesis. Specifically, they posited that the embryonic area of the blastoderm grows faster than the surrounding extra-embryonic area; the blastoderm then buckles out of plane to form the HF as the embryonic area "[grows] forwards...over the portion of the area pellucida which lies in front of it." In their view, this alternative hypothesis explained away the role for any active folding or "tucking in" of the tissue. In addition, consistent with our own findings (Figs 4.5C, 4.15E), the authors speculated that mechanical contact with the VM plays a role in shaping the HF.

In the mid-twentieth century, Stalsberg and DeHaan (1968), building on work by Bellairs (1953), suggested a different buckling mechanism. They proposed that regression of Henson's node pulls the embryonic midline (i.e., Shore and Pickering's embryonic area) downward, causing the blastoderm to buckle and roll over the fixed anterior border of the NP. This folding forms the HF and initiates foregut development.

Their buckling mechanism, however, is inconsistent with our experiment in which a HF develops without a direct connection to Henson's node (Fig. 4.16). We thus propose a new hypothesis for HF formation that includes many of the active ectodermal

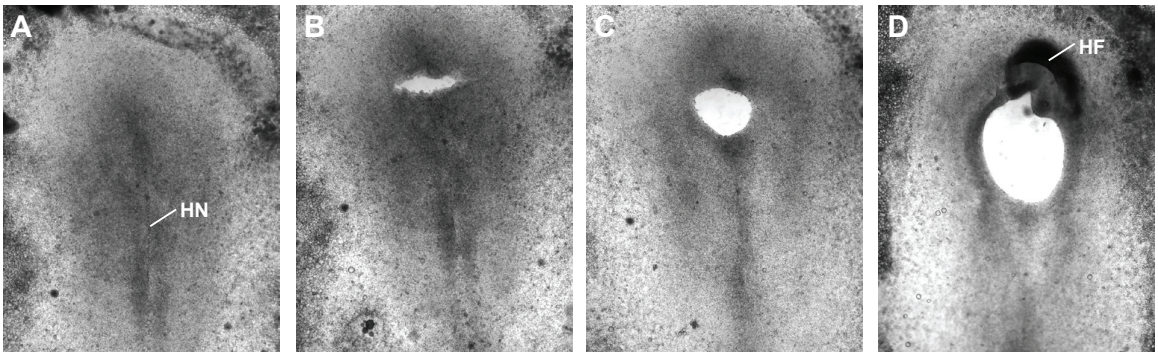

Figure 4.16: **Testing the buckling mechanism of Stalsberg and DeHaan (1968).** A linear incision across the midline severs any connection to Henson's node but does not disrupt HF formation. Embryo at HH stage 5 **(A)** before treatment, **(B)** immediately after cutting, **(C)** after 2 hours of culture, and **(D)** after 7 hours of culture.

processes which shape the neural tube. Specifically, we postulate that (1) active cell wedging at the NP border, (2) convergent extension of the NP, and (3) epidermal shaping anterior to the NP generate the mechanical forces that drive this process. This hypothesis is motivated by the following experimental results.

First, Lawson et al. (2001) demonstrated that localized cell wedging accompanies the epithelial bending (or kinking) that occurs along the NP border, and this behavior appears intrinsic to the border zone itself (Moury and Schoenwolf, 1995). The cellular mechanisms that drive this wedging, however, have yet to be determined, but may include actomyosin contraction (Gorfinkiel et al., 2009; Martin et al., 2009), interkinetic nuclear migration (Smith and Schoenwolf, 1988; Schenk et al., 2009), or laminin-dependent basal constriction (Gutzman et al., 2008).

Second, it has also been well established that the NP elongates by convergent extension (Smith and Schoenwolf, 1997; Colas and Schoenwolf, 2001; Ezin et al., 2009). External loads may play a role in this process, but that role appears to be a subsidiary one, as convergent extension occurs within NP isolates (Moury and Schoenwolf, 1995) and has been attributed to both cell intercalation (Schoenwolf and Alvarez, 1989; Ezin et al., 2009) and coordinated cell division (Sausedo et al., 1997).

Third, the epidermal ectoderm anterior to the NP actively shortens in the transverse direction (Moury and Schoenwolf, 1995). Though the cellular mechanisms behind this epidermal shaping are still unclear, there is evidence that coordinated cell division

plays a role. The orientation of these dividing cells (i.e., the direction along which tissue growth occurs) may depend on mechanical stress (Sausedo et al., 1997).

4.4.2 Computational models help elucidate morphogenetic forces

We have integrated computational modeling and in vitro experiments to determine the tissue-level forces that drive HF formation. In highly nonlinear problems (like this one), physical intuition can often be misleading, and models are a useful tool, enabling us to quantitatively investigate whether a given hypothesis is consistent with physical law.

Morphological and mechanical experiments can be used to test the model. However, in problems of morphogenesis, it is important to note that matching global tissue geometry does not guarantee a unique solution, and other types of experiments (e.g., stress, strain) can be used to test the model more rigorously.

To test our hypothesis for HF formation, we constructed a 3D computational model that consists of two pseudoelastic plates, corresponding to the blastoderm and VM. A continuum mechanics framework is used because we are concerned here with global tissue deformations. The model geometry, material constants, and boundary conditions are all based on experimental observations in normal chick embryos. We used 3D OCT reconstructions, morphogenetic strain distributions, and qualitative stress estimates to test the model and identify reasonable values for the free parameters (i.e., the components of $\mathbf{G}$), which determine the magnitude of the hypothesized driving forces.

The model matches the HF geometry observed in living embryos using OCT (Figs 4.5,4.11). Though it captures the key geometrical features, the model does not, however, reproduce the local curvature in the blastoderm just posterior to the HF (arrow in Fig. 4.11B). One reason for this discrepancy may be our assumption of uniform growth (i.e., convergent extension) in the NP, as there is some evidence that the extent of cell rearrangement varies along the embryonic midline (Schoenwolf and Alvarez, 1989). Alternatively, apical constriction of median hinge-point cells along

the midline (Lee and Nagele, 1985; Colas and Schoenwolf, 2001) may further enhance this local curvature.

The model also qualitatively matches our morphogenetic strain data (Fig. 4.13), which, consistent with existing data on avian convergent extension, shows the NP elongating longitudinally ($E_{YY} > 0$) and shortening transversely ($E_{XX} < 0$) (Schoenwolf and Sheard, 1989; Smith and Schoenwolf, 1997; Colas and Schoenwolf, 2001; Ezin et al., 2009). Moreover, in both the model and experiments, the negative transverse strains (E_{XX}) surrounding the HF are in agreement with previously reported evidence of epidermal shaping (Moury and Schoenwolf, 1995), and the shear strains (E_{XY}), akin to the reorientation movements described by Ezin et al. (2009), are the result of NP growth being constrained by surrounding tissue. Interestingly, the difference in material properties between the NP and surrounding tissue (that is, between μ_{NP} and μ_S) is such that the shear strains are continuous across the NP border.

A lack of complete agreement between the strain distributions given by the model and our experimental data could be attributed to either the model geometry or our assumption of uniform growth. In the model, the thickness of the blastoderm is uniform outside the NP; however, transverse OCT sections indicate that the blastodermal thickness decreases toward the periphery of the embryo. This could contribute to the laterally increasing E_{XX} gradient observed in experiments (Fig. 4.13), since the thinner (lateral) material would deform to a greater extent under the stresses exerted by the narrowing NP. Alternatively, the effects of non-uniform growth could also be a factor.

To our knowledge, this work constitutes the first study of mechanical stress in HF-stage chick embryos. Before HF morphogenesis, the blastoderm is in a state of uniform, isotropic tension; as the HF forms, however, the stress distribution becomes both inhomogeneous and anisotropic (Fig. 4.9). Our model effectively captures this non-uniform stress field (Fig. 4.14), predicting both compressive and tensile stresses in the NP, and large tensile stresses in the blastoderm surrounding it. In addition, the model predicts the dominant line of tension observed anterior to the HF (Fig. 4.14C).

Lastly, to gauge the predictive capability of the model, we simulated two mechanical perturbation experiments that disrupted the normal stress field: lateral cutting of the

blastoderm and VM removal. Rather strikingly, the model reasonably captures the abnormal tissue geometry in both cases (Fig. 4.15E).

4.4.3 Head fold is shaped by forces typically associated with neurulation

These results suggest that our hypothesized morphogenetic mechanisms, which include those typically associated with neurulation, are the primary driving forces behind HF formation. Given its central importance to both heart tube and foregut formation, a more complete biophysical understanding of this crucial morphogenetic event should give insight into how embryonic tissues are organized during early cardiac development.

By characterizing the forces that shape the HF during normal development, future work can be done to determine how molecular or genetic perturbations mechanically disrupt this process. In mice, for example, inactivation of the Huntington's disease gene *Hdh* disrupts early embryonic patterning and completely blocks HF formation (Duyao et al., 1995; Woda et al., 2005). How this aberrant patterning influences the morphogenetic forces that shape the HF, however, remains unclear. Other results provide further evidence of a link between head and heart development. In chicks, Rho kinase (ROK) expression is enriched in the HF, and inhibition of ROK, which is implicated in cytoskeletal organization, often generates embryos with cardia bifida, particularly if the inhibitor is applied before the HF has formed (Wei et al., 2001). Here again, the biophysical consequences of this perturbation are unknown and warrant further attention.

The integrated use of quantitative modeling and experiments is well-suited to answer these questions, and the approach presented here can be readily generalized to other morphogenetic processes, offering us a chance to understand how physical forces are organized at the tissue-level to create biological form.

Chapter 5

Not just inductive: a critical mechanical role for the endoderm during heart tube assembly

Summary

The heart is the first functioning organ to form during development. During gastrulation, the cardiac progenitors reside in the lateral plate mesoderm but maintain close contact with the underlying endoderm. In amniotes, these bilateral heart fields are initially organized as a pair of flat epithelia that move toward the embryonic midline and fuse above the anterior intestinal portal (AIP) to form the heart tube. This medial motion is typically attributed to active mesodermal migration over the underlying endoderm. In this view, the role of the endoderm is two-fold: to serve as a mechanically passive substrate for the crawling mesoderm and to secrete various growth factors necessary for cardiac specification and differentiation. Here, using computational modeling and experiments on chick embryos, we present evidence supporting an active mechanical role for the endoderm during heart tube assembly. Label-tracking experiments suggest that active endodermal shortening around the AIP accounts for most of the heart field motion toward the midline. Results indicate that this shortening is driven by cytoskeletal contraction, as exposure to the myosin-II inhibitor blebbistatin arrested any shortening and also decreased both tissue stiffness (measured by microindentation) and mechanical tension (measured by cutting experiments). In addition, blebbistatin treatment often resulted in cardia bifida and

abnormal foregut morphogenesis. Moreover, finite element simulations of our cutting experiments suggest that the endoderm (not the mesoderm) is the primary contractile tissue layer during this process. Taken together, these results indicate that contraction of the endoderm actively pulls the heart fields toward the embryonic midline, where they fuse to form the heart tube.

5.1 Introduction

The heart is the first functioning organ to develop in the embryo. In avians, early cardiac progenitor cells ingress through the anterior primitive streak during gastrulation and take up residence in the lateral plate mesoderm (Rosenquist and DeHaan, 1966; Garcia-Martinez and Schoenwolf, 1993; Cui et al., 2009). They remain in close contact with the underlying endoderm (Linask and Lash, 1986; Schultheiss et al., 1995) as they form paired coherent epithelia on either side of the embryonic midline — the so-called primary heart fields (Abu-Issa and Kirby, 2007). These epithelia (i.e., the cardiogenic mesoderm) then move toward the midline, fold out-of-plane, and fuse above the anterior intestinal portal (AIP) to form the heart tube (Stalsberg and DeHaan, 1969; Linask and Lash, 1986; Kirby, 2007; Abu-Issa and Kirby, 2008; Cui et al., 2009).

Although the physical forces that drive this process remain poorly understood, it has been generally accepted that heart field motion toward the midline is primarily due to active migration (i.e., crawling) of the cardiogenic mesoderm over the underlying endoderm (DeHaan, 1963; Rosenquist and DeHaan, 1966; Linask and Lash, 1986; Trinh and Stainier, 2004). According to this view, the role of the endoderm during cardiogenesis is considered to be two-fold: (1) to serve as a mechanical substrate for the crawling mesoderm and (2) to secrete a host of soluble growth factors which induce cardiac specification and differentiation in the adjacent cardiogenic mesoderm (Schultheiss et al., 1995; Nascone and Mercola, 1995, 1996; Schultheiss et al., 1997; Lough and Sugi, 2000; Alsan and Schultheiss, 2002).

Here, using computational modeling and experiments with chick embryos, we show that the endoderm may also play a crucial mechanical role during cardiogenesis. Our results suggest that the endoderm actively shortens around the AIP, pulling the

overlying mesoderm toward the midline. Although relative motion between the germ layers (likely associated with active migration) is evident, most of the mesodermal motion is driven by active deformations in the endoderm. Our experiments indicate that actomyosin contraction generates this endodermal shortening, as the myosin II inhibitor blebbistatin arrests any shortening and (in most cases) results in cardia bifida. Microindentation tests before and after the application of blebbistatin also show a reduction in tissue stiffness, which is associated with contraction. Finally, dissection experiments indicate a state of contraction-induced tension around the AIP, and finite element simulations of these experiments identify the endoderm as the dominant contractile tissue layer. Taken together, these results suggest that, in addition to its inductive signaling role, the endoderm also plays a crucial mechanical role during heart tube assembly.

5.2 Materials and methods

5.2.1 Experimental methods

Embryo preparation and culture

Fertilized White Leghorn chicken eggs were incubated in a humidified, forced draft incubator at 38°C for 24 to 35 hours to yield embryos between Hamburger and Hamilton (HH) stages 5 and 9 (Hamburger and Hamilton, 1951). Whole embryos were harvested from the eggs using a filter paper carrier method (Voronov and Taber, 2002). The embryo and underlying vitelline membrane were kept intact, thereby preserving the stresses normally present in the tissue. Each embryo was then placed ventral side up in a 35 mm culture dish, and completely submerged under a thin layer of liquid culture media and incubated at 38°C in 95% O_2 and 5% CO_2. This method prevents artifacts caused by fluid surface tension, which alter the mechanical stresses in the embryo (Voronov and Taber, 2002).

In some experiments, embryos were cultured in 100 μM (–)-blebbistatin (Sigma, St. Louis, MO) to broadly suppress any cytoskeletal contraction dependent on myosin II.

The inhibitor could be washed out by rinsing the embryo several times in PBS and then continuing the culture with new blebbistatin-free media.

Injection labeling and tracking

To measure tissue motion in both the endoderm and mesoderm around the AIP, small groups of cells (in both germ layers) were labeled at HH stage 7+/8- with the lipophilic fluorescent dye DiI (Molecular Probes, Eugene, OR) mixed in a 20% sucrose solution. DiI injections were made using pulled glass micropipettes and a pneumatic pump (PicoPump PV830, World Precision Instruments). To label cardiogenic mesoderm, the tip of the injection pipette was first pierced through the superficial layer of endoderm.

Embryos were then cultured as above. For normal embryos (n=5), bright field and fluorescence time-lapse images were captured at approximately $\sim$2 hr intervals using a Leica DMLB microscope and attached video camera (Retiga 1300). Since certain wavelengths of light disrupt the activity of blebbistatin (Kolega, 2004), images of blebbistatin-treated embryos (n=4) were captured just prior to wash-out to minimize exposure of the embryo to light. All subsequent (i.e., post-blebbistatin) images were captured at $\sim$2 hr intervals.

Label motion was tracked using the Manual Tracking plug-in in ImageJ. Labels were confirmed to be mesodermal if they later incorporated into the beating heart tube.

Optical coherence tomography

A Thorlabs (Newton, NJ) optical coherence tomography (OCT) system with attached Nikon FN1 microscope was used to obtain cross-sectional image stacks of living embryos (n=2). Images were acquired every 5 μm across a 3 x 3 mm scanning window. Image stacks were then reconstructed into three-dimensional volumes and optically sectioned using Volocity (PerkinElmer, Waltham, MA).

Microindentation and tissue stiffness

Intact embryos (n=4) were transferred to a bath of PBS at room temperature, and tissue stiffness was measured using a custom-built microindentation device (Zamir et al., 2003). Briefly, the microindenter was attached to the end of a calibrated cantilever beam whose motion was driven by a piezoelectric motor. The measured beam deflection was then used to calculate the tissue indentation depth and applied force. As described previously, the measured force-deflection data were fit to a four-parameter exponential function, the derivative of which was used to determine the tangential tissue stiffness at 10 μm deflection (Zamir et al., 2003). Three consecutive indentations were made at each tissue location to ensure a repeatable response. To assess the effects of contraction, each embryo was then transferred to a 35 mm culture dish and incubated in 100 μM (–)-blebbistatin in PBS for 1-2 hr at room temperature. Performing this incubation step at room temperature ensured that the embryo did not develop further during these experiments. Afterward, tissue stiffness was measured again at the same locations.

Tissue microsurgery

To probe tissue stress, small linear incisions at the medial point of the AIP were made using the Gastromaster microsurgical device (Xenotek Engineering) with white tips. These experiments were performed in both a group of normal HH stage 8 embryos (n=5) and in another group of stage 8 embryos after incubation in 100 μM (–)-blebbistatin in PBS for 1-2 hr at room temperature (n=5). As discussed below, these linear incisions opened up to form triangularly shaped wounds (when viewed ventrally). The extent of this opening was quantified using ImageJ. A line segment was fit to each wound edge, and the angle between the lines was measured using the Angle Tool.

Statistics

All data are reported as mean ± SD. To compare stiffness measurements before and after treatment with blebbistatin, we used a paired t-test implemented in SigmaPlot

(Systat Software Inc., Chicago, IL). Circular statistics and a two-sample Watson-Williams test were used to analyze our wound opening-angle data (Zar, 2010).

5.2.2 Computational model

Model geometry

To help interpret our tissue cutting experiments, we constructed a nonlinear 2D finite element model of the endoderm and mesoderm around the AIP using COMSOL Multiphysics (Version 3.5, COMSOL AB, Providence, RI). As a first approximation, we consider an idealized 2D representation of the 3D tissue geometry around the AIP (Fig. 5.1). OCT sections were used to visualize this geometry in living HH stage 8 embryos (Fig. 5.1A,B). On each section, the endoderm (blue) and cardiogenic mesoderm (red) were approximately resolved by visual inspection. The cardiogenic mesoderm was shown to be a thickened epithelium in close contact with a thin superficial layer of endoderm (Fig. 5.1A,B) — a result consistent with previous morphological studies (Manasek, 1968; Patten, 1971; Drake et al., 1990; Kirby, 2007).

For our model geometry, we consider a simplified 2D slice through the cardiogenic mesoderm and endoderm around the AIP (Fig. 5.1B-D). In this idealized representation, both tissue layers are modeled as concentric circular 2D rings of material in plane stress. The inner curvature of the rings represents the contour of the AIP, and we define a polar coordinate system (r, θ), whose origin is situated at the center of the rings (Fig. 5.1D). As observed experimentally, the model mesoderm is thicker than the adjacent endoderm. Roller boundary conditions are specified along the medial and lateral edges of the model; the other edges are taken as traction free.

Theoretical framework

We use a continuum mechanical framework for large deformations, in combination with the Rodriguez et al. (1994) theory of finite volumetric growth to model the mechanics of morphogenesis. Briefly, the total deformation of a psuedoelastic body

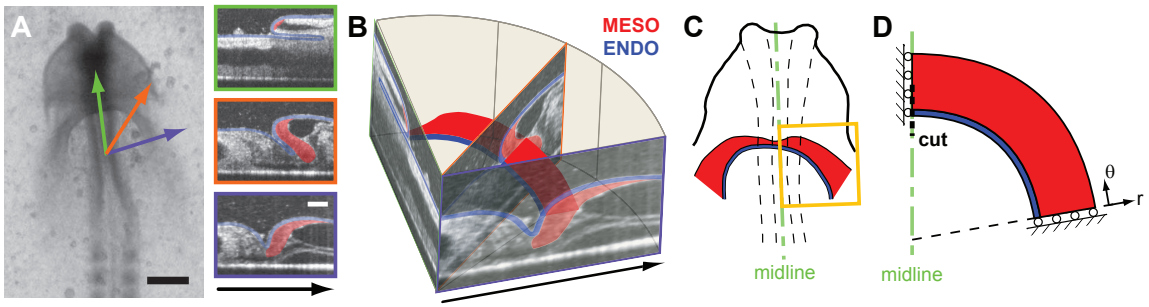

Figure 5.1: **Geometry for computational model. (A)** Bright field and OCT images of HH stage 8+ embryo. OCT sections were taken through medial (green), mediolateral (orange), and lateral (purple) locations around the AIP. On each section, endoderm (blue) and cardiogenic mesoderm (red) were resolved by visual inspection. Arrows indicate orientation of each OCT section within the embryo. Scale bars represent 300 μm (black) and 100 μm (white). **(B)** OCT sections in (A) arrayed in 3D space. We consider a 2D slice through the tissue. Note that the thickness of the mesoderm is greater than that of the the adjacent endoderm. **(C)** 2D projection of this slice overlayed with a schematic of HH stage 8+ embryo. **(D)** For our model geometry, we consider an idealized 2D representation of the tissue, and both tissue layers are modeled as concentric circular rings of pseudoelastic material. We assume bilateral symmetry relative to the embryonic midline, and the model geometry includes only the yellow boxed region in (C). A polar coordinate system (r, θ) has its origin at the center of the rings. See text for further details.

can be described by the deformation gradient tensor

$$\mathbf{F} = \mathbf{I} + (\boldsymbol{\nabla}\mathbf{u})^T , \tag{5.1}$$

where $\mathbf{I}$ is the identity tensor, $\boldsymbol{\nabla}$ is the gradient operator in the undeformed configuration, and $\mathbf{u}$ is the displacement vector between a material point P in the undeformed configuration and its image p in the deformed configuration. The tensor $\mathbf{F}$ thereby maps material points between the undeformed and deformed configurations of a body.

Contraction is simulated by negative growth, whereby $\mathbf{F}$ is decomposed into a contraction (or growth) tensor $\mathbf{G}$ and an elastic deformation gradient tensor $\mathbf{F}^*$ by the relation $\mathbf{F} = \mathbf{F}^* \cdot \mathbf{G}$ (Rodriguez et al., 1994). The tensor $\mathbf{G}$ changes the zero-stress configuration of each material element (akin to thermal contraction of a passive material), and $\mathbf{F}^*$ generates mechanical stress by both enforcing geometric compatibility between material elements and accounting for the elastic response of the material to any applied loads. This theory has been used to model several different morphogenetic processes including head fold formation (Varner et al., 2010) and cardiac c-looping

(Voronov et al., 2004; Ramasubramanian et al., 2006) in the chick embryo, cortical folding in the developing ferret brain (Xu et al., 2010), and ventral furrow formation in Drosophila (Muñoz et al., 2007, 2010).

Mechanical properties

Applied loads and mechanical deformations are coupled through the constitutive properties of the material. As a first approximation, we model both the endoderm and mesoderm as isotropic, slightly compressible, modified neo-Hookean materials characterized by the strain-energy density function

$$W = \frac{\mu}{2}\left(\bar{I}^* - 3\right) + \frac{\kappa}{2}\left(J^* - 1\right)^2, \tag{5.2}$$

where μ is the small-strain shear modulus, κ is the bulk modulus, $J^* = \det \mathbf{F}^*$ is the elastic volume ratio, and $\bar{I}^* = J^{*-2/3}\,\mathrm{tr}\,(\mathbf{C}^*)$ is a modified first invariant of the right Cauchy-Green elastic deformation tensor $\mathbf{C}^* = \mathbf{F}^{*T} \cdot \mathbf{F}^*$. Our assumption of slight material compressibility yields numerical solutions that converge more readily than when near incompressibility is enforced. Changing the bulk modulus ($\bar{\kappa} = \kappa/\mu = 1000$) by an order of magnitude does not qualitatively alter our model results.

The Cauchy stress tensor $\boldsymbol{\sigma}$ depends on $\mathbf{F}^*$ through the relation (Taber, 2004):

$$\boldsymbol{\sigma} = J^{*-1}\mathbf{F}^* \cdot \frac{\partial W}{\partial \mathbf{F}^{*T}}. \tag{5.3}$$

Stress components ($\hat{\sigma}_{ii}$) are normalized with respect to the passive small-strain shear modulus μ_p (i.e., $\hat{\sigma}_{ii} = \sigma_{ii}/\mu_p$) and reported in the convected coordinate system $(\bar{r}, \bar{\theta})$ which is embedded in the material and deforms with it. In the undeformed configuration, $(\bar{r}, \bar{\theta})$ is coincident with (r, θ). Details on how to implement this theoretical framework in COMSOL Multiphysics (Version 3.5) can be found in Taber (2008).

Simulating cytoskeletal contraction

Active contraction is specified in the model by varying the components of $\mathbf{G}$. We assume this contraction occurs only along the orthogonal directions $\mathbf{e_r}$ and $\mathbf{e_\theta}$, so

$\mathbf{G} = G_r \mathbf{e_r} \mathbf{e_r} + G_\theta \mathbf{e_\theta} \mathbf{e_\theta}$ where G_r and G_θ are contraction ratios; $G_i = 1$ for passive material and $G_i < 1$ specifies active contraction. As shown below, endodermal line elements shorten around the AIP (i.e., in the circumferential or θ-direction). We take $G_r = 1$ and $G_\theta < 1$ to simulate active circumferential contraction in either the endoderm or mesoderm. Also, since contracting tissues stiffen, a concomitant material stiffening accompanies our specified contraction (i.e., μ increases as G_θ decreases). Here, we take $\mu = \mu_p / G_\theta$, where (as a first approximation) μ_p is assumed equivalent in both the endoderm and mesoderm. More details for the model are provided below.

5.3 Results

Approximately 24 hours into the 21-day incubation period of the chick, the head fold forms at the anterior end of the blastoderm (Varner et al., 2010) and initiates formation of the foregut and anterior intestinal portal (AIP) (Bellairs, 1953; Stalsberg and DeHaan, 1968; Varner et al., 2010). At this stage of development (i.e., HH stage 7), the cardiogenic mesoderm is organized as a pair of bilateral epithelia on either side of the embryonic midline (Stalsberg and DeHaan, 1969; Moreno-Rodriguez et al., 2006; Abu-Issa and Kirby, 2008). These heart fields then move to the midline and fuse above the AIP to form the heart tube. During this period, the mesoderm remains in close contact with the endoderm around the AIP (Fig. 5.1A) (Linask and Lash, 1986; Schultheiss et al., 1995).

5.3.1 Cardiogenic mesoderm and adjacent endoderm move together toward midline

To dynamically measure the motion of the endoderm and mesoderm during heart tube assembly, we injected fluorescent DiI labels into both germ layers before the heart tube had formed (HH stage 7+/8-) (Fig. 5.2A,B). Overlapping labels were placed in the lateral region of the AIP in both the endoderm and mesoderm, and a single label was placed in the endoderm at the midline (Fig. 5.2A). Embryos were then cultured, and labels were tracked in time as the heart tube formed (Fig. 5.2B-D and see Movie 1 in the supplementary material).

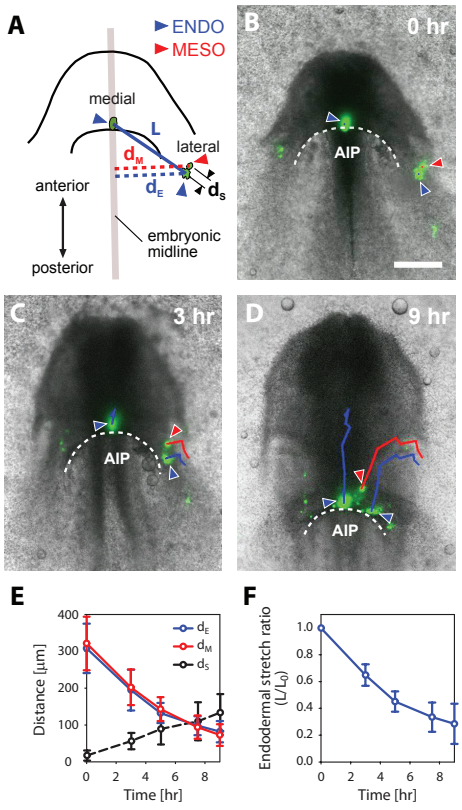

Figure 5.2: **Tracking motion of endoderm and cardiogenic mesoderm around the AIP during heart tube assembly. (A)** Schematic of representative HH stage 7+ embryo shown in (B). Overlapping mesodermal (red arrowhead) and endodermal (blue arrowhead) fluorescent labels were injected in the lateral region of the AIP, while a single fluorescent label was placed in the endoderm at the medial point of the AIP (blue arrowhead). Embryos were cultured ex ovo and labels were tracked in time as the heart tube formed. The distance of both lateral labels from the midline (d_M and d_E for the mesoderm and endoderm, respectively) was measured at each timepoint. The length L between the two endodermal labels, and the separation distance d_S between the (initially) adjacent labels in the endoderm and mesoderm were also measured. **(B-D)** Representative embryo at 0, 3, and 9 hr of incubation. Red and blue tracks represent mesodermal and endodermal label trajectories, respectively. Scale bar = 200 μm. **(E)** Distance of lateral labels from the midline (mesoderm, red; endoderm, blue), and separation distance between the labels (dashed black) plotted as functions of time (n=5). **(F)** Endodermal stretch ratio around the AIP as a function of time (n=5). The distance between endodermal labels at 0 hr (L_0) is used as the reference length. Error bars indicate ± SD. During heart tube formation, the endoderm and cardiogenic mesoderm move together toward the midline, as the endoderm shortens around the AIP. AIP = anterior intestinal portal.

As the AIP descended, the medial endodermal label did not move into the forming foregut pocket. Instead it followed a posterior trajectory and maintained a similar position relative to the regressing AIP (Fig. 5.2B-D, medial blue lines).

Both labels in the lateral region of the AIP, however, moved toward the embryonic midline (Fig. 5.2B-D, red and blue lateral lines), and of these two, the label in the mesoderm (red) incorporated into the nascent heart tube. Both germ layers approached the midline at nearly identical rates (Fig. 5.2E), and the tracked trajectories of both labels were remarkably similar, suggesting that the motions of the cardiogenic mesoderm and adjacent endoderm are correlated (Fig. 5.2D). Although the initially overlapping labels moved apart as the heart tube formed (Fig. 5.2E), likely due to active crawling of the mesoderm over the endoderm, the contribution of this migration to the medial motion of the mesoderm was relatively minor. The lateral mesoderm and endoderm essentially moved together toward the midline.

In addition, the endoderm shortened (i.e., narrowed) tangential to the AIP as the heart tube formed, as the distance between the medial and lateral endodermal labels decreased by greater than 60% (Fig. 5.2F). At HH stage 7+ (i.e., before heart field fusion), no mesoderm is present in the medial AIP (Cui et al., 2009). Since the mesoderm is not continuous across the embryonic midline, these results suggest that the medial movement of both germ layers is driven by endodermal shortening around the AIP.

5.3.2 Cytoskeletal contraction drives endodermal shortening around AIP

To explore the role of cytoskeletal contraction in this process, we cultured head fold stage embryos (HH stages 5-7) in 100 μM blebbistatin to broadly suppress the activity of myosin II. In these embryos, heart field fusion was impaired and complete cardia bifida often occurred (in 5 out of 6 embryos) (Fig. 5.3). In these cases the foregut remained open ventrally, the AIP failed to descend, and by the end of the experiment, two asynchronously beating heart tubes were observed on either side of the embryonic midline (Fig. 5.3D). Proper heart field fusion thus requires actomyosin contraction, and we speculated that this contraction drives the observed endodermal shortening.

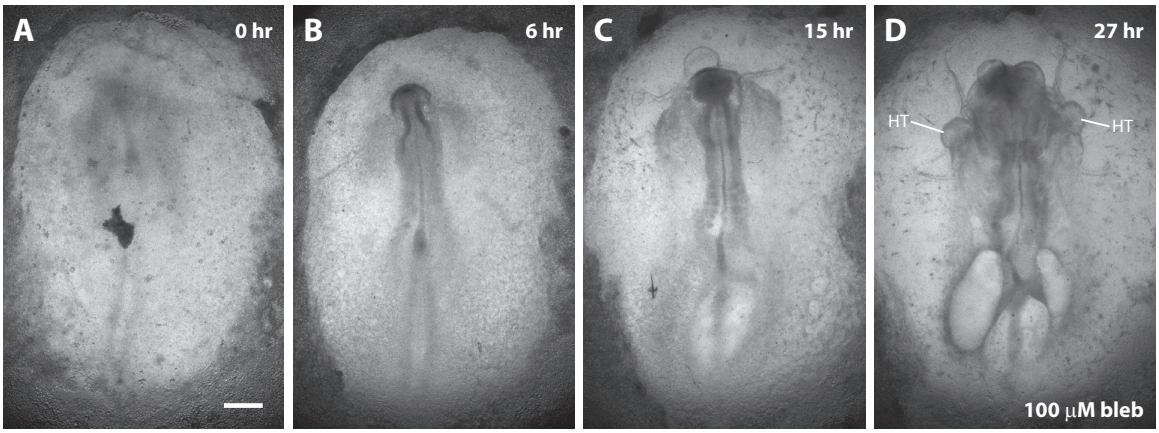

Figure 5.3: **Inhibiting myosin-II dependent contraction impairs heart field fusion and causes cardia bifida.** Representative head fold stage embryo (n=6) cultured in 100 μM blebbistatin at **(A)** 0 hr, **(B)** 6 hr, **(C)** 15 hr, and **(D)** 27 hr of incubation. At the end of the incubation period, two asynchronously beating heart tubes (HT) were observed on either side of the embryonic midline. Scale bar = 500 μm.

To test this idea, we repeated our injection labeling experiments in the presence of blebbistatin (Fig. 5.4). In these experiments only endodermal cells were labeled, as we were primarily concerned with deformations in the endoderm. After culture in 100 μM blebbistatin, the labels in the medial and lateral regions of the AIP did not move together as before. Instead the distance between them increased, indicating tissue relaxation (Fig. 5.4B,E), and the AIP did not descend as in normal embryos (compare Figs 5.2C and 5.4B). Blebbistatin was then washed out after 3 hours, and culture was continued. After the wash-out, the labels began to approach one another (Fig. 5.4C,D) and the distance between them shortened at a rate comparable to that seen in normal embryos (Fig. 5.4E). Moreover, the AIP resumed its posterior descent.

During some experiments, mesodermal cells adjacent to the lateral endoderm were also labeled. In these few cases, when treated with blebbistatin, the mesodermal labels tracked with their endodermal counterparts. Only after wash-out did the two overlapping labels separate.

This resumption of normal development and contractility indicates that the foregut and heart defects observed during prolonged treatment with blebbistatin are likely not the result of irreversible toxicity or rampant cell death. These results support

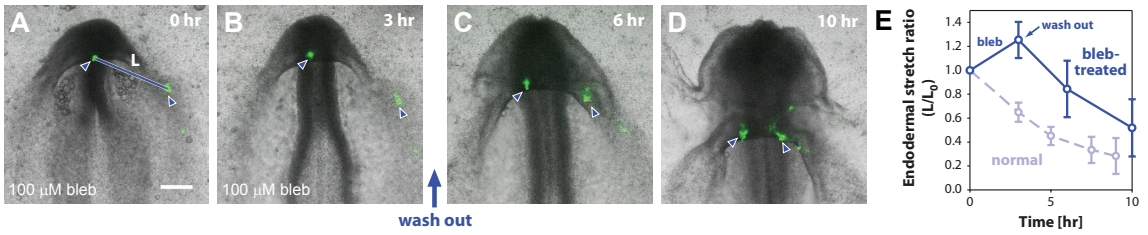

Figure 5.4: **Myosin-II dependent contraction drives endodermal shortening around AIP. (A,B)** Fluorescent labels were injected into the endoderm at medial and lateral locations around the AIP (blue arrowheads); these labels were separated by a distance L. Representative embryo cultured in 100 mM blebbistatin after (A) 0 hr and (B) 3 hr of incubation. At 3 hr of incubation, blebbistatin was washed out and culture was resumed. **(C,D)** Same embryo after 6 hr and 10 hr of total incubation. **(E)** Plots of the endodermal stretch ratio around the AIP as a function of time for both blebbistatin-treated (solid line, n=4) and normal (dashed line, n=5) embryos. The distance between endodermal labels at 0 hr (L_0) is used as the reference length. Error bars indicate ± SD. The dashed curve is identical to that shown in Fig. 5.2F. These results suggest that cytoskeletal contraction drives endodermal shortening around the AIP. Scale bar = 200 μm.

our hypothesis that actomyosin contraction drives endodermal shortening around the AIP.

Still, additional experiments were used to further confirm the presence of contraction. Because actively contracting tissues stiffen, we performed microindentation tests in embryos before and after blebbistatin exposure (Fig. 5.5). We indented medial, mediolateral, and lateral locations around the AIP in normal HH stage 8 embryos and calculated force-displacement (FD) curves for each location to locally measure tissue stiffness (i.e., endoderm, mesoderm, and the accompanying extracellular matrix taken together) (Fig. 5.5A,B). These curves were nonlinear, so the tissue stiffness (i.e., the tangential slope of each FD curve) depended on indentation depth. We therefore fit an exponential regression curve to each set of experimental FD data, and calculated the (tangential) tissue stiffness at 10 μm to characterize the local tissue response (Fig. 5.5B,E). In control embryos, stiffness around the AIP decreased with distance from the midline (Fig. 5.5E, solid bars).

Contraction was then suppressed by incubating each embryo in 100 μM blebbistatin at room temperature for ∼1–2 hr, and the microindentation experiments were repeated. Tissue stiffness decreased at each location after incubation with blebbistatin (Fig. 5.5E, compare Figs 5B and C). Although this result suggests that blebbistatin

had suppressed active contraction in the AIP, changes in stiffness can be caused by either changes in geometry or changes in material properties. Thus, to rule out the possibility that the observed changes in stiffness were simply the result of morphological differences after contraction had been suppressed, we used OCT to image HH stage 8 embryos before and after treatment in blebbistatin (Fig. 5.5D). Optical sections of the tissue at each indentation location revealed only minor changes in geometry after incubation in blebbistatin, confirming that the observed decreases in stiffness were likely caused by changes in the local, contractile state of the tissue. Somewhat suprisingly, however, a stiffness gradient around the AIP was still present after incubation in blebbistatin (Fig. 5.5E).

5.3.3 Endoderm (not mesoderm) is the primary contractile tissue layer

Active contraction tangential to the AIP would tend to generate tension in that direction. To estimate the mechanical stress in the tissue, we made a small linear incision at the medial point of the AIP. In normal embryos, the resulting wounds immediately opened (with a mean opening angle of $59^\circ \pm 3^\circ$), indicating a state of tension (Fig. 5.6A-C). Measuring the immediate tissue behavior precluded the possibility that an active healing response had affected our results. When similar cuts were made in embryos after treatment in blebbistatin for $\sim$1 hr, the wounds still opened but to a significantly lesser extent (with a mean opening angle of $33 \pm 3^\circ$) (Fig. 5.6D-F). These results indicate that the observed tension tangential to the AIP is at least partly due to actomyosin contraction.

To determine whether the mesoderm or endoderm is the dominant contractile tissue layer during this process, we constructed a 2D nonlinear finite element model of both germ layers around the AIP (see section 5.2.2 for details). Briefly, we consider an idealized 2D representation of the tissue (Fig. 5.1). In this 2D slice, the endoderm and mesoderm are modeled as concentric circular rings of pseudoelastic material (Fig. 5.1D); the AIP corresponds to the inner curvature of the rings. We also specify a polar coordinate system (r, θ) such that the r- and θ-directions run parallel and perpendicular, respectively, to the radii of the rings.

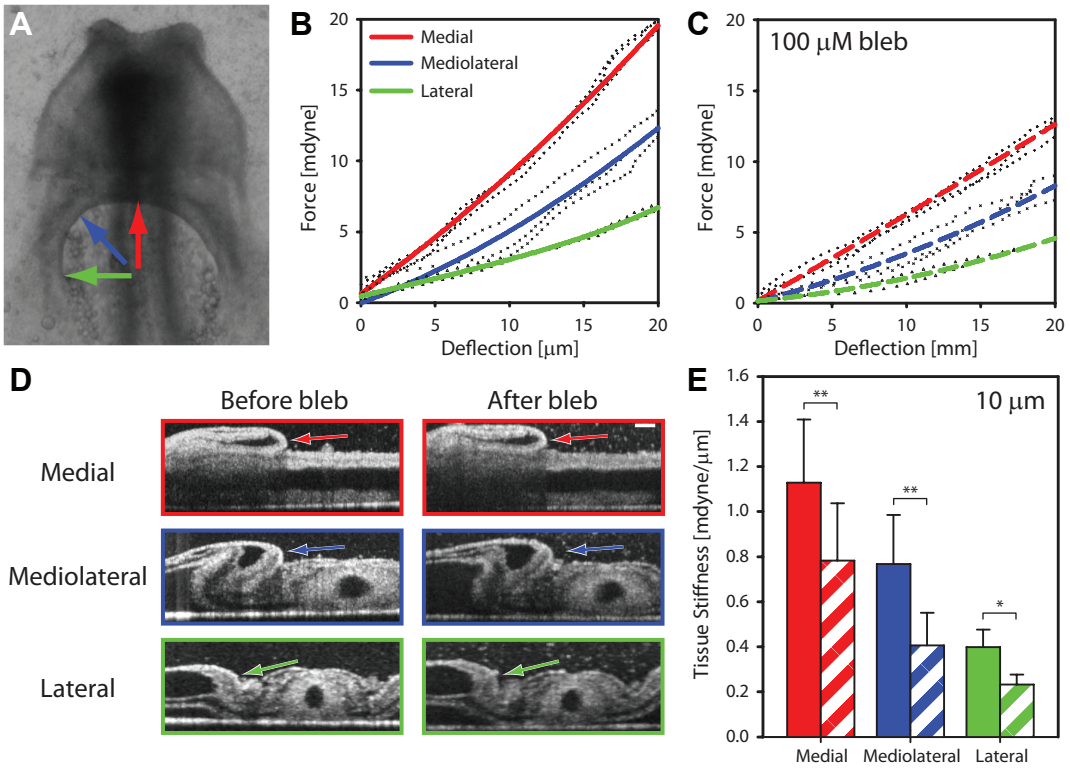

Figure 5.5: **Microindentation tests indicate active cytoskeletal contraction around AIP. (A)** Microindentation tests were performed at medial (red), mediolateral (blue), and lateral (green) locations around the AIP in HH stage 8+ embryos before and after incubation in 100 μM blebbistatin. Arrows indicate indentation locations. **(B,C)** Force-displacement curves for a representative embryo (B) before and (C) after treatment in blebbistatin. **(D)** Representative OCT sections of tissue geometry at each indentation location both before and after treatment with blebbistatin. Arrows indicate position of the indenter. Scale bar = 100 μm. **(E)** Plot of tissue stiffness at 10 μm displacement before (filled bars) and after (hatched bars) blebbistatin exposure. *, $P < 0.05$ and **, $P < 0.01$ (paired t-test, n=4). Tissue stiffness decreased at each tissue location after incubation in blebbistatin. Because actively contracting tissues stiffen, these results further suggest the presence of actomyosin contraction around the AIP.

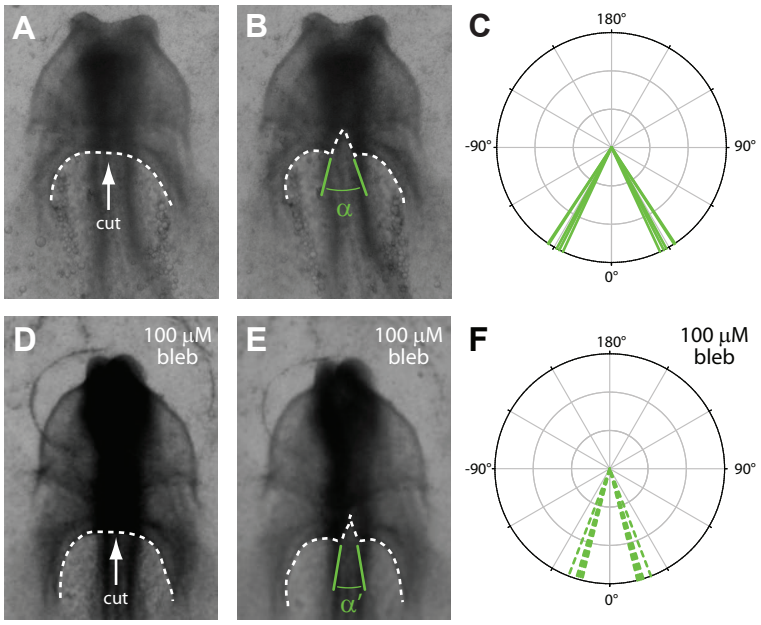

Figure 5.6: **Tension around AIP decreases when contraction is suppressed. (A-C)** Small linear incisions were made at the medial point of the AIP in normal HH stage 8 embryos (n=5). Dashed white lines indicate the contour of the AIP (A) before and (B) after cutting. Opening of wound indicates tension along AIP. (C) Resulting wound geometry was characterized by the opening angle $\alpha = 59° \pm 3°$. **(D-F)** Similar incisions were made in HH stage 8 embryos after incubation in 100 μM blebbistatin (n=4). Dashed white lines indicate the contour of AIP (D) before and (E) after cutting. (F) Wound geometry was characterized by the opening angle $\alpha' = 33° \pm 3°$. Wounds opened to a significantly lesser extent than in control embryos ($P < 0.001$, two-sample Watson-Williams test), indicating a reduction in tissue tension after blebbistatin exposure.

Active contraction is specified in the model only along the θ-direction (i.e., by assigning $G_\theta < 1$ with $G_r = 1$), since we observed endodermal shortening tangential to the AIP (Fig. 5.2). Our cutting experiments are then simulated by modifying the boundary conditions along the midline (i.e., switching a portion from roller to free) to create a linear incision at the medial point of the AIP (dotted lines in Fig. 5.7C,G). Contraction was specified in either the endoderm, mesoderm, or both layers, and the simulated wound geometry was compared to that observed experimentally.

During our cutting experiments, the contour of the AIP curled posteriorly and increased in curvature in the neighborhood of the cut (compare Figs 5.7A,A$'$). In our model, when we specify contraction in the endoderm only and simulate an incision at the midline (Fig. 5.7B-D), the cut opens as observed experimentally. In addition, the model AIP curls posteriorly and qualitatively matches the deformed contour of the AIP in our cutting experiments (compare white contour inside dashed red box in Fig. 5.7A$'$ with Fig. 5.7D). The model, however, does not capture the nearly straight wound edges observed experimentally. When contraction is simulated in the mesoderm only, the model wound fails to open, and the shape of the AIP does not match that seen in experiments (Fig. 5.7F-H).

Both of these models have the same overall shape before cutting is simulated. These contrasting results are therefore due to differences in stress across the tissue. When the endoderm contracts, the circumferential stresses (in the θ-direction) are compressive in the mesoderm and tensile in the endoderm (Fig. 5.7E). If the mesoderm contracts, however, the trend is reversed — the endoderm is in compression while the mesoderm is in tension (Fig. 5.7I). In this second case, compressive stresses in the endoderm drive wound closure.

These two models can be considered paradigmatic cases since all of the contraction is specified in either one germ layer or the other. Intermediate models, which include different ratios of contractility between the two layers, yield intermediate wound geometries between those shown in Figs 5.7D and H (Fig. 5.8).

Taken together, these results suggest that, during heart tube formation, the endoderm is the dominant contractile tissue layer. This contraction generates tension in the endoderm, which pulls the cardiogenic mesoderm toward the midline.

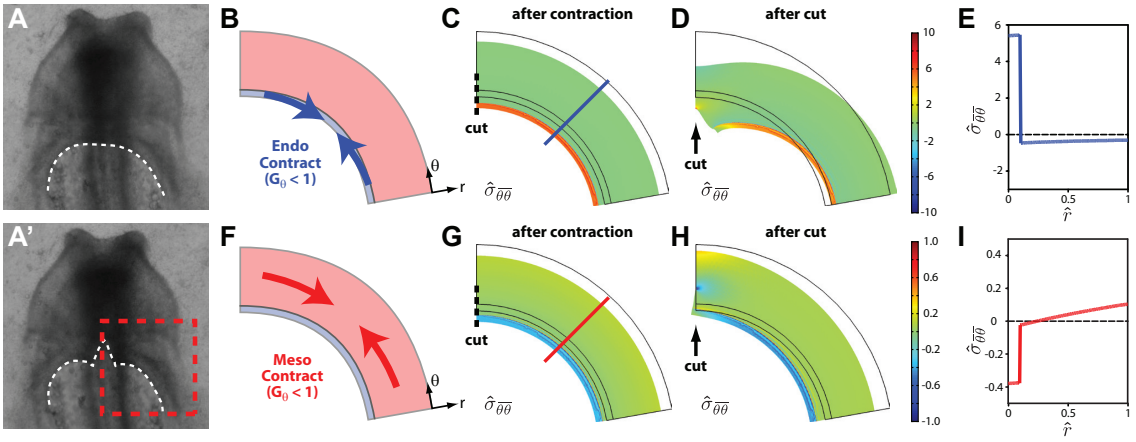

Figure 5.7: **Computational model indicates endoderm as primary contractile tissue layer. (A,A)** Deformed shape of the AIP (A) before and (A) after cutting (same as Figure 6A,B). **(B-D)** When (B) contraction is specified in the endoderm only and (C) an incision is simulated at the midline, (D) the cut opens as observed experimentally. The model AIP curls posteriorly and qualitatively matches the deformed contour of the AIP in our cutting experiments (compare white contour inside dashed red box in (A) with geometry in (D)). **(E)** When the endoderm contracts, the (convected) circumferential Cauchy stresses are compressive in the mesoderm and tensile in the endoderm (computed along blue line in (C)). **(F-H)** When (F) contraction is simulated in the mesoderm only, (G) the model cut (H) fails to open up, and the shape of the AIP is not curled posteriorly as in experiments. **(I)** In this case, the endoderm is in compression while the mesoderm is in tension (computed along red line in (G)). Agreement between the experiments and model in (D), but not in (H), indicates that the endoderm (not the mesoderm) is the primary contractile tissue layer. $\hat{r}$ is the normalized radial distance across the rings, where 0 represents the inner curvature. AIP = anterior intestinal portal.

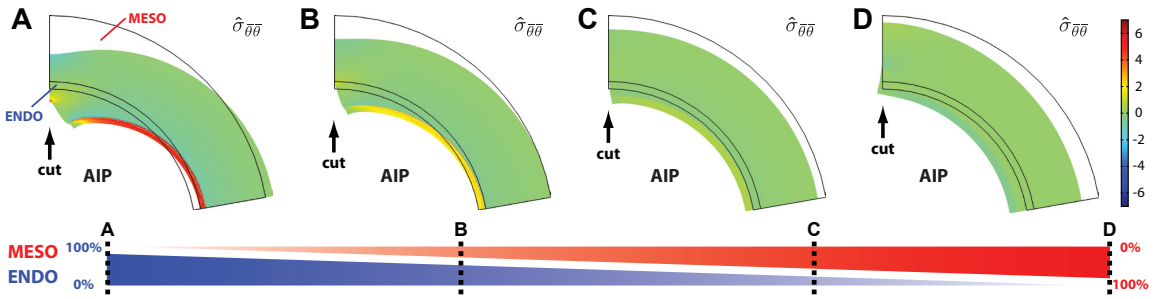

Figure 5.8: **Varying ratio of contractility between model endoderm and mesoderm.** Cytoskeletal contraction is simulated in the model by specifying values for the circumferential contraction ratio G_θ. If contraction is specified (A) in the endoderm only (where $G_{\theta,E} = 0.6$), the simulated cut opens and the contour of the AIP curls posteriorly. If contraction, however, is specified (D) in the mesoderm only (where $G_{\theta,M} = 0.92$), the model wound fails to open. In this case, the contraction ratio $G_{\theta,M}$ is specified so that model has an equivalent global geometry to that in (A) before cutting is simulated. When different ratios of contractility are specified between the two germ layers (e.g., 67% $G_{\theta,E}$ and 33% $G_{\theta,M}$ in (B), 33% $G_{\theta,E}$ and 67% $G_{\theta,M}$ in (C)), the models produce intermediate wound geometries between those in the paradigmatic cases of (A) and (D). Here, 100% $G_{\theta,E} = 0.6$; 0% $G_{\theta,E} = 1$; 100% $G_{\theta,M} = 0.92$; and 0% $G_{\theta,M} = 1$. Plots of the normalized convected Cauchy stress $\hat{\sigma}_{\bar{\theta}\bar{\theta}}$ show the endoderm progressively changes from a state of tension in (A) to compression in (D). AIP = anterior intestinal portal.

5.4 Discussion

Morphogenesis is fundamentally a physical process, as mechanical forces deform developing tissues in a coordinated way to create biological form (Taber, 1995; Lecuit and Lenne, 2007; Gjorevski and Nelson, 2010b; Davidson, 2011). In recent years, groups of developmental biologists, physicists and engineers have been paying renewed attention to the mechanics of morphogenesis — how forces are generated in the embryo (Hutson et al., 2003; Rauzi et al., 2008; Martin et al., 2009; Martin, 2010; Wozniak and Chen, 2009), how those forces are integrated into tissue-level deformations (Ramasubramanian et al., 2006; Chen and Brodland, 2008; Martin et al., 2010; Varner et al., 2010; Brodland et al., 2010), and how they might regulate both cytoskeletal dynamics (Bertet et al., 2004; Fernandez-Gonzalez et al., 2009; Pouille et al., 2009; Zhou et al., 2010; Filas et al., 2011) and regional gene expression (Farge, 2003; Desprat et al., 2008). Here, we have characterized some of the mechanical forces that drive heart tube assembly in the avian embryo.

5.4.1 Physical forces that shape the heart tube are poorly understood

Much work has been done to map the regions of the embryo that are destined to form the heart (Rawles, 1943; Stalsberg and DeHaan, 1969; Redkar et al., 2001; Cui et al., 2009), and many of the important genetic and molecular factors that drive cardiac specification and differentiation have been identified (Olson and Srivastava, 1996; Yutzey and Kirby, 2002; Buckingham et al., 2005; Abu-Issa and Kirby, 2007). The mechanical forces that physically drive formation of the primitive heart tube, however, remain relatively uncharacterized (Taber, 2006).

Still, several investigators have speculated that a combination of forces likely drives heart tube assembly (Stalsberg and DeHaan, 1969; Linask and Lash, 1986; Drake and Jacobson, 1988; Meilhac and Buckingham, 2010). In particular, the mechanism by which the bilateral fields of cardiogenic mesoderm move toward the midline and fuse to form the heart tube has garnered the most experimental attention. Early evidence in avian embryos suggested that this convergence is driven largely by active crawling of the mesoderm over the underlying endoderm (DeHaan, 1963; Linask and Lash, 1986, 1988a,b), and the possibility that other physical mechanisms also might contribute to this process for the most part faded from view. A notable exception, however, is the study by Wiens (1996), who speculated that cytoskeletal contraction within the mesoderm itself might drive its convergence toward the midline. Our results support this contraction idea, but suggest that the source of contraction is the endoderm rather than the mesoderm.

5.4.2 Endoderm has generally been considered an inductive substrate

Mounting evidence has established a clear signaling role for the endoderm during early cardiogenesis (Nascone and Mercola, 1996; Lough and Sugi, 2000; Brand, 2003). Removal of (or defects in) the endoderm can produce abnormal heart development (Orts-Llorca, 1963; Rosenquist, 1970), and the endoderm is necessary for the initiation and maintenance of several cardiac transcription factors (Alsan and Schultheiss,

2002). Others have shown, however, that explants of cardiogenic mesoderm removed post-gastrulation are still capable of expressing a host of cardiac-specific genes in the absence of endoderm (Gannon and Bader, 1995; Du et al., 2003). Even so, the endoderm is at least transiently required to generate beating heart tissue (Gannon and Bader, 1995). Furthermore, mesoderm not fated to contribute to the heart can be induced to express cardiac marker genes by co-culture with endoderm normally adjacent to the cardiogenic mesoderm (Schultheiss et al., 1995). This endoderm expresses the cardiac inducing factors BMP-2 (Schultheiss et al., 1997; Andrée et al., 1998) and FGF-8 (Alsan and Schultheiss, 2002), as well as the Frizzled-related protein Crescent (Marvin et al., 2001), which inhibits Wnt signaling – an antagonizer of cardiogenesis.

Such evidence has contributed to the generally accepted view that the role of the endoderm during heart tube formation is to serve as an inductive substrate for the actively crawling mesoderm, secreting various growth factors that induce cardiac specification and differentiation in the mesoderm as it migrates past.

5.4.3 Endoderm actively contracts to pull cardiogenic mesoderm toward midline

In the present study, we have used a combination of computational modeling and ex ovo experiments with chick embryos to show that the endoderm also plays a crucial mechanical role during cardiogenesis. Our results suggest that the endoderm around the AIP actively contracts and pulls the bilateral fields of cardiogenic mesoderm toward the midline, enabling them to properly fuse and form the heart tube.

Dynamically tracking the motions of the mesoderm and endoderm during heart tube assembly revealed that both layers move toward the midline together (Fig. 5.2). Although relative movement between the two germ layers was observed (Fig. 5.2E), possibly reflecting active migration, its contribution to the overall convergence of the cardiogenic mesoderm was relatively minor. The motions of the endodermal labels in these experiments are consistent with the pioneering work of Rosenquist (1966) and Stalsberg and DeHaan (1968), who used tritiated thymidine labeling and iron oxide particles, respectively, to track endodermal displacements. Although both of these studies reported endodermal shortening around the AIP, neither dynamically

measured the concomitant motion of the cardiogenic mesoderm or investigated the mechanical stresses present in the tissue. Even so, Stalsberg and DeHaan (1968) proposed a simple mechanical model for foregut morphogenesis, contending that the posterior descent of the AIP is driven by tension around the AIP — a tension that is generated by elongation of the notochord and regression of Henson's node.

Here, however, we have shown that myosin-II based cytoskeletal contraction drives both endodermal shortening and AIP descension, and that inhibiting this contraction with blebbistatin can lead to cardia bifida and abnormal foregut morphogenesis (Fig. 5.3). Notably, both elongation of the notochord and regression of Henson's node occur relatively normally in these embryos even with the observed heart and foregut defects. We therefore suggest an alternative mechanism to that of Stalsberg and DeHaan (1968). Rather than deformations caused by forces at a distance (i.e., notochordal elongation, etc.), local contraction around the AIP itself drives endodermal shortening and thereby both AIP descension and heart field convergence.

Wei et al. (2001) have reported cardia bifida in chick embryos treated with the Rho kinase inhibitor Y27632, which also suppresses cytoskeletal contraction. They concluded, however, that the observed heart and foregut defects were not due to a lack of contractility, since treatment with the myosin light chain kinase (MLCK) inhibitor ML-9 did not reproduce the observed abnormalities. Previous work in our laboratory, however, has shown that the similar but more specific MLCK inhibitor ML-7 (Bain et al., 2003) did not significantly reduce either myosin regulatory light chain phosphorylation or tissue stiffness in looping chick hearts (Rémond et al., 2006). It is thus possible that ML-9 did not completely suppress cytoskeletal contraction, and that cardia bifida produced by treatment with Y27632 was (at least in part) due to attenuated contraction.

To determine whether the cardiogenic mesoderm or the adjacent endoderm is the dominant contractile layer during heart tube assembly, we constructed a 2D computational model of both germ layers around the AIP (Fig. 5.1). When a linear incision is simulated at the midline, the deformed shape of the AIP matches our cutting experiments only if contraction is included (predominantly) in the endoderm (Fig. 5.7). The model predicts endodermal tension and mesodermal compression — a result

consistent with previous work in our laboratory which reported mesodermal compression in the fusing omphalomesenteric veins of HH stage 10 chick hearts (Voronov et al., 2004). Furthermore, preliminary data from our laboratory has estimated a small-strain shear modulus of 50–100 Pa for the tissue around the AIP (V.D.V., unpublished). Our model thus predicts peak stresses in the contracting endoderm that are between 300–600 Pa, which are on the order of the contractile stresses generated within a coherent and collectively migrating cell sheet (Trepat et al., 2009). We suggest therefore that active contraction around the AIP is primarily endodermal in origin, not mesodermal as postulated by Wiens (1996).

Taken together, these results suggest an essential mechanical role for the endoderm during heart tube assembly (Fig. 5.9). Instead of just serving as a passive, secretory substrate for the crawling cardiogenic mesoderm (Fig. 5.9C), the endoderm around the AIP actively contracts and pulls (i.e., convects) the heart fields toward the midline (Fig. 5.9D), enabling them to fuse and form the heart tube. How this contraction is spatially distributed, and how this distribution may contribute to the observed morphogenetic movements remain open questions. In particular, it would be interesting to determine whether the observed stiffness gradient around the AIP (Fig. 5.5E) is due to spatial variations in tissue geometry, mechanical properties, actomyosin contractility, or the amount of cross-linking within the extracellular matrix (ECM).

Other recent studies of avian embryogenesis have shown that cell displacements are similarly convected by ECM (i.e., substrate) motion during the processes of primitive streak formation (Zamir et al., 2008), gastrulation (Zamir et al., 2006), and axial elongation (Bénazéraf et al., 2010). The interface between the cardiogenic mesoderm and adjacent endoderm is textured with an abundant ECM containing fibronectin, laminin, and collagen types I and IV (Linask and Lash, 1986; Drake et al., 1990; Wiens, 1996). The two tissue layers are thus intimately coupled, with numerous interdigitating cell processes extending through the layer of ECM (Linask and Lash, 1986). Contractile forces generated in the endoderm could thus be plausibly transmitted to the overlying mesoderm, and we speculate that ECM deforms with the contracting endoderm.

Both our label tracking experiments and model, however, are limited to two dimensions and fail to accurately capture the out-of-plane folding that both tissue layers

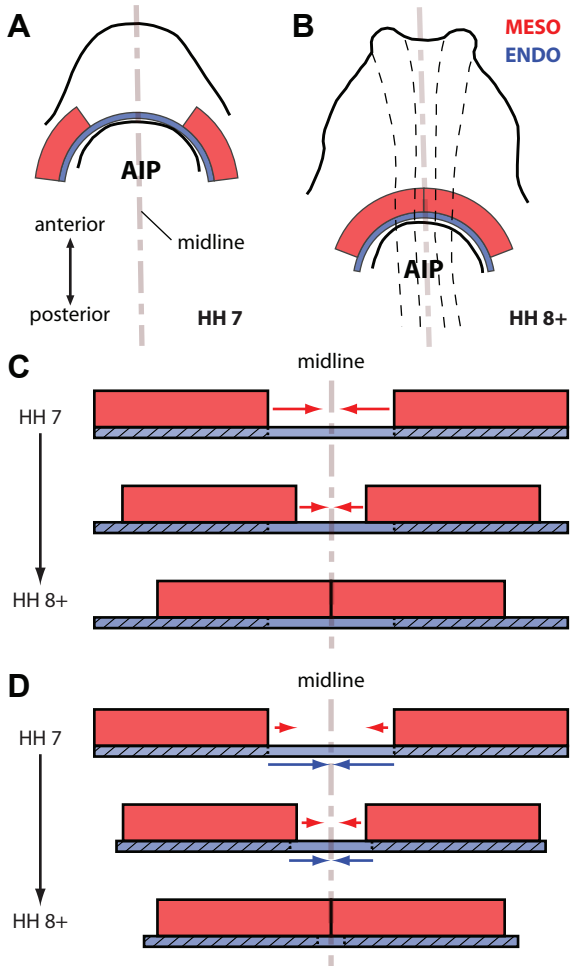

Figure 5.9: **Endoderm actively contracts to pull the cardiogenic mesoderm toward the midline. (A)** Schematic of HH stage 7 embryo. The cardiogenic mesoderm (red) is organized as a pair of bilateral epithelia that are separated on either side of the embryonic midline and remain in close contact with the underlying endoderm (blue). **(B)** Schematic of HH stage 8+ embryo. As the AIP descends, the cardiogenic mesoderm moves toward the midline and fuses to begin forming the early heart tube. **(C)** Investigators have suggested that the endoderm primarily serves as an inductive substrate for the actively crawling mesoderm (red arrows). **(D)** Our results suggest that the endoderm also has a distinct mechanical role in early cardiogenesis — it actively contracts (blue arrows) to pull the cardiogenic mesoderm toward the midline. Although relative motion (red arrows) occurs between the endoderm and mesoderm during this process (likely due to collective migration), this motion is much less than the convection caused by contraction. AIP = anterior intestinal portal.

undergo during this process. Although our results offer qualitative insight into the mechanics of heart tube formation, further experimental and computational work is needed to more fully characterize the 3D nature of this problem. Imaging technologies such as OCT (Filas et al., 2007) or dynamic wide-field fluorescence imaging (Zamir et al., 2006, 2008; Sato et al., 2010) are sure to prove useful tools in this regard.

It also remains to be seen whether endodermal contraction around the AIP proceeds in the pulsatile, ratchet-like manner described during both Drosophila ventral furrow formation (Martin et al., 2009) and dorsal closure (Solon et al., 2009). The endoderm shortens so dramatically ($> 60\%$) as the AIP descends (Fig. 5.2F) that it seems reasonable that the contracting cytoskeleton may need to stabilize or remodel at intermediate configurations (akin to airway smooth muscle cells) to accomplish an active shortening of this magnitude (Fredberg et al., 1997). These stabilized configurations could explain the observed residual tension in the AIP after treatment in blebbistatin (Fig. 5.6D-F). Remodeling of the ECM between the endoderm and mesoderm might also contribute to such stabilizations.

In addition, it remains a possibility that, once they have moved to the midline, the fusing cardiogenic mesoderm may (much like a zipper) provide a driving force behind AIP descension (Moreno-Rodriguez et al., 2006). Recent work, however, has shown that ectopic expression of Wnt3a can generate a cardia bifida phenotype without any apparent defects in AIP descension or foregut morphogenesis (Yue et al., 2008). Moreover, since the AIP begins its descent well before there is any mesoderm at the midline, we speculate that even after heart field fusion, contraction continues to drive the posterior descent of the AIP.

5.4.4 Role for endodermal contractility in cardia bifida mutants?

Several gene mutants produce a cardia bifida phenotype (Meilhac and Buckingham, 2010), and it is unclear whether any are due to suppressed levels of endodermal contractility. An intriguing possibility is the $Gata4^{-/-}$ mouse mutant, which has both cardia bifida and abnormal foregut morphogenesis (Kuo et al., 1997; Molkentin et al., 1997). GATA-4 is normally expressed in both the cardiogenic mesoderm and adjacent

endoderm. In the intriguing mosaic experiments of Narita et al. (1997), however, wild-type ($Gata4^{+/+}$) endoderm alone was sufficient to rescue both the cardia bifida and abnormal foregut phenotype in embryos that otherwise consisted only of $Gata4^{-/-}$ cells. GATA-4 thus seems to be required in the endoderm, not the mesoderm, for proper heart tube assembly (Narita et al., 1997; Watt et al., 2004). Since GATA-4 has also been shown to regulate the expression of cytoskeletal proteins (Molkentin et al., 1994), it may be involved in contractility and (consequently) endodermal shortening around the AIP. It would be interesting to investigate the role of actomyosin contractility in the these mutants.

In zebrafish, other types of genetic perturbations produce both endodermal defects and cardia bifida, such as *one-eyed pinhead* (Schier et al., 1997) and *casanova* (Alexander et al., 1999). Intuiting a possible physical role for the endoderm here, however, is decidedly more problematic, since it seems to play a somewhat different role. Several recent studies have suggested that heart field convergence in zebrafish is in fact largely driven by active crawling of cardiomyocytes toward the midline (Holtzman et al., 2007), a process likely regulated by fibronectin (Trinh and Stainier, 2004; Garavito-Aguilar et al., 2010). How deformations in the endoderm may contribute to this process remains unclear. Other recent work in ascidian embryos, however, has suggested a possible morphogenetic role for the endoderm during heart progenitor convergence (Ragkousi et al., 2011).

In conclusion, we propose an active mechanical role for the endoderm during heart tube formation. This work constitutes a new step toward characterizing some of the mechanical forces that shape the vertebrate heart. How these forces are regulated by (or in turn regulate) the various molecular and genetic factors involved in cardiogenesis remains an exciting avenue of research to explore, as we seek to connect genetic and molecular mechanisms of development with the mechanics of morphogenesis.

Chapter 6

On tissue stiffness and contractility gradients during heart tube formation

6.1 Introduction

The heart is the first mechanically functioning organ to form in the embryo. Similar to other organ primordia (Lubarsky and Krasnow, 2003), the embryonic heart forms as a simple tube — in this case, a straight muscle-wrapped tube situated along the ventral side of the embryo (Stalsberg and DeHaan, 1969; Taber, 2006; Abu-Issa and Kirby, 2007).

Given that avian heart development parallels that in humans (DeHaan, 1967), the chick embryo is well suited to studies of early cardiogenesis. During gastrulation, when the primary germ layers (endoderm, mesoderm, and ectoderm) are established, the early chick embryo is organized as a flat sheet of cells. The cardiac progenitors reside in the lateral plate mesoderm, where they form a pair of epithelia situated on either side of the embryonic midline (Stalsberg and DeHaan, 1969; Abu-Issa and Kirby, 2008). After the head fold has formed, the initial planar geometry of the embryo is broken and the cardiogenic mesoderm folds out-of-plane and moves toward the embryonic midline. Then, in one of the most dramatic events during early amniote development, the bilateral fields of cardiac progenitors fuse behind the anterior intestinal portal (AIP) to form the primitive heart tube (Moreno-Rodriguez et al., 2006; Cui et al., 2009). During this entire process, the mesoderm remains in close

contact with the underlying endoderm (Linask and Lash, 1986; Schultheiss et al., 1995).

In Chapter 5, we showed that in addition to its inductive signaling role, the endoderm around the AIP actively contracts and pulls the fields of cardiogenic mesoderm toward the midline, enabling them to form the heart tube. How this contraction is spatially distributed, and how different distributions of contraction might affect the morphogenetic deformations around the AIP, however, are still open questions. Moreover, whether the measured stiffness gradient around the AIP, which decreases with distance from the midline, is due to variations in material properties, contractility, or differences in geometry still remains unresolved.

Here, we employ a growth theory for beams and use it to qualitatively investigate the effects of spatial gradients in contractility and material properties around the AIP. Considered in combination with label tracking and tissue cutting experiments using whole chick embryos, these models suggest that the distribution of contraction around the AIP is relatively uniform.

Moreover, microindentation experiments indicate that, even when contraction is broadly suppressed using the myosin II inhibitor blebbistatin, a stiffness gradient is still present around the AIP. Finite element simulations of these experiments suggest that this residual stiffness gradient is caused by a spatial gradient in the passive mechanical properties of the tissue, as opposed to local differences in tissue geometry.

These results offer insight into how embryonic tissues are spatially patterned during the process of heart tube formation, and raise new questions about the cellular mechanisms and signaling networks that drive this morphogenetic event. This work highlights how variations in both contractility and mechanical properties can alter the deformations observed during development, and our methods can be readily generalized to different morphogenetic processes.

6.2 Experimental methods

6.2.1 Whole embryo harvesting and dissection

Fertilized White Leghorn chicken eggs were incubated in a humidified, forced draft incubator at 38°C for 28 to 34 hours to yield embryos between Hamburger and Hamilton (HH) stages 7 and 8 (Hamburger and Hamilton, 1951). Whole embryos were harvested using a filter paper carrier method (Voronov and Taber, 2002), thus preserving the mechanical stresses present in the tissue. Each embryo was soaked in a bath of phosphate buffered saline (PBS) at room temperature to remove any adherent yolk particles, and was then placed ventral side up in a 35 mm culture dish. The entire embryo/filter paper assembly was then submerged under a thin layer of PBS.

6.2.2 Tissue cutting experiments

To qualitatively measure tissue stress, small linear incisions were made at different locations around the AIP using the Gastromaster microsurgical device (Xenotek Engineering) with white tips. These experiments were performed at room temperature with a group of normal HH stage 8 embryos in PBS (n=5). The extent of wound opening was quantified using ImageJ. A line segment was fit to each wound edge, and the angle between the lines was measured using the Angle Tool.

6.2.3 Optical coherence tomography

A Thorlabs (Newton, NJ) optical coherence tomography (OCT) system with attached Nikon FN1 microscope was used to obtain cross-sectional image stacks of living HH stage 8 embryos (n=2). Image slices were acquired every 5 μm across a 3 x 3 mm scanning window and then reconstructed into 3D volumes using Volocity (PerkinElmer, Waltham, MA).

As described below, optical sections through different regions of the AIP were used to create the tissue geometry used in finite element simulations of our microindentation experiments.

6.2.4 Microindentation

Normal HH stage 8 embryos (n=5) were transferred (individually) to a large bath of PBS at room temperature. Using a custom-built microindentation device (Zamir et al., 2003), tissue stiffness was measured at different locations around the AIP. As described previously, we used a microindenter, attached to a calibrated cantilever beam, to calculate local force-deflection (FD) curves for the tissue (Zamir et al., 2003; Nerurkar et al., 2006; Ramasubramanian et al., 2008; Filas et al., 2011). Three consecutive indentations were made to ensure a repeatable response. The tangential slope of the FD curve at 10 μm deflection was used as a local measure of tissue stiffness.

Each embryo was then transferred to a 35 mm culture dish and incubated in 100 μM (–)-blebbistatin in PBS for 1-2 hr at room temperature. Performing this incubation step at room temperature ensured that the embryo did not develop further during these experiments. Afterward, microindentation tests were repeated at each tissue location to measure any changes in tissue stiffness.

Using another group of HH stage 8 embryos (n=3), we performed microindentation tests using our OCT setup to visualize the tissue deformations near the indenter. Owing to spatial constraints, the entire microindentation setup used to make stiffness measurements could not be transferred to the OCT. Thus, using pulled glass micropipettes, we fashioned microindenters of similar (cylindrical) geometry and attached them to a hand-driven micromanipulator. The axis of the indenter was aligned with the OCT imaging plane. Driven manually, it could then be used to indent the tissue, while real-time OCT recordings were used to capture the resultant tissue deformations.

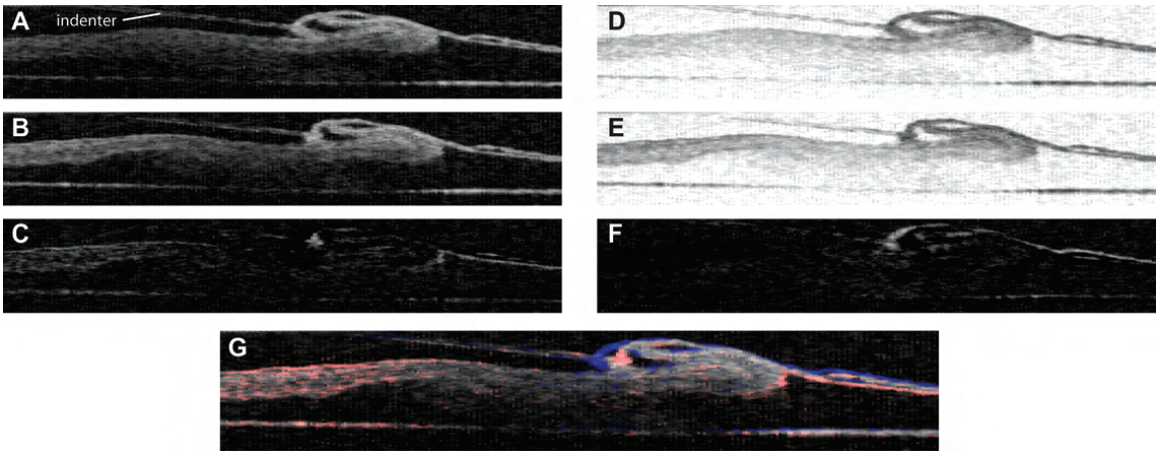

Figure 6.1: **Characterizing tissue deformations during microindentation using OCT. (A)** Sagittal (midline) OCT section through an HH stage 8 embryo. The long axis of the cylindrical indenter is aligned with the imaging plane, and has just come into contact with the tissue. **(B)** Subsequent OCT image showing deformed shape of the indented tissue. **(C)** Image created by subtracting (A) from (B). **(D,E)** Inverted images of (A) and (B). **(F)** Image created by subtracting (D) from (E). **(G)** Composite color image generated by overlaying (C) (red) and (F) (blue) on top of (A).

During these experiments, the indenter was not attached to a calibrated cantilever beam, so tissue stiffness was not measured. Instead, we were interested solely in the deformed shape of the tissue.

6.2.5 Image processing

Within each stack of real-time OCT images, the contact frame (i.e., the frame which captured the indenter first coming into contact with the tissue) was used as a reference (Fig. 6.1A). Then, using the Image Calculator in ImageJ, this reference frame was subtracted from subsequent images (e.g., Fig. 6.1B) in the recording, which showed the tissue as it deformed under the indenter. This operation identified populations of pixels which increased in intensity as the tissue deformed (Fig. 6.1C). These pixels represented regions where the deforming tissue had moved into space previously occupied by only fluid (i.e. the leading edge of the deformation).

In a similar way, repeating this operation using inverted OCT images (Fig. 6.1D-E) identified pixels that decreased in intensity (Fig. 6.1F). That is, regions in space where tissue had been replaced by fluid (i.e., the trailing edge of the deformation).

Both subtracted images were then overlaid on top of the originals to generate composite (color) images, which indicated both the leading (red) and trailing (blue) edges of the tissue deformation during microindentation (Fig. 6.1G).

6.2.6 Fluorescent labeling and tracking

To quantify endodermal deformations around the AIP during heart tube formation, we tracked the motion of fluorescently labels cells during ex ovo culture. As described in Chapter 4, we soaked iron particles in saturated DiI in ethanol and distributed them across the tissue. After a brief incubation at 38°C, the particles were removed with a strong magnet, leaving fluorescently labeled cells behind.

Each embryo (n=3) was then submerged beneath a thin layer of liquid culture media and incubated at 38°C in 95% O_2 and 5% CO_2 (Voronov and Taber, 2002). Bright field and fluorescence time-lapse images were captured at approximately 1–2 hr intervals using a Leica DMLB microscope and attached video camera (Retiga 1300). The motion of individual labels was then tracked using the Manual Tracking plug-in in ImageJ.

6.2.7 Statistics

All data are reported as mean ± SD. To compare regional stiffness data around the AIP, we used a one-way ANOVA with the Tukey post hoc test implemented in SigmaPlot (Systat Software Inc., Chicago, IL). Circular statistics and a two-sample Watson-Williams test were used to analyze and compare wound opening angles (Zar, 2010).

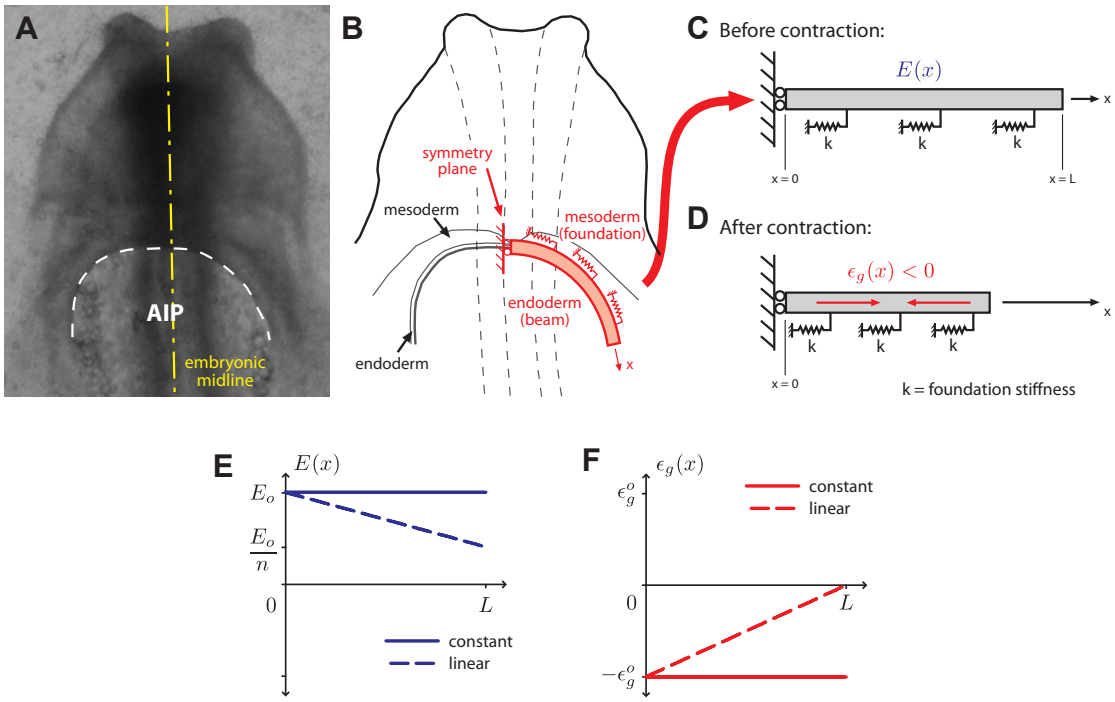

Figure 6.2: **Modeling the tissue around the AIP as a contractile beam on an elastic foundation. (A)** Bright field image of a HH stage 8 embryo. **(B)** Schematic of embryo shown in (A). The endoderm around the AIP is modeled as a contractile beam, and the mesoderm as an elastic foundation. Symmetry is assumed about the embryonic midline. **(C,D)** (C) Undeformed and (D) deformed model geometry after contraction. **(E)** The Young's modulus $E(x)$ is taken to be either uniform (solid line) or linearly decreasing along the beam (dashed line). **(F)** Similarly, active contraction in the beam ($\epsilon_g(x) < 0$) is taken as either uniform (solid line) or linearly decreasing (dashed line).

6.3 Theoretical methods

6.3.1 Contracting beam on elastic foundation

As a first approximation, we model the endoderm and mesoderm around the AIP by considering the relatively simple problem of a contractile beam on an elastic foundation (Fig. 6.2). In Chapter 5, we presented evidence suggesting that the endoderm (not the mesoderm) is the primary contractile tissue layer during heart tube formation. The contractile beam thus represents the endoderm, and the mesoderm is modeled as an elastic foundation represented by a series of springs.

Here, we employ a linear growth theory for beams, since our model is used to qualitatively investigate the mechanical behavior of the tissue. Admittedly, the deformations involved in heart tube assembly are large (or finite), and to quantitatively characterize the stresses that resident cells in the tissue experience, the fully nonlinear theory must be brought to bear. But, when used as a first approximation, the linear theory can still offer real qualitative insight into the behavior, and its relatively simpler mathematics enable us to (at times!) generate closed-form solutions to the problem.

We consider a thin beam of length L with uniform rectangular cross-section subjected to a combination of both axial forces and longitudinal growth. Growth is simulated in the beam by decomposing the total strain[8] $\epsilon = u'(x)$ into an elastic strain ϵ^* and growth strain ϵ_g by

$$\epsilon = \epsilon^* + \epsilon_g. \tag{6.1}$$

The stress σ in the beam is then a function of the elastic strain ϵ^* (as opposed to the total strain ϵ for a passive material). If we assume a Hookean constitutive response, this relation takes the form

$$\sigma = E\epsilon^* = E\left(\epsilon - \epsilon_g\right) \tag{6.2}$$

where E is the Young's modulus of the material.

Contraction is simulated by negative growth (i.e., $\epsilon_g < 0$), and deformation of the beam is resisted by an elastic foundation with stiffness k per unit volume of the bar.

Uniform contraction and uniform mechanical properties

For a uniformly contracting beam with uniform material properties (Fig. 6.2E,F), we take

$$\begin{array}{c} \epsilon_g\left(x\right) = -\epsilon_g^o \\ E\left(x\right) = E_o \end{array}, \tag{6.3}$$

and the governing equation for the axial elongation $u\left(x\right)$ of the beam is given by

$$u''(x) - \alpha^2 u'(x) = 0 \tag{6.4}$$

[8] $(\ )'$ denotes differentiation with respect to x.

where $\alpha = \sqrt{k/E}$. We assume symmetry about the embryonic midline, so the left end of the beam is held fixed while the right end remains traction-free. Thus, we take the boundary conditions

$$\begin{aligned} u(0) &= 0 \\ \sigma(L) = 0 \Longrightarrow \frac{du}{dx}(L) &= -\epsilon_g^o \end{aligned} . \tag{6.5}$$

Solving this equation in closed-form, we get

$$u(x) = -\frac{\epsilon_g^o}{\alpha \cosh(\alpha L)} \sinh(\alpha x), \tag{6.6}$$

which can be used to calculate both the stretch ratio

$$\lambda(x) = 1 + \epsilon(x) = 1 - \frac{\epsilon_g^o}{\cosh(\alpha L)} \cosh(\alpha x) \tag{6.7}$$

and the stress field

$$\bar{\sigma}(x) = \frac{\sigma(x)}{E_o} = \epsilon_g^o \left[1 - \frac{\cosh(\alpha x)}{\cosh(\alpha L)}\right]. \tag{6.8}$$

Gradient in contraction and uniform mechanical properties

If contraction in the beam, however, is not uniform, and we consider the linear contraction gradient (Fig. 6.2F)

$$\epsilon_g(x) = -\epsilon_g^o + \frac{\epsilon_g^o}{L} x, \tag{6.9}$$

as well as uniform Young's modulus

$$E(x) = E_o, \tag{6.10}$$

the governing equation takes the form

$$u''(x) - \alpha^2 u(x) = \frac{\epsilon_g^o}{L}. \tag{6.11}$$

Using the boundary conditions

$$\begin{aligned} u(0) &= 0 \\ \sigma(L) = 0 &\Longrightarrow u'(L) = 0 \end{aligned} \tag{6.12}$$

we can solve this equation in closed-form to yield

$$u(x) = \frac{E\epsilon_g^o}{kL}\left[\cosh(\alpha x) - \tanh(\alpha L)\sinh(\alpha x) - 1\right]. \tag{6.13}$$

In this case, the stretch ratio is given by

$$\lambda(x) = 1 + \frac{\alpha E\epsilon_g^o}{kL}\left[\sinh(\alpha x) - \tanh(\alpha L)\cosh(\alpha x)\right], \tag{6.14}$$

and the stress field by

$$\bar{\sigma}(x) = \frac{\alpha E\epsilon_g^o}{kL}\left[\sinh(\alpha x) - \tanh(\alpha L)\cosh(\alpha x)\right] - \epsilon_g^o\left(\frac{x}{L} - 1\right). \tag{6.15}$$

Uniform contraction and gradient in mechanical properties

Also, to assess the effects of a material property gradient, we consider the case of a uniformly contracting beam with a linearly varying Young's modulus (Fig. 6.2E,F):

$$\begin{aligned} \epsilon_g(x) &= -\epsilon_g^o \\ E(x) &= E_o\left(1 - \frac{1 - \frac{1}{n}}{L}\,x\right) \end{aligned} \tag{6.16}$$

where n is the fold decrease in modulus along the length L of the beam.

In this case, the governing equation is

$$u''(x) + \frac{E'(x)}{E(x)} \cdot u'(x) - \frac{k}{E(x)} \cdot u(x) = -\epsilon_g^o \frac{E'(x)}{E(x)}, \tag{6.17}$$

and we take the boundary conditions

$$\begin{array}{c} u(0) = 0 \\ \sigma(L) = 0 \Longrightarrow u'(L) = -\epsilon_g^o \end{array} . \tag{6.18}$$

We used the MATLAB subroutine *bvp4c* to solve Eqns. (6.17)–(6.18). For validation, we compared our numerical solution for the special case of $n = 1$ with our analytical solution for a uniformly contracting beam with uniform material properties (i.e., Eq. (6.6)).

6.3.2 Finite element model

Using COMSOL Multiphysics (Version 3.5, COMSOL AB, Providence, RI), we constructed a nonlinear, 3D finite element model of the tissue around the AIP to simulate our microindentation experiments. As shown below, we observed a stiffness gradient around the AIP, which decreased with distance from the embryonic midline. To investigate a possible role for differences in tissue geometry in the observed gradient, we used OCT section data from HH stage 8 embryos to construct our model geometry (Fig. 6.3). The largest difference in stiffness was observed between medial (red) and lateral (green) regions of the AIP (Fig. 6.3A). Thus, using Adobe Illustrator, we manually segmented the tissue geometry from OCT sections at these two locations (Fig. 6.3B,C), and imported each into COMSOL.

We created separate models for indentation of both the medial (Fig. 6.3D) and lateral AIP (Fig. 6.3E). In both cases, symmetry was assumed about the embryonic midline, and each imported 2D section was swept through 3D space to create a pseudo-embryonic geometry. For each model, the swept 2D section matched the tissue geometry under the indenter.

As a first approximation, we neglect any material difference between the endoderm and mesoderm, and model the entire tissue as a uniform, hyperelastic, nearly incompressible material, characterized by the modified neo-Hookean strain-energy density function

$$W = \frac{\mu}{2}\left(\bar{I} - 3\right) + p\left(1 - J - \frac{p}{2\kappa}\right). \tag{6.19}$$

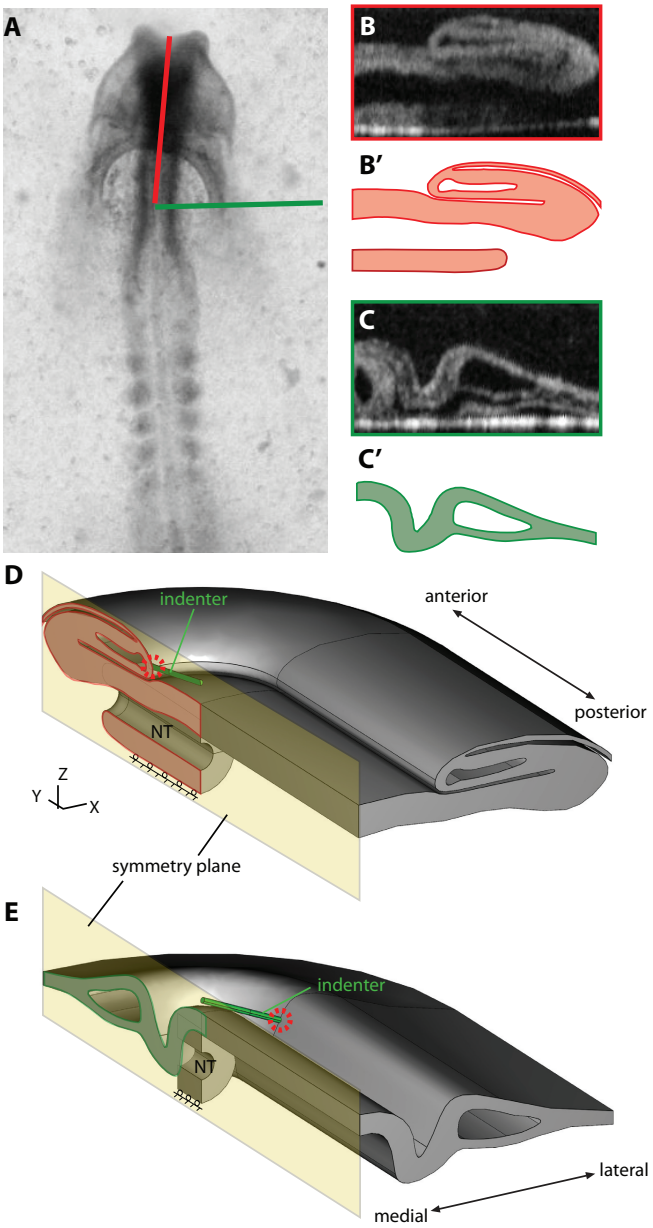

Figure 6.3: **Finite element model geometry based on OCT section data. (A)** Bright field image of HH stage 8 embryo. **(B,B')** Medial (B) OCT section and (B') segmented section indicated by red line in (A). **(C,C')** Lateral (C) OCT section and (C') segmented section indicated by green line in (A). **(D,E)** Segmented sections were imported into COMSOL and swept through 3D space to create pseudo-embryonic geometries. These models were used to simulate microindentation at the (D) medial and (E) lateral AIP. Dashed red circles indicate indentation sites. The dorsal side of the neural tube (NT) was placed on rollers to simulate the presence of the vitelline membrane.

In this equation, μ is the small-strain shear modulus, κ represents the bulk modulus, $J = \det \mathbf{F}$ is the dilatation ratio, where $\mathbf{F}$ represents the deformation gradient tensor, p is a penalty variable introduced for nearly incompressible materials, and $\bar{I} = J^{-2/3} \operatorname{tr}\left(\mathbf{F}^T \cdot \mathbf{F}\right)$ is a modified strain invariant.

The Cauchy stress tensor is given by the relation

$$\boldsymbol{\sigma} = J^{-1}\mathbf{F}.\frac{\partial W}{\partial \mathbf{F}^T}. \tag{6.20}$$

The indenter is modeled as a Hookean material, with material properties typical for Silica glass ($E = 73.1$ GPa and $\nu = 0.17$, from the COMSOL Material Library).

For simplicity, we assume that the indenter tip is adherent to the tissue, and simulate indentation by prescribing a known axial displacement at its far end. During indentation, the indenter force is calculated by integrating the normal axial stress across the cross-sectional area of the indenter. All other boundaries in the model are taken to be traction-free.

The indenter itself deforms only negligibly, so a simulated FD curve is generated using the prescribed axial displacement and the calculated indenter force.

6.4 Results

6.4.1 Gradients in both tension and stiffness are present around the AIP

The heart tube forms between HH stages 7 and 9 in the early chick embryo, approximately 24–36 hr into its 21-day incubation period. We therefore made linear incisions through the medial and lateral AIP in HH stage 8 embryos to probe the tissue stresses during heart tube formation (Fig. 6.4). The incisions at the midline opened immediately (Fig. 6.4B) to produce triangularly shaped wounds with a mean opening angle $\phi_M = 59 \pm 3^\circ$. Wounds in the lateral AIP, however, opened only slightly and to a significantly lesser extent than those at the midline, with a mean opening angle $\phi_L = 16 \pm 3^\circ$ (Fig. 6.4C). The same trend was observed regardless of whether

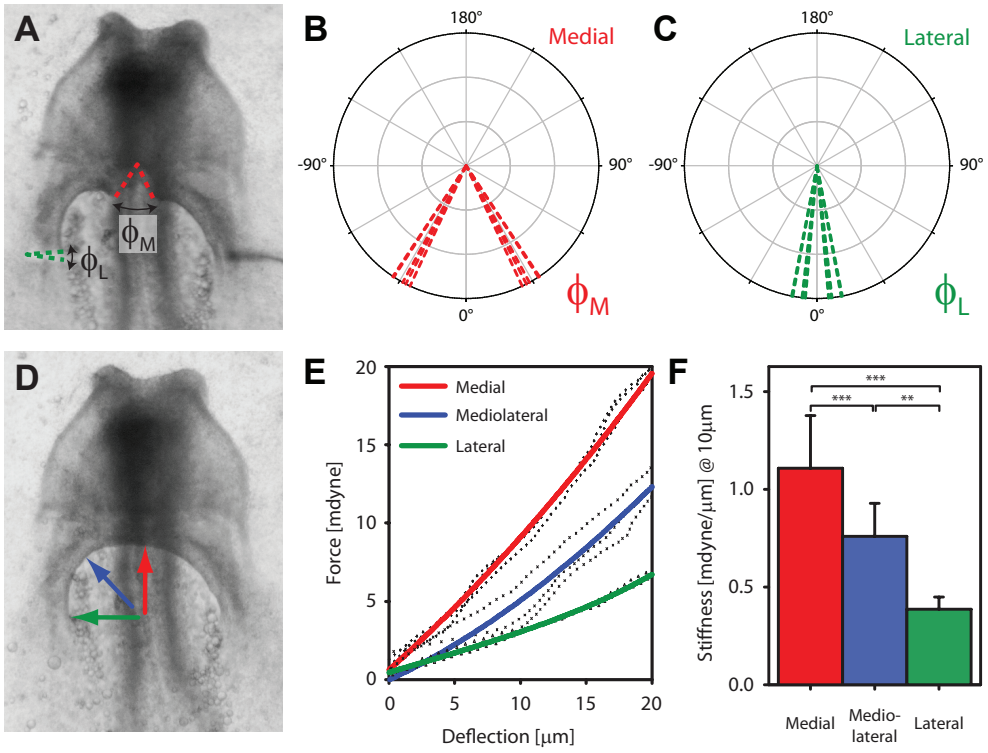

Figure 6.4: **Tension and tissue stiffness gradients around the AIP. (A-C)** Small linear incisions were made in the medial and lateral AIP, characterized by the opening angles $\phi_M = 59 \pm 3°$ and $\phi_L = 16 \pm 3°$, respectively. The wounds at the midline opened to a significantly greater extent ($P < 0.001$, two-sample Watson-Williams test,n=5). **(D)** Microindentation tests were conducted at medial (red), mediolateral (blue), and lateral (green) locations around the AIP. Arrows indicate the position of the indenter. **(E)** Force-deflection (FD) curves for a characteristic embryo. At each location, dotted black curves represent raw experimental data for three consecutive indentations. Solid lines represent regression curves fit to the experimental data. **(F)** Tissue stiffness measured at 10 μm deflection. A stiffness gradient, decreasing with distance from the midline, was observed around the AIP. * = P $<$ 0.05, ** = P $<$ 0.01, *** = P $<$ 0.001 (one-way ANOVA with Tukey post-hoc test, n=5).

the medial or lateral incision was made first, thus indicating a gradient in tension around the AIP, with the tensile stresses nearly vanishing laterally.

Moreover, microindentation tests at medial (red), mediolateral (blue), and lateral (green) locations around the AIP revealed a decreasing stiffness gradient (Fig. 6.4D-F). Regions of high tension corresponded to regions of high stiffness, which suggested to us the possibility that differential amounts of cytoskeletal contraction (which would tend to cause tension) might be behind the observed stiffness gradient.

6.4.2 Qualitative model results indicate uniform contraction around the AIP

To explore this idea, we simulate the endoderm and mesoderm around the AIP using the relatively simple model of a contracting beam on an elastic foundation (Fig. 6.2). The contractile beam represents the endoderm, and the mesoderm is modeled by a series of springs (Fig. 6.2B). Employing a linear growth theory for beams (see section 6.3.1 for further details), we consider the cases of both (i) uniform contraction, where $\epsilon_g(x) = -\epsilon_g^o$, and (ii) a decreasing linear gradient in contraction, where $\epsilon_g(x) = -\epsilon_g^o + \epsilon_g^o x/L$ (Fig. 6.2F). Since a linear theory is used, the particular value of ϵ_g^o does not qualitatively affect our results, and we demonstratively consider the case of $\epsilon_g^o = 0.1$.

Both contractile distributions produce a gradient in stress along the AIP (Fig. 6.5A,B). For the case of uniform contraction, as α increases (i.e., as the foundation stiffness increases, or beam modulus decreases), the gradient becomes more and more localized to the lateral end of the beam (Fig. 6.5A). When a linear gradient in contraction is included, however, the stresses decrease steadily along the entire length of the beam for all values of α (Fig. 6.5B). Moreover, as α decreases and the foundation effects attenuate, the qualitative shape of the curves looks increasingly similar between the two cases.

Thus, a comparison of our model results to our tissue cutting experiments alone is unable to distinguish between the cases of uniform and spatially graded contraction.

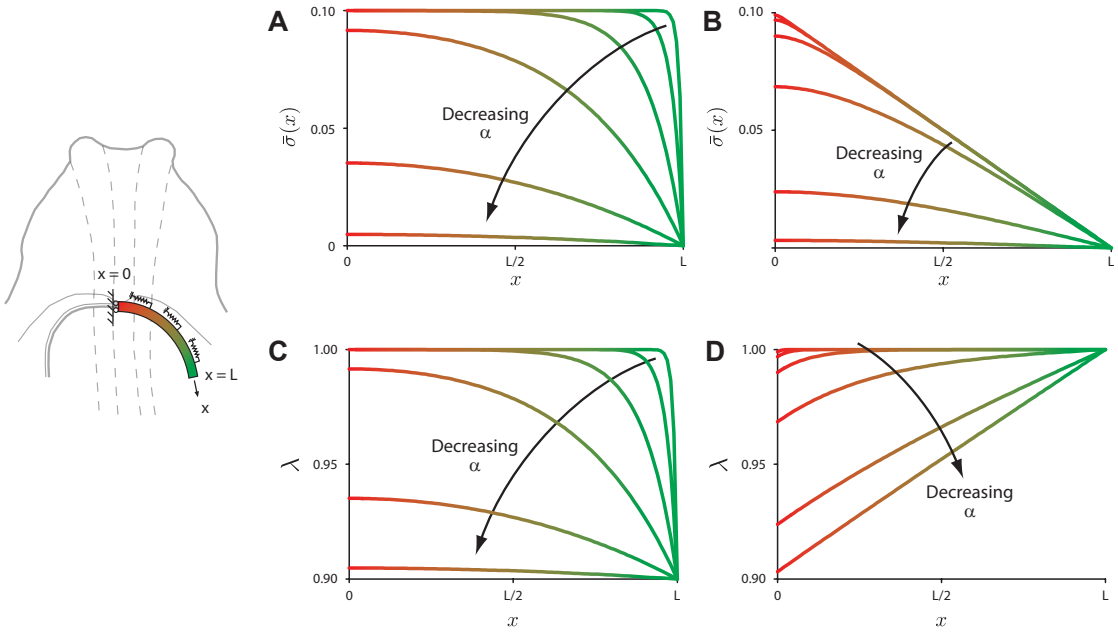

Figure 6.5: **Stress and stretch ratio plots for a contractile beam on an elastic foundation. (A,B)** Plots of stress $\bar{\sigma}(x) = \sigma(x)/E_o$ along contractile beam of length L for the cases of (A) uniform contraction and (B) a linear gradient in contraction. **(C,D)** Plots of the stretch ratio $\lambda(x)$ for the cases of (C) uniform contraction and (D) a linear gradient in contraction. Here, $\alpha = \sqrt{k/E_o}$ where k is the foundation stiffness and E_o is the Young's modulus. For each set of plots, we take $k/E_o = 10^i$, where $i = -5, -4, -3, -2, -1, 0$.

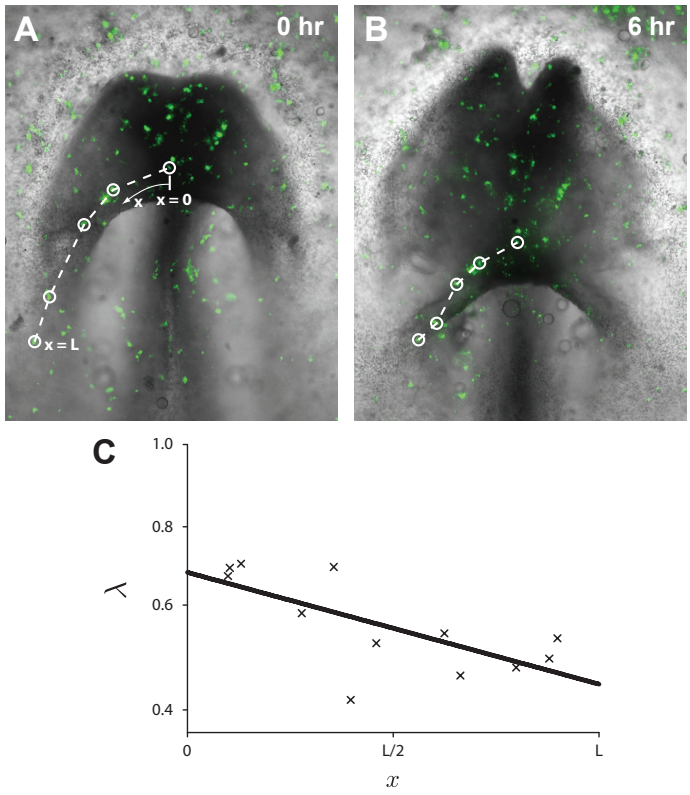

Figure 6.6: **Measuring endodermal stretch ratios around the AIP during heart tube formation. (A,B)** Bright field/fluorescent images of a characteristic HH stage 7+ embryo after (A) 0 hr and (B) 6 hr of incubation. Labeled endodermal cells, which formed an arc of segmented lines around the AIP, were tracked in time. The stretch ratio λ for each line segment was calculated by dividing the deformed length by the undeformed length. **(C)** Stretch ratios were evaluated at the midpoint of each line segment and plotted a function of the distance along the AIP x. A linear regression for $\lambda(x)$ showed that more tissue shortening occurred in the lateral, as opposed to the medial, region of AIP.

If we also consider, however, the deformation patterns around the AIP, and plot the stretch ratio λ along the length of the beam for both cases, divergent trends emerge (Fig. 6.5C,D). For uniform contraction, a majority of the tissue shortening occurs laterally (Fig. 6.5C), while for a linear gradient in contraction, the trend is reversed and more shortening is present at the midline (Fig. 6.5D).

To test between these two cases, we fluorescently labeled endodermal cells in HH stage 7+ embryos (i.e., before either the heart tube had formed) and cultured them ex ovo (Fig. 6.6). Labels positioned around the AIP were tracked in time (Fig. 6.6A,B) and used to compute endodermal stretch ratios. In these embryos, more shortening

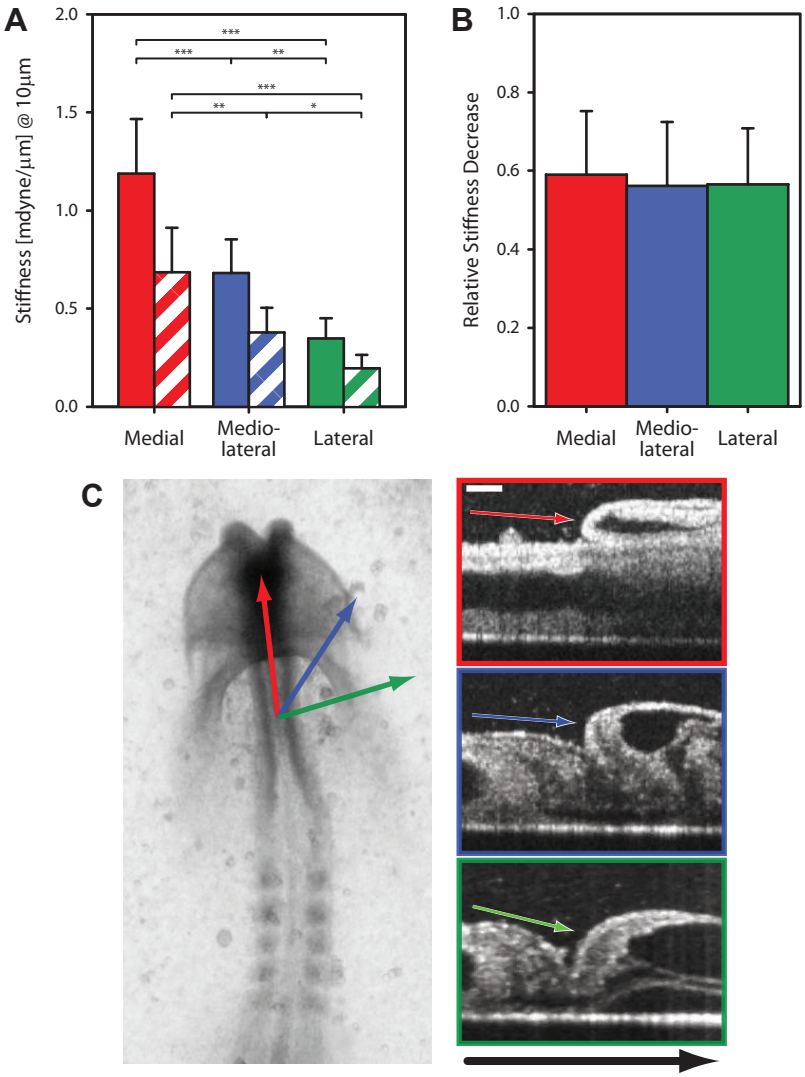

Figure 6.7: **Microindentation tests after treatment with the myosin II inhibitor blebbistatin. (A)** Tissue stiffness at medial (red), mediolateral (blue) and lateral (green) locations around the AIP both before (solid bars) and after (hatched bars) incubation with 100 μM blebbistatin. A residual stiffness gradient was still present after blebbistatin treatment. * = P $<$ 0.05, ** = P $<$ 0.01, *** = P $<$ 0.001 (one-way ANOVA with Tukey post-hoc test, n=5). Solid bars are the same as those included in Fig. 6.4F. **(B)** The relative stiffness decrease after treatment with blebbistatin nearly identical for each tissue location. **(C)** Bright field image of HH stage 8 embryo. OCT sections through each indentation location show differences in tissue geometry around the AIP. Arrows indicate the position of the indenter.

was observed laterally than at the midline (Fig. 6.6C), consistent with our model for uniform contraction (Fig. 6.5C).

As a further test, we also repeated our microindentation experiments in the presence of the myosin II inhibitor blebbistatin to determine the stiffness decrease when contraction was suppressed (Fig. 6.7). These experiments were conducted using the same embryos as those included in Fig. 6.4, so we were able to directly compare tissue stiffness measurements before and after blebbistatin treatment. On average, the relative stiffness decrease at each tissue location was approximately uniform and equal to $\sim 60\%$ (Fig. 6.7B). If we assume that any increase (or decrease) in tissue stiffness is proportional to the amount of contraction in the tissue (as has been assumed in other computational models of morphogenesis (Ramasubramanian and Taber, 2008)), this result further implicates uniform contraction around the AIP.

6.4.3 Simulated microindentation tests indicate a gradient in material properties.

Somewhat surprisingly, a stiffness gradient was still present around the AIP even after treatment with blebbistatin (Fig. 6.7B). This residual gradient could be due to either differences in tissue geometry or to differences in the passive mechanical properties of the tissue. Thus, to characterize tissue geometry in living embryos, we captured OCT sections at locations corresponding to each indentation site around the AIP (Fig. 6.7C). Visual inspection of these images showed marked differences in both the curvature and the thickness of the tissue under the indenter.

To test whether geometrical differences alone could account for the observed gradient, we constructed a 3D finite element model of the tissue around the AIP to simulate our microindentation experiments. As described in section 6.3.2, we used segmented OCT images to create a pseudo-embryonic geometry for the model. Since the largest difference in stiffness was observed between the medial and lateral regions of the AIP (Fig. 6.7A), we created separate models for these two cases. In both, we used the segmented OCT image corresponding to the indentation site of interest to create the swept model geometry (Fig. 6.3D,E).

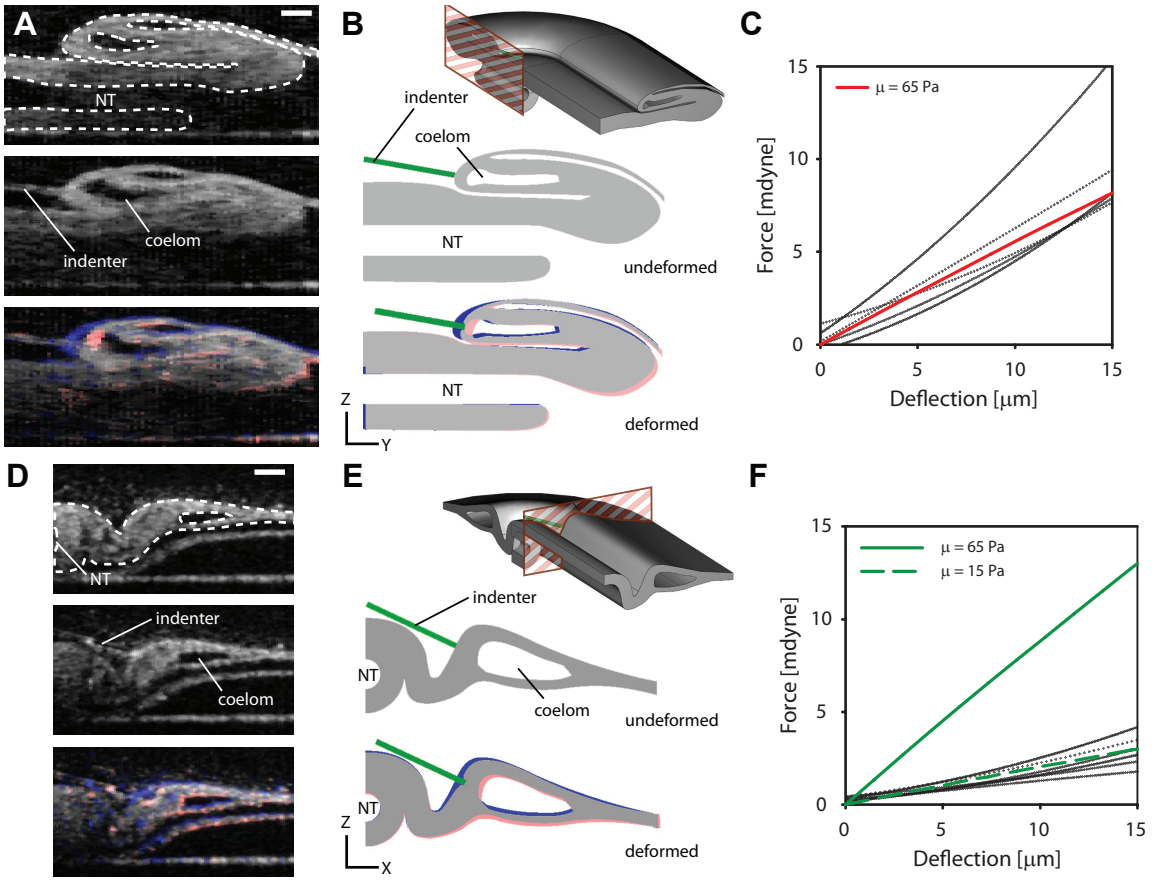

Figure 6.8: **Simulating our microindentation experiments around the AIP. (A,D)** OCT sections through the (A) medial and (D) lateral AIP before indentation (top), as the indenter first comes into contact the tissue (middle), and after indentation (bottom). Red pixels indicate the leading edge of the deformation, and blue pixels, the trailing edge. See section 6.2.5 for details. Scale bar = 200 μm. **(B,E)** Undeformed and deformed geometries from our models simulating microindentation of the (B) medial and (E) lateral AIP. The algorithms used to analyze our OCT images were used to characterize the leading and trailing edges of the deformation. Both models qualitatively match the tissue deformations observed experimentally. **(C)** The simulated force-deflection (FD) curve at the medial AIP (solid red line) approximately matches our experimental FD data after blebbistatin treatment (black dotted lines), if we specify $\mu = 65$ Pa. **(F)** If we use $\mu = 65$ Pa to simulate microindentation of the lateral AIP, the simulated FD curve (solid green line) is much stiffer than that seen experimentally (black dotted lines). When $\mu = 15$ Pa is included in the model, however, the simulated FD curve (dashed green line) matches our experimental data. These results suggest a gradient in passive mechanical properties around the AIP.

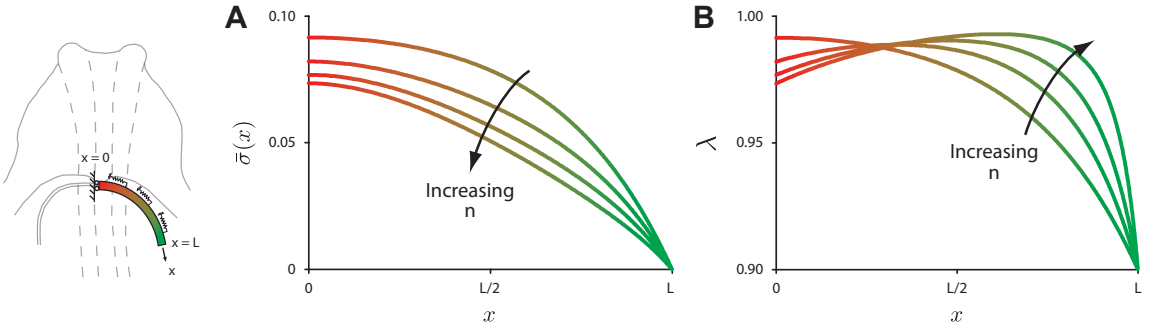

Figure 6.9: **Uniformly contracting beam with a linearly varying Young's modulus.** Plots of **(A)** stress $\bar{\sigma}(x) = \sigma(x)/E_o$ and **(B)** stretch ratio $\lambda(x)$ along a contractile beam of length L with a linearly varying Young's modulus given by $E(x) = E_o(1 - \frac{1-(1/n)}{L}\, x)$. Here, $n = 1, 2, 4, 10$ and k/E_o is held fixed at 10^{-3}.

We also performed microindentation experiments using OCT to characterize the geometry of the tissue under the indenter as it deformed (red pixels indicate the leading of the deformation; blue pixels, the trailing edge) (Fig. 6.8A,C).

Our microindentation simulations at both the medial and lateral regions of the AIP produce deformed shapes that qualitatively match those observed via OCT (Fig. 6.8B,D). This was not the case for preliminary 2D models, nor simple extruded 3D models, which did not include a crescentic AIP.

At the medial AIP, our simulated force-deflection (FD) curve roughly matches our experimental FD data if the small-strain shear modulus is taken as $\mu = 65$ Pa (Fig. 6.8E). Here, we use blebbistatin-treated experimental data for comparison, since we are interested in the residual stiffness gradient. When $\mu = 65$ Pa is included in the model for the lateral AIP, however, the simulated FD curve is much stiffer than that observed experimentally (Fig. 6.8F). But if μ is reduced to 15 Pa, the model more closely matches the experimental FD curves.

This result then suggests that differences in mechanical properties, not geometry, are responsible for the residual stiffness gradient around the AIP after blebbistatin treatment. We thus estimate an approximately 4-fold decrease in tissue modulus between the medial and lateral regions of the AIP.

If then, returning to our beam on a foundation model, we include a mechanical property gradient, and consider a uniformly contracting beam with a linearly varying

Young's modulus, the qualitative behavior is similar to that seen in our previous model with uniform contraction (compare Figs 6.9A,B and 6.5A,C) — the stresses vanish laterally (Fig. 6.9A) and most of the (overall) shortening occurs at the midline (Fig. 6.9B).

In this model, we include stiffness gradients on the order of that observed experimentally; the fold change in Young's modulus n varies from 1 to 10. Still, as the steepness of the gradient increases (i.e., as n increases) (Fig. 6.2E), the deformations at the lateral end of the beam become more local. The stress distribution, however, maintains a similar overall shape, but begins to flatten out and decrease somewhat in magnitude.

Taken together, these results suggest that while cytoskeletal contraction around the AIP is approximately uniform, a gradient in passive mechanical properties is present, decreasing with distance from the midline.

6.5 Discussion

At a fundamental level, morphogenesis is accomplished through the action of mechanical forces, as the simple geometry of the early embryo deforms to give rise to the intricate 3D structures of the adult organism (Blanchard and Adams, 2011). In metazoans, the embryo is comprised largely of thin epithelia (or cell sheets), and this dramatic transformation occurs as physical forces act both within and upon these cell sheets.

During animal development, cytoskeletal contractility provides a major intrinsic driving force for epithelial morphogenesis (Wozniak and Chen, 2009; Martin, 2010). Within each cell, meshworks of actin microfilaments are cross-linked with myosin motor proteins. These motors then work to pull antiparallel actin fibers toward one another and generate contractile force (Martin, 2010). In a host of model organisms, contractility has been shown to drive both cell shape changes (Martin et al., 2009; Solon et al., 2009; Blanchard et al., 2010) and cell intercalation (Skoglund et al., 2008; Fernandez-Gonzalez et al., 2009; Rauzi et al., 2010; Fernandez-Gonzalez and Zallen, 2011), as well as higher order structures like multicellular rosettes (Blankenship et al.,

2006) and actomyosin purse strings, such as observed during Drosophila dorsal closure (Kiehart et al., 2000; Hutson et al., 2003). This stands in stark contrast to morphogenesis in plants, which owing to the physical constraints of a cell wall, does not depend on actomyosin contractility. Instead, shape changes are driven primarily by changes in internal turgor pressure (Dumais et al., 2006).

Cytoskeletal contraction not only exerts forces, but also modifies the mechanical properties of the tissue — both actively contracting cells and tissues stiffen (Wakatsuki et al., 2000, 2001; Rémond et al., 2006; Zhou et al., 2009). This then muddles our understanding of the role contractility plays during development, since it both drives the deformations observed during morphogenesis and increases the rigidity of the tissues being deformed. This observation has led others to speculate about a possible role for mechanical feedback in regulating contraction (Taber, 2009; Davidson, 2011). Moreover, recent experimental work in Drosophila has indicated a possible role for mechanical tension in regulating myosin II dynamics (Fernandez-Gonzalez et al., 2009; Pouille et al., 2009) during early development.

Here, we show how cytoskeletal contractility and tissue stiffness are spatially distributed around the AIP during heart tube formation. In Chapter 5, we indicated that endodermal contraction in this region pulls the heart fields toward the midline, enabling them to fuse and form the primitive heart tube. By qualitatively comparing our model results with both label tracking and tissue cutting experiments, we suggest that this contraction is relatively uniform around the AIP.

Our microindentation tests revealed a decrease in tissue stiffness after treatment with blebbistatin (Fig. 6.7A,B). Thus, as observed by several others in different tissue structures (Rémond et al., 2006; Zhou et al., 2009; Filas et al., 2011), cytoskeletal contraction was shown to contribute to overall tissue stiffness. In addition, the observed stiffness decreases were on the order of those seen in both the heart and brain of later stage chick embryos treated with blebbistatin (Ramasubramanian et al., 2008; Filas et al., 2011).

When contraction was suppressed, we also observed a residual stiffness gradient around the AIP, decreasing with distance from the midline (Fig. 6.7A). Finite element simulations of our microindentation experiments suggest that this gradient is due to differences in the passive mechanical properties of the tissue (Fig. 6.8). The

small-strain modulus μ for a neo-Hookean material is related to the Young's modulus E for a linear elastic material by $E = 3\mu$ (Taber, 2004). Using this relation, our measured constitutive properties ($\mu = 65$ Pa and $\mu = 15$ Pa for the medial and lateral AIP, respectively) are on the order of those measured for dorsal isolates of early Xenopus laevis embryos ($E = 20 - 100$ Pa) (Zhou et al., 2009), and c-looped chick hearts ($\mu = 26$ Pa) (Zamir and Taber, 2004a).

This approximately 4-fold stiffness gradient is somewhat larger than the natural variations in tissue stiffness observed among Xenopus laevis gastrulae (von Dassow and Davidson, 2009). Moreover, since the gradient was consistently observed in every embryo we studied, it is tempting to speculate about both its molecular underpinnings and its possible morphogenetic role. Though regional differences in actomyosin contractility have been shown to account for variations in tissue stiffness (Zhou et al., 2009), that does not seem to be the case here, since a residual gradient was still observed after treatment with blebbistatin. An abundant extra-cellular matrix (ECM), however, is present between the mesoderm and endoderm (Linask and Lash, 1986; Drake et al., 1990; Wiens, 1996), and it would also be interesting to test whether differential amounts of cross-linking within the ECM might be able to explain the observed gradient.

Additionally, recent work using transgenic quail embryos has shown that endothelial cells in the forming vitelline vascular network migrate medially toward the heart (Sato et al., 2010). Since mechanical stiffness gradients have been shown to influence the directional movements of migrating cells in vitro (Lo et al., 2000; Discher et al., 2005), it would be interesting to investigate whether or not the observed gradient around the AIP contributes to these endothelial cell movements.

In conclusion, we propose that endodermal contraction, which draws the heart fields toward the midline, is uniform around the AIP. The passive mechanical properties of the tissue, however, vary – decreasing in stiffness with distance from the embryonic midline. These results then give new insight into how tissue stiffness and contractility are distributed during heart tube formation, and how they might contribute to the observed morphogenetic deformations.

Chapter 7

Conclusions

For decades, biologists have done the important work of identifying many of the genetic and molecular factors involved in heart development (Yutzey and Kirby, 2002; Buckingham et al., 2005; Abu-Issa and Kirby, 2007; Meilhac and Buckingham, 2010). Over the years, these efforts have helped elucidate the vast biochemical signaling networks, which drive cardiac specification and differentiation in the embryo (Olson and Srivastava, 1996). Even so, despite this deep molecular understanding of cardiogenesis, the biophysical mechanisms which link these molecular factors to actual, physical changes in cardiac morphology remain unclear (Taber, 2006).

Toward this end, we have identified some of the tissue-level forces that drive heart tube formation in the early chick embryo. Rather surprisingly, our work suggests that, although the heart is a mesodermally derived structure (i.e., the cardiac progenitors take up residence in the mesoderm), all three germ layers physically contribute to formation of the heart tube.

Head fold morphogenesis is the first step in this process. It sets the stage for cardiac development by folding the (initially flat) heart fields out-of-plane, enabling them to form a tube along the ventral aspect of the embryo. Our work suggests that head fold formation is driven by forces that originate in the ectoderm, forces that are typically associated with neurulation — the formation of the neural tube.

The primitive heart tube itself then forms as the mesodermal heart fields move toward the midline, and fuse to construct a straight muscle-wrapped tube. During this process, the mesoderm remains in close contact with the endoderm, and this medial motion is typically attributed to active crawling of the (mesodermal) heart fields over

the underlying endoderm. Our results, however, indicate that the endoderm plays a crucial mechanical role during this process. Instead of just serving as a passive, secretory substrate for the crawling mesoderm, the endoderm actively contracts and pulls the heart fields toward the midline. Moreover, defects in endodermal contraction can lead to heart malformations such as cardia bifida.

The ectoderm and endoderm thus contribute mechanically to the process of heart tube formation, a result which may have implications for cardiac tissue engineers who hope to recapitulate this process in vitro. While it is well established that inductive signaling between the different germ layers plays a role in cardiogenesis (Nascone and Mercola, 1996; Lough and Sugi, 2000; Brand, 2003), these physical interactions appear to also play an important morphogenetic role in shaping the heart.

Going forward, it would be interesting to more fully investigate the cellular and molecular mechanisms which underpin these tissue-level forces. For instance, are active cell shape changes or is cell intercalation responsible for the observed endodermal shortening around the AIP? And what are the actomyosin dynamics within these cells as the overall tissue shortens?

Advances in microscopy and targeted fluorescent reporter proteins have made answering questions like these a possibility. These techniques have been used to great effect in studies of Drosophila germ band extension (Blankenship et al., 2006; Rauzi et al., 2008; Butler et al., 2009; Fernandez-Gonzalez et al., 2009), dorsal closure (Kiehart et al., 2000; Hutson et al., 2003; Solon et al., 2009; Gorfinkiel et al., 2009; Blanchard et al., 2010), and ventral furrow formation (Martin et al., 2009, 2010). So far, however, their utility has been primarily restricted to genetically tractable model organisms like zebrafish and Drosophila. Pioneering work that seeks to create lines of transgenic quail (Sato et al., 2010), however, may make these dynamic studies of tissue morphogenesis possible in avian embryos.

Recent theoretical (Taber, 2008, 2009) and experimental work has also indicated a regulatory role for mechanical forces during development (Farge, 2003; Desprat et al., 2008; Fernandez-Gonzalez et al., 2009; Filas et al., 2011). In particular, during the later stage of looping, chick hearts have been shown to adapt to altered mechanical loading (Nerurkar et al., 2006; Ramasubramanian and Taber, 2008). Whether is the case for the forces that form the early tube remains an exciting avenue of research

to explore, as we work to connect physical mechanisms of morphogenesis with the underlying molecular cell biology and genetics.

References

Abu-Issa, R., Kirby, M. L., 2007. Heart field: from mesoderm to heart tube. Annu Rev Cell Dev Biol 23, 45–68.

Abu-Issa, R., Kirby, M. L., 2008. Patterning of the heart field in the chick. Dev Biol 319 (2), 223–33.

Alexander, J., Rothenberg, M., Henry, G. L., Stainier, D. Y. R., 1999. Casanova plays an early and essential role in endoderm formation in zebrafish. Dev Biol 215 (2), 343–57.

Alsan, B. H., Schultheiss, T. M., 2002. Regulation of avian cardiogenesis by Fgf8 signaling. Development 129 (8), 1935–43.

Andrée, B., Duprez, D., Vorbusch, B., Arnold, H. H., Brand, T., 1998. BMP-2 induces ectopic expression of cardiac lineage markers and interferes with somite formation in chicken embryos. Mech Dev 70 (1-2), 119–31.

Aristotle, 1970. Historia animalium. With an English translation by A. L. Peck. Harvard University Press, Cambridge, Mass.

Bain, J., McLauchlan, H., Elliott, M., Cohen, P., 2003. The specificities of protein kinase inhibitors: an update. Biochem J 371 (Pt 1), 199–204.

Balfour, F. M., 1881. A treatise on comparative embryology. MacMillan and Co., London,.

Bartman, T., Hove, J., 2005. Mechanics and function in heart morphogenesis. Dev Dyn 233 (2), 373–81.

Bellairs, R., 1953. Studies on the development of the foregut in the chick. II. The morphogenetic movements. J Embryol Exp Morphol 1 (December), 369–385.

Bellairs, R., Osmond, M., 2005. The atlas of chick development. Elsevier Academic, London.

Bénazéraf, B., Francois, P., Baker, R. E., Denans, N., Little, C. D., Pourquié, O., 2010. A random cell motility gradient downstream of FGF controls elongation of an amniote embryo. Nature 466 (7303), 248–52.

Bertet, C., Sulak, L., Lecuit, T., 2004. Myosin-dependent junction remodelling controls planar cell intercalation and axis elongation. Nature 429 (6992), 667–71.

Blanchard, G. B., Adams, R. J., 2011. Measuring the multi-scale integration of mechanical forces during morphogenesis. Curr Opin Genet Dev 21 (5), 653–663.

Blanchard, G. B., Kabla, A. J., Schultz, N. L., Butler, L. C., Sanson, B., Gorfinkiel, N., Mahadevan, L., Adams, R. J., 2009. Tissue tectonics: morphogenetic strain rates, cell shape change and intercalation. Nat Methods 6 (6), 458–64.

Blanchard, G. B., Murugesu, S., Adams, R. J., Martinez-Arias, A., Gorfinkiel, N., 2010. Cytoskeletal dynamics and supracellular organisation of cell shape fluctuations during dorsal closure. Development 137 (16), 2743–52.

Blankenship, J. T., Backovic, S. T., Sanny, J. S. P., Weitz, O., Zallen, J. a., 2006. Multicellular rosette formation links planar cell polarity to tissue morphogenesis. Dev Cell 11 (4), 459–70.

Brand, T., 2003. Heart development: molecular insights into cardiac specification and early morphogenesis. Dev Biol 258 (1), 1–19.

Brodland, G. W., Conte, V., Cranston, P. G., Veldhuis, J., Narasimhan, S., Hutson, M. S., Jacinto, A., Ulrich, F., Baum, B., Miodownik, M., 2010. Video force microscopy reveals the mechanics of ventral furrow invagination in Drosophila. Proc Natl Acad Sci U S A 107 (51), 22111–6.

Buckingham, M., Meilhac, S., Zaffran, S., 2005. Building the mammalian heart from two sources of myocardial cells. Nat Rev Genet 6 (11), 826–35.

Butler, L. C., Blanchard, G. B., Kabla, A. J., Lawrence, N. J., Welchman, D. P., Mahadevan, L., Adams, R. J., Sanson, B., 2009. Cell shape changes indicate a role for extrinsic tensile forces in Drosophila germ-band extension. Nat Cell Biol 11 (7), 859–64.

Chen, X., Brodland, G. W., 2008. Multi-scale finite element modeling allows the mechanics of amphibian neurulation to be elucidated. Phys Biol 5 (1), 015003.

Clark, A. G., Miller, A. L., Vaughan, E., Yu, H.-Y. E., Penkert, R., Bement, W. M., 2009. Integration of single and multicellular wound responses. Curr Biol 19 (16), 1389–95.

Colas, J. F., Schoenwolf, G. C., 2001. Towards a cellular and molecular understanding of neurulation. Dev Dyn 221 (2), 117–45.

Cui, C., Cheuvront, T. J., Lansford, R. D., Moreno-Rodriguez, R. A., Schultheiss, T. M., Rongish, B. J., 2009. Dynamic positional fate map of the primary heart-forming region. Dev Biol 332 (2), 212–22.

David, G., Humphrey, J. D., 2004. Redistribution of stress due to a circular hole in a nonlinear anisotropic membrane. J Biomech 37 (8), 1197–203.

Davidson, L. A., 2008. Integrating morphogenesis with underlying mechanics and cell biology. Curr Top Dev Biol 81 (07), 113–33.

Davidson, L. A., 2011. Embryo mechanics: balancing force production with elastic resistance during morphogenesis. Curr Top Dev Biol 95, 215–41.

Davidson, L. A., Joshi, S. D., Kim, H. Y., von Dassow, M., Zhang, L., Zhou, J., 2010. Emergent morphogenesis: elastic mechanics of a self-deforming tissue. J Biomech 43 (1), 63–70.

Davidson, L. A., von Dassow, M., Zhou, J., 2009. Multi-scale mechanics from molecules to morphogenesis. Int J Biochem Cell Biol 41 (11), 2147–62.

Davies, J. A., 2005. Mechanisms of morphogenesis. Elsevier Academic Press, Amsterdam ; Boston.

de Jong, F., Geerts, W. J., Lamers, W. H., Los, J. A., Moorman, A. F., 1990. Isomyosin expression pattern during formation of the tubular chicken heart: a three-dimensional immunohistochemical analysis. Anatomical Record 226 (2), 213–227.

de la Cruz, M. V., Sanchez-Gomez, C., 1998. Straight tube heart. Primitive cardiac cavities vs. primitive cardiac segments. In: Cruz, M. V., Markwald, R. R. (Eds.), Living morphogenesis of the heart. Cardiovascular Molecular Morphogenesis. Birkhäuser Boston, pp. 85–98.

DeHaan, R. L., 1959. Cardia bifida and the development of pacemaker function in the early chick heart. Dev Biol 1 (6), 586–602.

DeHaan, R. L., 1963. Migration patterns of the precardiac mesoderm in the early chick embrvo. Exp Cell Res 29, 544–60.

DeHaan, R. L., 1967. Development of form in the embryonic heart. An experimental approach. Circulation 35 (5), 821–33.

Desprat, N., Supatto, W., Pouille, P.-A., Beaurepaire, E., Farge, E., 2008. Tissue deformation modulates twist expression to determine anterior midgut differentiation in Drosophila embryos. Dev Cell 15 (3), 470–7.

Discher, D. E., Janmey, P., Wang, Y.-L., 2005. Tissue cells feel and respond to the stiffness of their substrate. Science 310 (5751), 1139–43.

Drake, C. J., Davis, L. A., Walters, L., Little, C. D., 1990. Avian vasculogenesis and the distribution of collagens I, IV, laminin, and fibronectin in the heart primordia. J Exp Zool 255 (3), 309–22.

Drake, C. J., Jacobson, A. G., 1988. A survey by scanning electron microscopy of the extracellular matrix and endothelial components of the primordial chick heart. Anat Rec 222 (4), 391–400.

Du, A., Sanger, J. M., Linask, K. K., Sanger, J. W., 2003. Myofibrillogenesis in the first cardiomyocytes formed from isolated quail precardiac mesoderm. Dev Biol 257 (2), 382–94.

Dumais, J., Shaw, S. L., Steele, C. R., Long, S. R., Ray, P. M., 2006. An anisotropic-viscoplastic model of plant cell morphogenesis by tip growth. Int J Dev Biol 50 (2-3), 209–22.

Duyao, M. P., Auerbach, A. B., Ryan, A., Persichetti, F., Barnes, G. T., McNeil, S. M., Ge, P., Vonsattel, J. P., Gusella, J. F., Joyner, A. L., 1995. Inactivation of the mouse Huntington's disease gene homolog Hdh. Science 269 (5222), 407–10.

Engler, A. J., Sen, S., Sweeney, H. L., Discher, D. E., 2006. Matrix elasticity directs stem cell lineage specification. Cell 126 (4), 677–89.

Ettensohn, C. A., 1985. Mechanisms of epithelial invagination. Q Rev Biol 60 (3), 289–307.

Ezin, A. M., Fraser, S. E., Bronner-Fraser, M., 2009. Fate map and morphogenesis of presumptive neural crest and dorsal neural tube. Dev Biol 330 (2), 221–36.

Farge, E., 2003. Mechanical induction of Twist in the Drosophila foregut/stomodeal primordium. Curr Biol 13 (16), 1365–77.

Farhadifar, R., Röper, J.-C., Aigouy, B., Eaton, S., Jülicher, F., 2007. The influence of cell mechanics, cell-cell interactions, and proliferation on epithelial packing. Curr Biol 17 (24), 2095–104.

Fernandez-Gonzalez, R., Simoes, S. D. M., Röper, J.-C., Eaton, S., Zallen, J. A., 2009. Myosin II dynamics are regulated by tension in intercalating cells. Dev Cell 17 (5), 736–43.

Fernandez-Gonzalez, R., Zallen, J. A., 2011. Oscillatory behaviors and hierarchical assembly of contractile structures in intercalating cells. Phys Biol 8 (4), 045005.

Filas, B. A., Bayly, P. V., Taber, L. A., 2011. Mechanical stress as a regulator of cytoskeletal contractility and nuclear shape in embryonic epithelia. Ann Biomed Eng 39 (1), 443–54.

Filas, B. A., Efimov, I. R., Taber, L. A., 2007. Optical coherence tomography as a tool for measuring morphogenetic deformation of the looping heart. Anat Rec 290 (9), 1057–68.

Filas, B. A., Knutsen, A. K., Bayly, P. V., Taber, L. A., 2008. A new method for measuring deformation of folding surfaces during morphogenesis. J Biomech Eng 130 (6), 061010.

Foster, M., Balfour, F. M., 1883. The elements of embryology, 2nd Edition. Macmillan and Co., London.

Fredberg, J. J., Inouye, D., Miller, B., Nathan, M., Jafari, S., Raboudi, S. H., Butler, J. P., Shore, S. A., 1997. Airway smooth muscle, tidal stretches, and dynamically determined contractile states. Am J Respir Crit Care Med 156 (6), 1752–9.

Fujimoto, J. G., 2003. Optical coherence tomography for ultrahigh resolution in vivo imaging. Nat Biotechnol 21 (11), 1361–7.

Fung, Y. C., Fronek, K., Patitucci, P., 1979. Pseudoelasticity of arteries and the choice of its mathematical expression. Am J Physiol 237 (5), H620–31.

Gannon, M., Bader, D., 1995. Initiation of cardiac differentiation occurs in the absence of anterior endoderm. Development 121 (8), 2439–50.

Garavito-Aguilar, Z. V., Riley, H. E., Yelon, D., 2010. Hand2 ensures an appropriate environment for cardiac fusion by limiting Fibronectin function. Development 137 (19), 3215–20.

Garcia-Martinez, V., Schoenwolf, G. C., 1993. Primitive-streak origin of the cardiovascular system in avian embryos. Dev Biol 159 (2), 706–19.

Gilbert, S. F., 2000. Developmental biology, 6th Edition. Sinauer Associates, Sunderland, Mass.

Gjorevski, N., Nelson, C. M., 2010a. Endogenous patterns of mechanical stress are required for branching morphogenesis. Integr Biol 2 (9), 424–34.

Gjorevski, N., Nelson, C. M., 2010b. The mechanics of development: models and methods for tissue morphogenesis. Birth Defects Res C Embryo Today 90 (3), 193–202.

Glazier, J., Graner, F., 1993. Simulation of the differential adhesion driven rearrangement of biological cells. Phys Rev E Stat Phys Plasmas Fluids Relat Interdiscip Topics 47 (3), 2128–2154.

Gorfinkiel, N., Blanchard, G. B., Adams, R. J., Martinez Arias, A., 2009. Mechanical control of global cell behaviour during dorsal closure in Drosophila. Development 136 (11), 1889–98.

Graner, F., Glazier, J., 1992. Simulation of biological cell sorting using a two-dimensional extended Potts model. Phys Rev Lett 69 (13), 2013–2016.

Gutzman, J. H., Graeden, E. G., Lowery, L. A., Holley, H. S., Sive, H., 2008. Formation of the zebrafish midbrain-hindbrain boundary constriction requires laminin-dependent basal constriction. Mech Dev 125 (11-12), 974–83.

Haigo, S. L., Hildebrand, J. D., Harland, R. M., Wallingford, J. B., 2003. Shroom induces apical constriction and is required for hingepoint formation during neural tube closure. Curr Biol 13 (24), 2125–37.

Hamburger, V., Hamilton, H. L., 1951. A series of normal stages in the development of the chick embryo. J Morphol 88 (1), 49–92.

Holtzman, N. G., Schoenebeck, J. J., Tsai, H.-J., Yelon, D., 2007. Endocardium is necessary for cardiomyocyte movement during heart tube assembly. Development 134 (12), 2379–86.

Holzapfel, G. A., 2000. Nonlinear solid mechanics: a continuum approach for engineering. Wiley, New York.

Huang, D., Swanson, E. A., Lin, C. P., Schuman, J. S., Stinson, W. G., Chang, W., Hee, M. R., Flotte, T., Gregory, K., Puliafito, C. A., 1991. Optical coherence tomography. Science 254 (5035), 1178–81.

Humphrey, J. D., Strumpf, R. K., Yin, F. C., 1990. Determination of a constitutive relation for passive myocardium: I. A new functional form. J Biomech Eng 112 (3), 333–9.

Hutson, M. S., Tokutake, Y., Chang, M.-S., Bloor, J. W., Venakides, S., Kiehart, D. P., Edwards, G. S., 2003. Forces for morphogenesis investigated with laser microsurgery and quantitative modeling. Science 300 (5616), 145–9.

Joshi, S. D., von Dassow, M., Davidson, L. a., 2010. Experimental control of excitable embryonic tissues: three stimuli induce rapid epithelial contraction. Exp Cell Res 316 (1), 103–14.

Keller, E. F., 2002. Making sense of life : explaining biological development with models, metaphors, and machines. Harvard University Press, Cambridge, Mass. ; London.

Kiehart, D. P., Galbraith, C. G., Edwards, K. A., Rickoll, W. L., Montague, R. A., 2000. Multiple forces contribute to cell sheet morphogenesis for dorsal closure in Drosophila. J Cell Biol 149 (2), 471–90.

Kirby, M. L., 2007. Cardiac development. Oxford University Press, Oxford.

Koehl, M. A. R., 1990. Biomechanical approaches to morphogenesis. Semin Dev Biol 1, 367–378.

Kolega, J., 2004. Phototoxicity and photoinactivation of blebbistatin in UV and visible light. Biochem Biophys Res Commun 320 (3), 1020–5.

Krieg, M., Arboleda-Estudillo, Y., Puech, P.-H., Käfer, J., Graner, F., Müller, D. J., Heisenberg, C.-P., 2008. Tensile forces govern germ-layer organization in zebrafish. Nat Cell Biol 10 (4), 429–36.

Kuo, C. T., Morrisey, E. E., Anandappa, R., Sigrist, K., Lu, M. M., Parmacek, M. S., Soudais, C., Leiden, J. M., 1997. GATA4 transcription factor is required for ventral morphogenesis and heart tube formation. Genes Dev 11 (8), 1048–60.

Langer, K., 1978a. On the anatomy and physiology of the skin. I. The cleavability of the cutis. (Presented at the meeting of 26th April 1861.). Br J Plast Surg 31 (1), 3–8.

Langer, K., 1978b. On the anatomy and physiology of the skin. II. Skin tension. (Presented at the meeting of 27th November 1861.). Br J Plast Surg 31 (2), 93–106.

Lanir, Y., Fung, Y. C., 1974. Two-dimensional mechanical properties of rabbit skin. II. Experimental results. J Biomech 7 (2), 171–82.

Lawson, A., Anderson, H., Schoenwolf, G. C., 2001. Cellular mechanisms of neural fold formation and morphogenesis in the chick embryo. Anat Rec 262 (2), 153–68.

Lecuit, T., 2008. "Developmental mechanics": cellular patterns controlled by adhesion, cortical tension and cell division. HFSP J 2 (2), 72–8.

Lecuit, T., Lenne, P.-F., 2007. Cell surface mechanics and the control of cell shape, tissue patterns and morphogenesis. Nat Rev Mol Cell Biol 8 (8), 633–44.

Lee, H. Y., Nagele, R. G., 1985. Studies on the mechanisms of neurulation in the chick: interrelationship of contractile proteins, microfilaments, and the shape of neuroepithelial cells. J Exp Zool 235 (2), 205–15.

Lewis, W. H., 1947. Mechanics of invagination. Anat Rec 97 (2), 139–156.

Lillie, F. R., 1952. Development of the chick, an introduction to embryology, 3rd Edition. Holt, New York,.

Linask, K. K., 2003. Regulation of heart morphology: current molecular and cellular perspectives on the coordinated emergence of cardiac form and function. Birth Defects Res C Embryo Today 69 (1), 14–24.

Linask, K. K., Lash, J. W., 1986. Precardiac cell migration: fibronectin localization at mesoderm-endoderm interface during directional movement. Dev Biol 114 (1), 87–101.

Linask, K. K., Lash, J. W., 1988a. A role for fibronectin in the migration of avian precardiac cells. I. Dose-dependent effects of fibronectin antibody. Dev Biol 129 (2), 315–23.

Linask, K. K., Lash, J. W., 1988b. A role for fibronectin in the migration of avian precardiac cells. II. Rotation of the heart-forming region during different stages and its effects. Dev Biol 129 (2), 324–9.

Lo, C. M., Wang, H. B., Dembo, M., Wang, Y. L., 2000. Cell movement is guided by the rigidity of the substrate. Biophys J 79 (1), 144–52.

Lodish, H. F., 2004. Molecular cell biology, 5th Edition. W.H. Freeman and Company, New York.

Lough, J., Sugi, Y., 2000. Endoderm and heart development. Dev Dyn 217 (4), 327–42.

Lubarsky, B., Krasnow, M. A., 2003. Tube morphogenesis: making and shaping biological tubes. Cell 112 (1), 19–28.

Manasek, F. J., 1968. Embryonic development of the heart. I. A light and electron microscopic study of myocardial development in the early chick embryo. J Morphol 125 (3), 329–65.

Manasek, F. J., Nugent, J., O'Connor, M., 1983. Control of early embryonic heart morphogenesis: a hypothesis. In: Development of the Vascular System. Pitman, London, pp. 4–19.

Martin, A. C., 2010. Pulsation and stabilization: contractile forces that underlie morphogenesis. Dev Biol 341 (1), 114–25.

Martin, A. C., Gelbart, M., Fernandez-Gonzalez, R., Kaschube, M., Wieschaus, E. F., 2010. Integration of contractile forces during tissue invagination. J Cell Biol 188 (5), 735–49.

Martin, A. C., Kaschube, M., Wieschaus, E. F., 2009. Pulsed contractions of an actin-myosin network drive apical constriction. Nature 457 (7228), 495–9.

Marvin, M. J., Di Rocco, G., Gardiner, A., Bush, S. M., Lassar, A. B., 2001. Inhibition of Wnt activity induces heart formation from posterior mesoderm. Genes Dev 15 (3), 316–27.

Mathar, J., 1934. Determination of initial stresses by measuring the deformations around drilled holes. Trans. ASME 56, 249–254.

Meilhac, S. M., Buckingham, M. E., 2010. The behavior of cells that form the myocardial compartments of the vertebrate heart. In: Heart Development and Regeneration. Vol. I. Elsevier Inc., pp. 195–217.

Molkentin, J. D., Kalvakolanu, D. V., Markham, B. E., 1994. Transcription factor GATA-4 regulates cardiac muscle-specific expression of the alpha-myosin heavy-chain gene. Mol Cell Biol 14 (7), 4947–57.

Molkentin, J. D., Lin, Q., Duncan, S. A., Olson, E. N., 1997. Requirement of the transcription factor GATA4 for heart tube formation and ventral morphogenesis. Genes Dev 11 (8), 1061–72.

Moore, K. L., Persaud, T. V. N., Shiota, K., 2000. Color atlas of clinical embryology, 2nd Edition. Saunders, Philadelphia, PA.

Moreno-Rodriguez, R. A., Krug, E. L., Reyes, L., Villavicencio, L., Mjaatvedt, C. H., Markwald, R. R., 2006. Bidirectional fusion of the heart-forming fields in the developing chick embryo. Dev Dyn 235 (1), 191–202.

Moury, J. D., Schoenwolf, G. C., 1995. Cooperative model of epithelial shaping and bending during avian neurulation: autonomous movements of the neural plate, autonomous movements of the epidermis, and interactions in the neural plate/epidermis transition zone. Dev Dyn 204 (3), 323–37.

Muñoz, J. J., Barrett, K., Miodownik, M., 2007. A deformation gradient decomposition method for the analysis of the mechanics of morphogenesis. J Biomech 40 (6), 1372–80.

Muñoz, J. J., Conte, V., Miodownik, M., 2010. Stress-dependent morphogenesis: continuum mechanics and truss systems. Biomech Model Mechanobiol 9 (4), 451–67.

Narita, N., Bielinska, M., Wilson, D. B., 1997. Wild-type endoderm abrogates the ventral developmental defects associated with GATA-4 deficiency in the mouse. Dev Biol 189 (2), 270–4.

Nascone, N., Mercola, M., 1995. An inductive role for the endoderm in Xenopus cardiogenesis. Development 121 (2), 515–23.

Nascone, N., Mercola, M., 1996. Endoderm and cardiogenesis new insights. Trends Cardiovasc Med 6 (7), 211–6.

Nerurkar, N. L., Ramasubramanian, A., Taber, L. a., 2006. Morphogenetic adaptation of the looping embryonic heart to altered mechanical loads. Dev Dyn 235 (7), 1822–9.

Odell, G. M., Oster, G., Alberch, P., Burnside, B., 1981. The mechanical basis of morphogenesis. I. Epithelial folding and invagination. Dev Biol 85 (2), 446–62.

Oden, J. T., Key, J. E., 1972. On the effect of the form of the strain energy function on the solution of a boundary-value problem in finite elasticity. Comput. Struct. 2 (4), 585–592.

Olson, E. N., Srivastava, D., 1996. Molecular pathways controlling heart development. Science 272 (5262), 671–6.

Oostra, R. J., Steding, G., Lamers, W. H., Moorman, A. F., 2007. Steding's and Viragh's scanning electron microscopy atlas of the developing human heart. Springer, New York ; Berlin.

Orts-Llorca, F., 1963. Influence of the endoderm on heart differentiation during the early stages of development of the chicken embryo. Wilhelm Roux' Arch. Entwicklungsmech. Organ. 154 (6), 533–551.

Patten, B. M., 1971. Early embryology of the chick. McGraw-Hill, New York.

Pouille, P.-A., Ahmadi, P., Brunet, A.-C., Farge, E., 2009. Mechanical signals trigger Myosin II redistribution and mesoderm invagination in Drosophila embryos. Sci Signal 2 (66), ra16.

Ragkousi, K., Beh, J., Sweeney, S., Starobinska, E., Davidson, B., 2011. A single GATA factor plays discrete, lineage specific roles in ascidian heart development. Dev Biol 352 (1), 154–63.

Ramasubramanian, A., Latacha, K. S., Benjamin, J. M., Voronov, D. A., Ravi, A., Taber, L. A., 2006. Computational model for early cardiac looping. Ann Biomed Eng 34 (8), 1355–1369.

Ramasubramanian, A., Nerurkar, N. L., Achtien, K. H., Filas, B. a., Voronov, D. a., Taber, L. a., 2008. On modeling morphogenesis of the looping heart following mechanical perturbations. J Biomech Eng 130 (6), 061018.

Ramasubramanian, A., Taber, L. a., 2008. Computational modeling of morphogenesis regulated by mechanical feedback. Biomech Model Mechanobiol 7 (2), 77–91.

Rauzi, M., Lenne, P.-F., Lecuit, T., 2010. Planar polarized actomyosin contractile flows control epithelial junction remodelling. Nature 468 (7327), 1110–4.

Rauzi, M., Verant, P., Lecuit, T., Lenne, P.-F., 2008. Nature and anisotropy of cortical forces orienting Drosophila tissue morphogenesis. Nat Cell Biol 10 (12), 1401–10.

Rawles, M. E., 1943. The heart-forming areas of the early chick blastoderm. Physiol Zool 16 (1), 22–43.

Redkar, A., Montgomery, M., Litvin, J., 2001. Fate map of early avian cardiac progenitor cells. Development 128 (12), 2269–79.

Rémond, M. C., Fee, J. A., Elson, E. L., Taber, L. A., 2006. Myosin-based contraction is not necessary for cardiac c-looping in the chick embryo. Anat Embryol (Berl) 211 (5), 443–54.

Rendler, N., Vigness, I., 1966. Hole-drilling strain-gage method of measuring residual stresses. Exp. Mech. 6 (12), 577–586.

Rivlin, R. S., Thomas, A. G., 1951. Large Elastic Deformations of Isotropic Materials. VIII. Strain Distribution around a Hole in a Sheet. Phil Trans R Soc A 243 (865), 289–298.

Rodriguez, E. K., Hoger, A., McCulloch, A. D., 1994. Stress-dependent finite growth in soft elastic tissues. J Biomech 27 (4), 455–67.

Rosenquist, G. C., 1966. A radioautographic study of labeled grafts in the chick blastoderm. Development from primitive streak stages to stage 12. Carnegie Inst. Wash. Contrib. Embryol. 38, 71–110.

Rosenquist, G. C., 1970. Cardia bifida in chick embryos: anterior and posterior defects produced by transplanting tritiated thymidine-labeled grafts medial to the heart-forming regions. Teratology 3 (2), 135–42.

Rosenquist, G. C., DeHaan, R. L., 1966. Migration of precardiac cells in the chick embryo: a radioautographic study. Carnegie Inst. Wash. Contrib. Embryol. 38, 111–121.

Sato, Y., Poynter, G., Huss, D., Filla, M. B., Czirok, A., Rongish, B. J., Little, C. D., Fraser, S. E., Lansford, R., 2010. Dynamic analysis of vascular morphogenesis using transgenic quail embryos. PLoS ONE 5 (9), e12674.

Sausedo, R. A., Smith, J. L., Schoenwolf, G. C., 1997. Role of nonrandomly oriented cell division in shaping and bending of the neural plate. J Comp Neurol 381 (4), 473–88.

Schenk, J., Wilsch-Bräuninger, M., Calegari, F., Huttner, W. B., 2009. Myosin II is required for interkinetic nuclear migration of neural progenitors. Proc Natl Acad Sci U S A 106 (38), 16487–92.

Schier, A. F., Neuhauss, S. C., Helde, K. A., Talbot, W. S., Driever, W., 1997. The one-eyed pinhead gene functions in mesoderm and endoderm formation in zebrafish and interacts with no tail. Development 124 (2), 327–42.

Schoenwolf, G. C., 1994. Formation and patterning of the avian neuraxis: one dozen hypotheses. Ciba Found Symp 181, 25–38; discussion 38–50.

Schoenwolf, G. C., Alvarez, I. S., 1989. Roles of neuroepithelial cell rearrangement and division in shaping of the avian neural plate. Development 106 (3), 427–39.

Schoenwolf, G. C., Sheard, P., 1989. Shaping and bending of the avian neural plate as analysed with a fluorescent-histochemical marker. Development 105 (1), 17–25.

Schoenwolf, G. C., Smith, J. L., 2000. Gastrulation and early mesodermal patterning in vertebrates. Methods Mol Biol 135 (10), 113–25.

Schultheiss, T. M., Burch, J. B., Lassar, A. B., 1997. A role for bone morphogenetic proteins in the induction of cardiac myogenesis. Genes Dev 11 (4), 451–62.

Schultheiss, T. M., Xydas, S., Lassar, A. B., 1995. Induction of avian cardiac myogenesis by anterior endoderm. Development 121 (12), 4203–14.

Selman, G. G., 1958. The forces producing neural closure in amphibia. J Embryol Exp Morphol 6 (3), 448–65.

Shore, T. W., Pickering, J. W., 1889. The proamnion and amnion in the chick. J Anat Physiol 24 (Pt 1), 1–21.

Skoglund, P., Rolo, A., Chen, X., Gumbiner, B. M., Keller, R., 2008. Convergence and extension at gastrulation require a myosin IIB-dependent cortical actin network. Development 135 (14), 2435–44.

Slack, J. M. W., 2006. Essential developmental biology, 2nd Edition. Blackwell Pub., Malden, MA ; Oxford.

Smith, J. L., Schoenwolf, G. C., 1988. Role of cell-cycle in regulating neuroepithelial cell shape during bending of the chick neural plate. Cell Tissue Res 252 (3), 491–500.

Smith, J. L., Schoenwolf, G. C., 1997. Neurulation: coming to closure. Trends Neurosci 20 (11), 510–7.

Sokal, R. R., Rohlf, F. J., 1981. Biometry : the principles and practice of statistics in biological research, 2nd Edition. W. H. Freeman, San Francisco.

Solon, J., Kaya-Copur, A., Colombelli, J., Brunner, D., 2009. Pulsed forces timed by a ratchet-like mechanism drive directed tissue movement during dorsal closure. Cell 137 (7), 1331–42.

Stalsberg, H., DeHaan, R. L., 1968. Endodermal movements during foregut formation in the chick embryo. Dev Biol 18 (2), 198–215.

Stalsberg, H., DeHaan, R. L., 1969. The precardiac areas and formation of the tubular heart in the chick embryo. Dev Biol 19 (2), 128–59.

Taber, L. A., 1995. Biomechanics of growth, remodeling, and morphogenesis. Appl. Mech. Rev. 48 (8), 487.

Taber, L. A., 2001. Biomechanics of cardiovascular development. Annu Rev Biomed Eng 3, 1–25.

Taber, L. A., 2004. Nonlinear theory of elasticity: applications in biomechanics. World Scientific, River Edge, NJ.

Taber, L. A., 2006. Biophysical mechanisms of cardiac looping. Int J Dev Biol 50 (2-3), 323–32.

Taber, L. A., 2008. Theoretical study of Beloussov's hyper-restoration hypothesis for mechanical regulation of morphogenesis. Biomech Model Mechanobiol 7 (6), 427–41.

Taber, L. A., 2009. Towards a unified theory for morphomechanics. Phil Trans R Soc A 367 (1902), 3555–83.

Thompson, D. W., 1942. On growth and form. Cambridge University Press, Cambridge.

Timoshenko, S., Woinowsky-Krieger, S., 1959. Theory of plates and shells, 2nd Edition. McGraw-Hill, New York.

Trepat, X., Wasserman, M. R., Angelini, T. E., Millet, E., Weitz, D. A., Butler, J. P., Fredberg, J. J., 2009. Physical forces during collective cell migration. Nature Physics 5 (6), 426–430.

Trinh, L. A., Stainier, D. Y. R., 2004. Fibronectin regulates epithelial organization during myocardial migration in zebrafish. Dev Cell 6 (3), 371–82.

Varner, V. D., Voronov, D. A., Taber, L. A., 2010. Mechanics of head fold formation: investigating tissue-level forces during early development. Development 137 (22), 3801–11.

von Dassow, M., Davidson, L. a., 2009. Natural variation in embryo mechanics: gastrulation in Xenopus laevis is highly robust to variation in tissue stiffness. Dev Dyn 238 (1), 2–18.

Voronov, D. A., Alford, P. W., Xu, G., Taber, L. A., 2004. The role of mechanical forces in dextral rotation during cardiac looping in the chick embryo. Dev Biol 272 (2), 339–50.

Voronov, D. A., Taber, L. A., 2002. Cardiac looping in experimental conditions: effects of extraembryonic forces. Dev Dyn 224 (4), 413–21.

Waddington, C. H., 1939. Order of magnitude of morphogenetic forces. Nature 144 (3649), 637–637.

Wakatsuki, T., Kolodney, M. S., Zahalak, G. I., Elson, E. L., 2000. Cell mechanics studied by a reconstituted model tissue. Biophys J 79 (5), 2353–68.

Wakatsuki, T., Schwab, B., Thompson, N. C., Elson, E. L., 2001. Effects of cytochalasin D and latrunculin B on mechanical properties of cells. J Cell Sci 114 (Pt 5), 1025–36.

Watson, J. D., Crick, F. H., 1953. Molecular structure of nucleic acids; a structure for deoxyribose nucleic acid. Nature 171 (4356), 737–8.

Watt, A. J., Battle, M. A., Li, J., Duncan, S. A., 2004. GATA4 is essential for formation of the proepicardium and regulates cardiogenesis. Proc Natl Acad Sci U S A 101 (34), 12573–8.

Wei, L., Roberts, W., Wang, L., Yamada, M., Zhang, S., Zhao, Z., Rivkees, S. A., Schwartz, R. J., Imanaka-Yoshida, K., 2001. Rho kinases play an obligatory role in vertebrate embryonic organogenesis. Development 128 (15), 2953–62.

Weiss, P., 1939. Principles of development: a text in experimental embryology. Henry Holt and Company, Inc., New York.

Weliky, M., Minsuk, S., Keller, R., Oster, G., 1991. Notochord morphogenesis in Xenopus laevis: simulation of cell behavior underlying tissue convergence and extension. Development 113 (4), 1231–44.

Weliky, M., Oster, G., 1990. The mechanical basis of cell rearrangement. I. Epithelial morphogenesis during Fundulus epiboly. Development 109 (2), 373–86.

Wiens, D. J., 1996. An alternative model for cell sheet migration on fibronectin during heart formation. J Theor Biol 179 (1), 33–9.

Woda, J. M., Calzonetti, T., Hilditch-Maguire, P., Duyao, M. P., Conlon, R. a., MacDonald, M. E., 2005. Inactivation of the Huntington's disease gene (Hdh) impairs anterior streak formation and early patterning of the mouse embryo. BMC Dev Biol 5, 17.

Wozniak, M. A., Chen, C. S., 2009. Mechanotransduction in development: a growing role for contractility. Nat Rev Mol Cell Biol 10 (1), 34–43.

Xu, G., Knutsen, A. K., Dikranian, K., Kroenke, C. D., Bayly, P. V., Taber, L. A., 2010. Axons pull on the brain, but tension does not drive cortical folding. J Biomech Eng 132 (7), 071013.

Yue, Q., Wagstaff, L., Yang, X., Weijer, C., Münsterberg, A., 2008. Wnt3a-mediated chemorepulsion controls movement patterns of cardiac progenitors and requires RhoA function. Development 135 (6), 1029–37.

Yutzey, K. E., Kirby, M. L., 2002. Wherefore heart thou? Embryonic origins of cardiogenic mesoderm. Dev Dyn 223 (3), 307–20.

Zamir, E. A., Czirók, A., Cui, C., Little, C. D., Rongish, B. J., 2006. Mesodermal cell displacements during avian gastrulation are due to both individual cell-autonomous and convective tissue movements. Proc Natl Acad Sci U S A 103 (52), 19806–11.

Zamir, E. A., Rongish, B. J., Little, C. D., 2008. The ECM moves during primitive streak formation–computation of ECM versus cellular motion. PLoS Biol 6 (10), e247.

Zamir, E. A., Srinivasan, V., Perucchio, R., Taber, L. A., 2003. Mechanical asymmetry in the embryonic chick heart during looping. Ann Biomed Eng 31 (11), 1327–1336.

Zamir, E. A., Taber, L. A., 2004a. Material properties and residual stress in the stage 12 chick heart during cardiac looping. J Biomech Eng 126 (6), 823–30.

Zamir, E. A., Taber, L. A., 2004b. On the effects of residual stress in microindentation tests of soft tissue structures. J Biomech Eng 126 (2), 276–83.

Zar, J. H., 2010. Biostatistical analysis, 5th Edition. Prentice-Hall/Pearson, Upper Saddle River, N.J.

Zhou, J., Kim, H. Y., Davidson, L. a., 2009. Actomyosin stiffens the vertebrate embryo during crucial stages of elongation and neural tube closure. Development 136 (4), 677–88.

Zhou, J., Kim, H. Y., Wang, J. H.-C., Davidson, L. A., 2010. Macroscopic stiffening of embryonic tissues via microtubules, RhoGEF and the assembly of contractile bundles of actomyosin. Development 137 (16), 2785–94.